PhD Program in Bioengineering and Robotics

Curriculum: Bionanotechnology

Zein-based smart coatings for drug-eluting stents: investigations via static and microfluidic approaches

May 2023

Student: Martina Lenzuni

Cycle: XXXV

Tutor: Athanassia Athanassiou

Supervisors: Giulia Suarato, Rosalia Bertorelli

To my family,
who never doubted my potential.

Acknowledgments

I would like to take this opportunity to extend a sincere thank you to my supervisor Dr. Giulia Suarato for her support, guidance, and encouragement throughout this journey. I have gained a lot from her character and working attitude; I have learned so much and consider myself very privileged to have had her as a mentor.

I would like to express my gratefulness to my PI, Dr. Athanassiou, for giving me the opportunity to take on an incredibly challenging research project. Thank you for giving me a wide range of creative freedom that allowed me to develop my skills within various disciplines. Sincere gratitude goes to my co-supervisor, Dr. Rosalia Bertorelli, for giving me the chance to work in her research group and for opening the door to her laboratories. My special thanks are dedicated to Dr. Perotto and Dr. Papadopoulou for their encouragement, guidance, discussions, and continuous advice. A special thank goes to Prof. Alessandro Coclite for giving me the opportunity of presenting my research at Politecnico di Bari.

My thanks also go to the technical staff of IIT for their friendship and help with laboratory tools. I would like to thank Lara, Giorgio, Riccardo, Maria, Simone, Doriana, Federico, and all the technical staff from the Nanochemistry group for the help and assistance throughout the years.

To the members of the Smart Materials group for their extensive knowledge and willingness to help. A special thank you to my colleagues who have become friends. A special mention goes to Fabrizio for introducing me to the secrets of cell culture techniques and his continuous support in day-to-day life. To my extraordinary friend Marco who has always believed in me and supported me on the path of science. My time at IIT would not have been the same if it was not for Marta. Thank you for always supporting me and being a source of comfort and advice. I am thankful to all my dear friends from all over the world for their valuable friendship and for making a pleasant and warm environment feel like home for me.

The last but most important THANKS goes to my enlarged family for their support throughout my study and their encouragement for each new challenge. Thanks to Matteo for always being there for me on my journey to becoming a scientist and bringing things into perspective when I needed it the most.

Abstract

Coronary heart disease is currently responsible for a significant percentage of global mortality in developed and developing nations alike. This occurrence takes place despite the advancement in medical technology and improved treatment options, such as stenting procedures. Due to complications with restenosis and stent thrombosis that are associated with current commercial stents, there has been a growing interest in stent research and development in order to eradicate the causes of such clinical events. The selection of an antioxidant, non-thrombogenic coating has been a major obstacle to the development of drug-eluting stents (DES), and, to date, a truly biocompatible stent platform remains elusive. Moreover, there is a need to assess stent coatings within an *in vitro* platform prior to *in vivo* and clinical studies in order to minimize adverse effects. Even if considerable progress has been made over the last two decades in the development of flow chambers to monitor and study thrombus formation outside of the circulation, blood-material interactions are still little investigated under static and dynamic modes.

In order to avoid some of the drawbacks of synthetic polymers, such as their undesirable degradation products, long-lasting presence, or potential biocompatibility issues, the aim of this PhD thesis was to investigate zein as a green and abundant plant-derived protein as a coating material for DES applications. This study aimed to understand the potential uses of zein as a controlled release matrix for drug delivery systems, in addition to developing a microfluidic platform to assess the behavior and hemocompatibility of the proposed plant-based stent coatings under flow conditions.

In **Chapter 1**, the relevant background was described, including coronary heart disease and percutaneous coronary intervention, biological cascades associated with the development of atherosclerosis and restenosis, current state-of-the-art stent commercial products (taking into consideration both drugs and coatings), and challenges associated with *in vitro* stent microfluidic studies. Biodegradable polymers, including zein, and their features for biomedical applications as presented as well in this introductory chapter. **Chapter 2** describes the work conducted to develop innovative zein-based coatings for DES with the ability to release an antioxidant drug. Zein (as the matrix) and rutin (as the active component) were selected for this purpose as available natural compounds easily extracted from vegetable waste through green and sustainable approaches. A series of bilayer coatings with different naturally-derived polymers as sacrificial layers were successfully fabricated. The chosen system, which was produced and fully characterized in this first PhD project, was the cross-linked alginate/rutin-loaded zein bilayer. The single and bilayer coatings properties were comprehensively assessed by means of relevant material characterization tests and biocompatibility assays on endothelial cells and fibroblasts to validate the absence of cytotoxicity. Most importantly, zein-based coatings resulted biocompatible and biodegradable, which are essential features for their

final application. **Chapter 3** addresses the design and development of fused silica-based platforms for investigating zein-based (and eventually any) DES coatings via a microfluidic approach. Dynamic experiments, such as matrix degradation and drug release tests, were carried out to simulate flow conditions in blood arteries and anticipate how the proposed plant-based biomaterial would react *in vivo*. Moreover, thrombogenicity experiments with mice whole blood were performed using this innovative microfluidic technology to confirm the hemocompatibility of the proposed naturally-derived coatings. The overall conclusions of the PhD project and the recommendations for future studies are presented in **Chapter 4** in order to tighten the gap between research and the development of a more biocompatible and effective stent coating and testing platform.

List of Contents

List of Figures

Chapter 1

Chapter 2

Chapter 3

List of Tables

Chapter 1

Chapter 2

Chapter 3

List of Abbreviations

ABTS - 2,2-azino-bis-(3-ethyl-benzthiazoline-6-sulfonic acid)

ATR - Attenuated total reflection

BMS - Bare metal stents

CAGB - Coronary artery bypass grafting

cAlg - cross-linked alginate

CHD - Coronary heart disease

CLSM - Confocal laser scanning microscope

CoCr - Cobalt chromium

CVD - Cardiovascular disease

DES - Drug-eluting stents

DMEM - Dulbecco's modified Eagle's medium

DMSO - Dimethyl sulfoxide

DPPH - 2,2-diphenyl-1-picrylhydrazyl

Fg- Fibrinogen

FDA - Food and drug administration

FLICE - Femtosecond laser irradiation and chemical etching

FTIR - Fourier transform infrared spectroscopy

GRAS - Generally recognized as safe

HDFa - Adult primary human dermal fibroblasts

HDL - High-density lipoproteins

HF - Hydrofluoric acid

HUVEC - Human umbilical vein endothelial cells

ISR - In-stent restenosis

LDL - Low-density lipoproteins

MSCs - Adult mesenchymal stem cells

mTOR - Mammalian target of rapamycin

NF-κB - Nuclear factor kappa-light-chain-enhancer of activated B cells

P(3HB) - Poly(3-hydroxybutyrate)

P(4HB) - Poly(4-hydroxybutyrate)

PBS - Phosphate-buffered saline

PBTP - Polybutylene terephtalate

PBMA - Poly(butyl methacrylate)

PCI - Percutaneous coronary intervention

PCL - Polycaprolactone

PDMS - Polydimethylsiloxane

PEO - Poly(ethylene oxide)

PEVA - Poly(ethylene-co-vinyl acetate)

PGA - Poly(glycolic acid)

PHA - polyhydroxyalkanoates

PHBV - Poly(hydroxybutyrate-co-valerate)

PLGA - Poly(lactic-co-glycolic acid)

PLA - Poly(lactic acid)

PMMA- Poly(methyl methacrylate)

POE - Poly(orthoester)

PPFC - Parallel plate flow chambers

PU - Polyurethane

PVA - Poly(vinyl alcohol)

SBF - Simulated blood fluid

SEM - Scanning electron microscopy

SIBS - Poly(styrene-b-isobutylene-b-styrene)

SMCs - Smooth muscle cells

SS - Stainless steel

TNF-α - Tumor necrosis factor α

XPS - X-ray photoelectron spectroscopy

ZR - rutin-loaded zein

Chapter 1 – Introduction

1.1 Cardiovascular stents

Cardiovascular diseases (CVDs) have had a massive global health impact, accounting for 10.3 million new diagnoses in 2019 alone, according to the European cardiovascular disease statistics. These numbers make CVD the leading cause of mortality under 65 years in Europe, leaving cancer behind in second place [1]. Even if variables such as social organization and economic growth produce regional variances, CVD is on the rise globally. In particular, coronary heart disease (CHD) is one of the major causes of mortality and premature disability in developed countries, accounting for 7.2 million deaths each year [2]. CHD is primarily caused by the formation of coronary atherosclerotic (or atheromatous) plaques, which diminish artery lumen size, reducing blood flow to the heart and frequently resulting in severe consequences such as myocardial infarction or angina pectoris [3, 4]. According to recent data, the prevalence of myocardial and ischemic infarction in men was about three times higher than for women, and incidence typically started in the fourth decade and increased with age [5]. Clinical manifestations of CHD may be chronic and stable, with chest pain (stable angina) induced by physical exercise. Patients with more acute clinical scenarios experience a rapid escalation and sudden onset of symptoms (acute coronary syndrome) [4].

Atherosclerosis is considered an inflammatory process since the accumulation of low-density lipoproteins (LDL) into the vascular wall leads to inflammatory reactions. More in detail, atherogenesis (the production of atheromatous plaques in the walls) begins with the dysfunction of the vascular endothelium (Figure 1.1). During these events, the expression of adhesion molecules such as the vascular cell adhesion molecule-1 and the intercellular adhesion molecule-1 is increased on endothelial cells and leads to a reduced release of nitric oxide and other substances that help prevent the adhesion of macromolecules, platelets, and monocytes to the endothelium [4, 6]. When the vasculature is damaged, lipids, mainly cholesterol in the form of LDL, and monocytes start to build up near the site of the lesion. The monocytes migrate into the tunica intima of the vessel wall, where they undergo macrophage differentiation (Figure 1.1a). They ingest and oxidize LDL, assuming a foam-like appearance. Smooth muscle cells (SMCs) then begin to migrate from the tunica media, and macrophage foam cells aggregate, resulting in a visible fatty streak [7]. A fibrous cap consisting of SMCs and collagen forms as the first macrophages and monocytes engaged in the process start to die. Leucocytes and lipid fragments continue to enter the lesion, causing the plaque to expand into the artery lumen as atherogenesis progresses, decreasing blood flow and myocardial oxygen supply (Figure 1.1b). During periods of physical activity, an imbalance in oxygen demand and supply occurs, causing the onset of ischemia and

angina symptoms [4]. Atherosclerosis often develops over a long period of time, typically several decades, and the growth of atheromatous plaques probably occurs intermittently, with periods of relatively slow growth and periods of fast change [3].

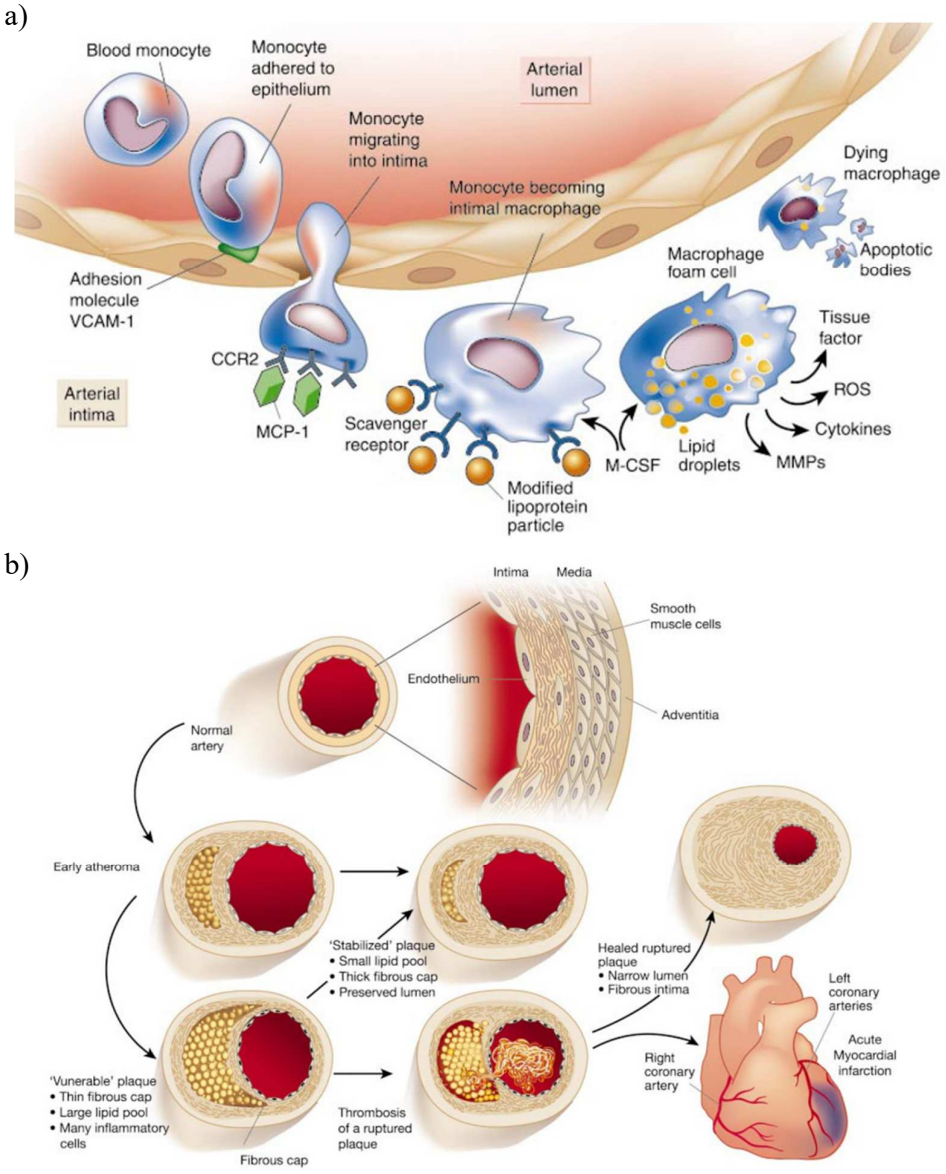

Figure 1.1. *Development of atheromatous plaques. a) The monocyte attaches to an adhesion molecule on a damaged endothelial cell of the artery. The monocyte then migrates into the intimal layer of the arterial wall and differentiates into a macrophage. The macrophage ingests and oxidizes low-density lipoproteins, assuming a foam-like appearance. The foam cells release substances that cause inflammation and growth of the intimal layer. b) Additional accumulation of macrophages and lipid fragments causes the plaque to become larger and larger. With the progress of atherogenesis, the plaque might occlude the vessel, reducing the blood flow and eventually rupture, leading to the formation of a thrombus. Adapted from Libby et al* [4].

Many risk factors contribute to the dysfunction of the vascular endothelium and the subsequent formation of the atherosclerotic plaques. The most important ones are high plasma concentration of LDL, which is increased as a consequence of poor life style habits, such as daily eating of highly saturated fat and excess of cholesterol, cigarette smoking, and physical inactivity, as well as by pathological conditions such as obesity, diabetes mellitus, hypertension, and hyperlipidemia. However, atherosclerosis can also develop in people with perfectly normal levels of cholesterol and lipoproteins [3, 4]. Epidemiological studies have shown that, in populations with low plasma cholesterol levels, such as are observed in the Japanese living on their islands, the incidence of coronary heart disease remains very low despite a high prevalence of smoking [8].

There are different therapeutic strategies to treat CHD; these include drug treatments and myocardial reperfusion or revascularization. In addition to appropriate hygienic and dietary regimen (to reduce risk factors), administration of pharmacological agents (e.g., anti-thrombotic, anti-ischemic, lipid-lowering drugs) is systematic and is done prior to any cardiovascular intervention [9]. Surgical treatments for CHD include coronary artery bypass grafting (CABG) and percutaneous coronary intervention (PCI):

- CABG is a procedure where a blood vessel graft bypasses the obstructive lesion. An artery or vein is harvested from the body to connect the aorta (the major artery that takes blood from the heart to the rest of the body) to an artery beyond the point of obstruction. This restores blood flow by "skipping" (bypassing) the narrowed or blocked area.
- During PCI an inflatable balloon is threaded to the site of the atherosclerotic lesion on a catheter and inflated to open the narrowed coronary artery. In order to keep the vessel open, wire tubular structures, known as stents, are then expanded inside the artery. The main steps of the stenting procedure are shown in Figure 1.2. Firstly, the stent, mounted on a balloon catheter in a crimped (i.e., collapsed) state, is positioned where the narrowing occurs. Secondly, the stent is expanded by balloon inflation. Lastly, the balloon is deflated, and the entire system is removed from the body with the exception of the permanently deformed stent, which remains in place, holding the artery open [10, 11].

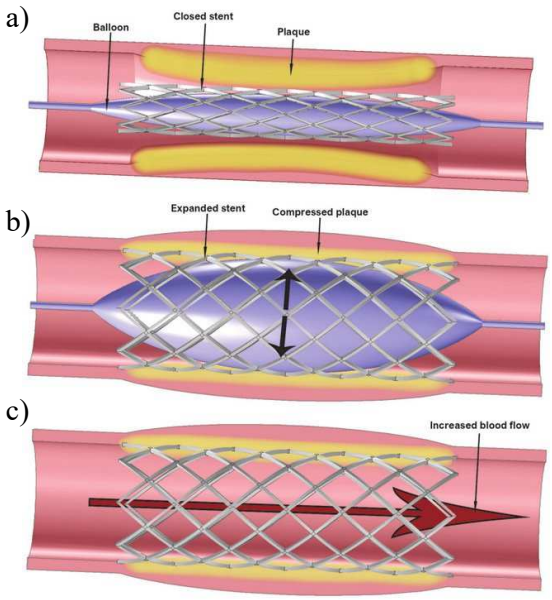

Figure 1.2. *Main steps of the stenting procedure. The stent is inserted into the constricted artery using a balloon catheter that is positioned over a guide wire (a). When the balloon is inflated, the stent expands and keeps the vessel open once it is in position (b). The stent is left in place permanently while the balloon is deflated and removed (c). Adapted from Gudino et al* [11].

Compared to CABG, PCI is performed under local anesthesia and only requires a one-day hospital stay, which reduces recovery time and expenses [12]. Since the introduction of PCI with stents in 1986, the use of this minimally invasive procedure for coronary revascularization has rapidly expanded, as reflected by declining rates of CABG interventions [13]. The medical term "stent" was originally derived from Charles T. Stent, a dentist who developed dental impression materials in the 19th century. The "stent" material was then used to indicate skin grafts during the First World War. The word then transitioned into the meaning of "any kind of non-biological support used to give shape or form to biological tissues" [14]. Although the stent was established as a tool for percutaneous insertion, the word itself did not appear in literature until Charles Dotter published an article reporting expandable stent grafting in 1983 [15]. Over the next few years, the use of coronary stents rose dramatically, and by 1999 they were utilized in over 85% of PCI [16]. Coronary stents have evolved over the past four decades to become one of the most implanted prosthetic devices worldwide, with about 4 million procedures performed annually. The current shift in demographic aging has led to an increase in patients requiring stent intervention due to the rise in the population suffering from CHD [10].

The majority of commercially available coronary stents are fabricated with metallic alloys such as cobalt chromium (CoCr), 316L stainless steel (SS), or nickel-titanium (nitinol). The deployment mechanisms of these stents are either self-expandable or balloon-expandable, where the latter method

requires the material to undergo plastic deformation and must have the ability to preserve the shape and position once expanded. The stainless steel 316L alloy has been the most commonly used metal platform for stents due to its properties (i.e., strength, corrosion resistance, and ductility) [17]. It is worth noting that a relevant portion of the population (~20% of women and ~4% of men) is allergic to nickel and could show signs of contact dermatitis. Moreover, a high nickel percentage has shown teratogenic and carcinogenic effects. Stainless steel is considered safe as long as corrosion does not occur and high hazardous ion concentrations do not interact with the surrounding tissue [17].

1.1.1 Post-implantation cascade

Although PCI with stents is the most widely performed procedure for the treatment of CHD, it is still associated with severe clinical long-term complications such as in-stent restenosis (ISR) [18]. Restenosis, as the name suggests, is the re-occurrence of stenosis (i.e., the reduction of the lumen size) and has been reported to have up to 40% chance of occurrence [18]. Restenosis is defined as a re-narrowing of >75% of the cross-sectional area of the stented artery [6]. ISR develops through a complex cascade of cellular events and results from excessive and pathological neointimal tissue growth as a healing response to vascular injury caused by stent deployment. Oxidative stress is known to be increased after angioplasty and may be involved in adverse remodeling by enhancing nitric oxide breakdown, hence intensifying vessel constriction [19]. ISR is influenced by the negative effects induced by stent presence in the coronary artery, such as a structural injury during implantation, foreign-body reaction, and local fluid dynamic alteration. More in detail, stent deployment results in a complex vascular response that is characterized by different phases, separated in time but partially interdependent (Figure 1.3) [20]:

1. Thrombosis: it represents the dominant physiological response in the first days after the implantation, when the stent and the balloon could damage the endothelial cells, exposing deeper wall structures, such as collagen fibers, to the blood flow. Platelets in the bloodstream are activated and adhere to the damaged endothelial cells, releasing chemical attractants for other platelets. These injuries induce the coagulation cascade, which involves several coagulation factors and leads to the formation of fibrin around the platelets, binding them together into a thrombus. Foreign-body reactions also cause thrombus formation, with different blood-soluble proteins adsorbing onto the stent surface and forming a thin film. Fibrinogen, a pro-thrombotic protein, promotes activation and adhesion of platelets and is adsorbed preferentially over the other macromolecules [21].
2. Inflammation: inflammatory reaction occurs immediately after stenting where the thrombus forms. Surface-adherent leukocytes are attracted to the injured site to prevent the propagation of the tissue damage and aid in wound healing and repair [21]. Intricate molecular mechanisms

orchestrating the process of vascular healing become dysregulated in the presence of persistent inflammation due to an imbalance of growth-promoting and growth-inhibiting signals [20].

3. Proliferation: a new tissue (i.e., neointima) grows around the implanted device as a result of foreign-body reaction and injury provoked by stent deployment. SMCs migrate from the middle layer of the arterial wall towards the intima layer, where they proliferate. These cells synthesize collagen, creating a bulk of new tissue that narrows the coronary artery. The degree of SMCs hyperproliferation is greatly influenced by the degree of thrombosis and inflammation [22]. However, correct re-endothelialization and complete regeneration of the denuded endothelial layer are complex processes not yet fully understood [6].
4. Remodeling: coronary artery opposes the strain caused by the stent strut by increasing collagen deposition, destruction of elastin, and persistent inflammation. From about four weeks after the stent implantation, collagen deposits in the neointima lead to shrinkage of the artery. This process increases the pressure on the device and may squeeze the arterial wall through the stent strut interstices from the outside [23].

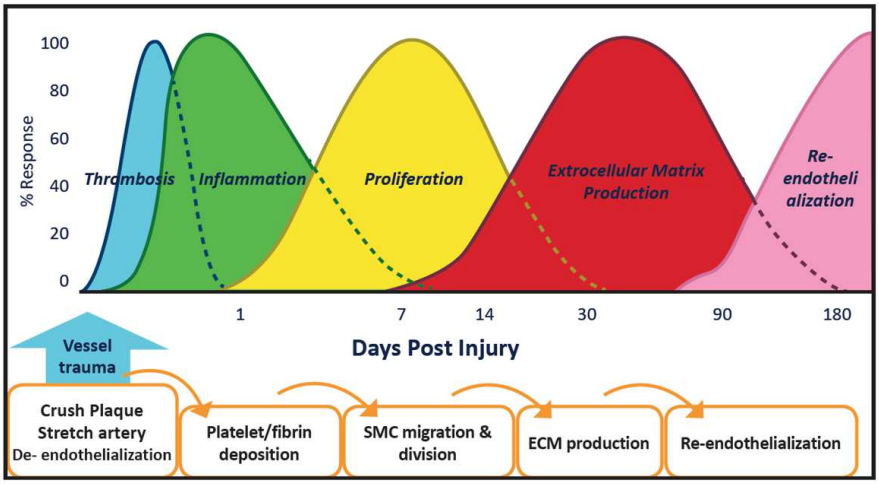

Figure 1.3. *The restenosis cascade following vessel injury. As the stent is inserted into the target site, a certain level of damage occurs, followed by a healing response. Platelet agglomeration and thrombus formation occur, followed by cell recruitment, where these cells produce certain factors which induce SMCs activation. This activation causes the proliferation and migration of SMCs into the intimal layer, thus causing ISR. Adapted from Deloose et al [24].*

To recapitulate, vascular stent implantation initiates a chronic healing response of the affected blood vessel, and it is often accompanied by the presence of reactive oxygen species and by incomplete endothelial coverage, which increases permeability and allows entry of high levels of lipoprotein and inflammatory cells [22]. Sometimes, even after forming an intact endothelial layer, the endothelium does not exhibit its most crucial function, which is vasodilation [25].

1.1.2 Drug-Eluting Stents (DES)

Studies have been conducted on identifying a correlation between ISR and metal ion release from bare metal stents (BMS), and even though the reports in the literature were not wholesome enough to provide an absolute conclusion, the studies do indicate that there is evidence of metal ion release into the vascular wall that could negatively influence chronic ISR in terms of long-term safety [17]. The phenomenon of ISR has been partially attenuated by the introduction in 2004 of drug-eluting stents (DES), which are able to release drugs with predictable pharmacokinetics into the arterial wall and vessel lumen. Ron Waksman proposed the first definition of a drug-eluting stent as "a device that presents or releases one or more bioactive agents to tissue at and near an implant" [26]. The DES are based on three aspects: the stent platform, the stent coating, and the drug itself (Figure 1.4).

- The stent platform is usually a metallic alloy, as in the case of BMS, and should have all the desirable mechanical requirements (in particular high flexibility, high radial strenght, low elastic radial recoil, and high fatigue strength) [27].
- The stent coating is the intermediate layer that facilitates drug adhesion and delivery from the stent platform into the surrounding environments. The polymer is mixed with the chosen drug to form a drug-polymer matrix and placed over the stent platform.
- The drugs can be classified as anti-proliferative, anti-thrombotic, immunosuppressive, anti-inflammatory, and pro-healing agents. High levels can be delivered to the site of interest using the stent as a drug-carrying vehicle without the risk of systemic contamination. The most widely used drugs, approved by the USA Food and Drug Administration (www.fda.gov), belong to the taxanes and rapamycin classes, which fight neointima growth by their ability to target the key event of restenosis development, i.e., suppressing SMCs proliferation. Apart from exhibiting cell growth suppressive properties, these drugs were selected because of their lipophilicity and low solubility properties. Their high tissue retention ability makes them ideal for local stent delivery, allowing a slow and sustained drug release into the vascular wall. However, taxanes and rapamycin are frequently associated with poor *in vitro* to *in vivo* data correlation due to their low water solubility [28].

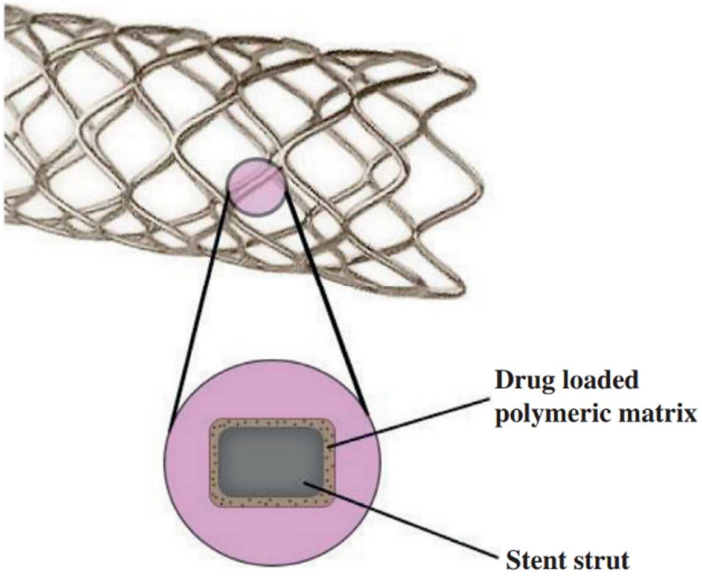

Figure 1.4. *Illustration of a drug-eluting stent (DES). Adapted from Deb et al [29].*

The use of DES has resulted in significantly improved outcomes compared with BMS: the incidence of ISR was reported to be ~40% for the BMS and less than 10% for DES in several randomized clinical trials [18, 30]. However, with more than 3 million stents implanted annually, even a seemingly minor complication can cause thousands of deaths per year (approximately 1-2% of DES-receiving patients) [31].

A range of adverse biological responses has been attributed to the permanent polymer coating on DES, including hypersensitivity reactions, medial necrosis, vascular inflammation, and hypereosinophilia [32]. Collectively these reactions contribute to stent thrombosis, with acute events occurring within the first 24 hours after stent placement due to uncovered dissections, and, although rare, the end results are usually fatal. Late stent thrombosis would occur 30 days after implantation and is now considered a well-known complication associated with DES caused by poor or delayed endothelialization [33, 34].

To overcome these drawbacks, degradable polymer coatings for DES were designed and, based on several trials, have been superior compared with durable polymer [35]. Differences include the eluted drug, the kinetics of elution, and the coating degradation time. Whether thinner struts that enhance faster endothelialization and vascular healing in addition to lowering the risk of uncovered struts lead to improved clinical outcomes or if they are due to degradable polymers that decrease long-term inflammation and development of neo-atherosclerosis remains up for debate [36, 37]. The main problem of degradable polymer layers lies in their degradation products, arising as a result of contact with biological fluids and the ability to trigger inflammation followed by thrombosis [38]. Van der Giessen and coworkers tested different polymers attached to coil wire stents. These coated devices were inserted

into the coronary arteries of porcines, but none was found to be physiologically inert [39]. In particular, five different degradable polymers were tested: poly(lactide-co-glycolide) [PLGA], polycaprolactone [PCL], poly(hydroxybutyrate-valerate) [PHBV], poly(ortho ester) [POE], and poly(ethylene oxide)/polybutylene terephthalate [PEO/PBTP]. All of these polymers have been shown to cause a significant inflammatory response inside the coronary artery, followed by neointimal thickening, which was unexpected based on *in vitro* experiments [39]. A more recent study by Busch et al. examined the interaction of endothelial cells, SMCs, and platelets on various degradable polymer surfaces, using well-known materials, such as polyethylene-co-vinyl acetate [PEVA] and poly(butyl methacrylate) [PBMA] as a comparison [40]. The research looked at poly(L-lactic acid) [PLLA], poly(3-hydroxybutyrate) [P(3HB)], poly(4-hydroxybutyrate) [P(4HB)], and a PLLA/P(4HB) blend. Endothelial cells survival was less than the control (polyolefin coverslip) for the PLLA, PEVA, PBMA, and P(4HB) samples, while on P(3HB) the proliferation rate showed to be quite high, but cell clusters were formed as opposed to desired cellular monolayers.

1.1.3 Current commercially available DES

The first patent regarding balloon-expandable stents was filed in 1985 by Julio Palmaz and was later downsized for use as a coronary stent. It was the first balloon-expandable instrument made of stainless steel and was one of the most widely used stents throughout the 1990s. The first ones to be approved by the FDA were the Cesare Gianturco and Gary Roubin stents (Cook Inc), which were made of stainless steel and had a particular Z-shape that gave them considerable resistance [14]. In 2003 the sirolimus-eluting stent Cypher was approved by FDA (Table 1.1), followed soon after by the paclitaxel-eluting stent Taxus, and both of them were shown to be markedly superior to BMS at reducing restenosis [41]. Although the taxanes and rapamycin achieve the same end result, they differ in the mechanism of action. Sirolimus was originally used in organ transplant patients as an immunosuppressant agent since it inhibits the mammalian target of rapamycin (mTOR), leading to the arrest of the cell cycle. Paclitaxel is an anti-neoplastic agent which inhibits microtubule function and halts the cell cycle [26]. Both drugs non-specifically target the proliferation of vascular SMCs, and this non-specificity is one of the key contributors to the biocompatibility limitations of these DES platforms [42]. Moreover, several randomized trials reported late stent thrombosis episodes after both Taxus and Cypher implantation soon after their widespread clinical adoption. Unlike the acute and subacute thrombosis seen in BMS, these reports detailed a phenomenon of stent thrombosis occurring more than 12 months after stenting [23, 34, 43].

Alternative strategies for improving endothelialization have been explored due to the limited ability of traditional stent coatings to improve vascular response. Noteworthy are phosphorylcholine (PC)-based coatings, which showed to generate highly biocompatible stent surfaces by mimicking the

hydrophilic head group of cell membrane phospholipids. These coatings have later transitioned into drug-eluting coatings, as in the example of the Endeavor stent that uses a PC-based system to elute a rapamycin analog (Table 1.1) [44]. The rapid zotarolimus release effect seen with the Endeavor stent has been reported to show signs of reduced local toxicity, and the PC-based coating has been shown to resist fibrinogen adsorption and decrease monocyte and platelet activation [45, 46].

Everolimus is another immunosuppressive agent derived from sirolimus and, similarly to the original agent, also inhibits mTOR. The primary difference between the two compounds is the half-life, which is 60 hours for sirolimus and 30 hours for everolimus. In 2014 an article in The Lancet journal stated that the Xience V stent (everolimus-eluting stent, with a fluoropolymer as coating material) was considered the optimum product in terms of clinical performance since the proposed polymer has a hydrophobic surface which causes a response called fluoropassivation that reduces fibrin adhesion [47]. However, the permanent presence of the fluoropolymer in contact with the vessel wall increased the potential for impaired vascular healing, which can lead to late stent thrombosis and neo-atherosclerosis [37]. It is important to notice that these catastrophic events occur long after the drug is eluted from the stent. For this reason, persistent inflammation has been pinpointed as one of the main aspects of late stent failure [20]. In addition, the extended drug retention in the lipophilic atheromatous plaque of the vascular wall has been suggested to contribute to delayed vascular repair and post-implantation invasion of inflammatory cells [20]. For example, the Cook Medical polymer-free Zilver PTX stent (Table 1.1) has been reported to elute the anti-proliferative paclitaxel agent within 72 hours, which remains retained in the arterial wall tissues for 56 days [48].

New-generation DES include degradable polymers. Recently, the Orsiro stent received FDA approval, and a recent study showed that target lesion failure was significantly reduced at a 2-year follow-up with Orsiro DES compared with Xience V DES (7.5% vs. 11.9%), the latter comprising a durable polymer. Rates of cardiac death were also statistically significantly reduced with DES with degradable polymers, and an increasing number of data nowadays suggest advantages for bioabsorbable polymer-coated stents (e.g., Synergy and Orsiro) versus durable polymer-coated DES [35, 49].

Table 1.1. *Currently FDA-approved drug-eluting stents [36]. SS, stainless steel; PEVA, poly(ethylene-covinyl acetate); PBMA, poly(n-butyl methacrylate); SIBS, poly(styrene-b-isobutylene-b-styrene); PC, phosphorylcholine; PtCr, platinum-chromium; CoCr, cobalt chromium; PVDF-HFP, poly(vinylidene fluoride-co-hexafluoropropylene); PHMA, poly(hexyl methacrylate); PLGA, poly(lactic-co-glycolic acid); PLA, poly(lactic acid).*

Name	Eluted drug	Drug loading	Material	Manufacturer	Year of FDA approval
Cypher	Sirolimus	1.4 μg /mm^2	SS + PEVA and PBMA	Cordis, Johnson & Johnson	2003
Taxus	Paclitaxel	1 μg/mm^2	SS + SIBS	Boston Scientific	2004
Endeavor	Zotarolimus	1 μg/mm^2	CoCr + PC	Medtronic	2008
Promus	Everolimus	1 μg/mm^2	PtCr + SIBS	Boston Scientific	2008
Xience V	Everolimus	1 μg/mm^2	CoCr + PVDF-HFP and PBMA	Abbott Laboratories	2008
ION Stent	Paclitaxel	1 μg/mm^2	PtCr + SIBS	Boston Scientific	2011
Zilver PTX	Paclitaxel	3 μg/mm^2	Nitinol (polymer free)	Cook Medical	2012
EluNir	Ridatorolimus	1.1 μg/mm^2	CoCr + CarboSil® and PBMA	Cordis	2017
Resolute	Zotarolimus	1.6 μg/mm^2	CoCr + PBMA and PHMA	Medtronic	2018
Synergy	Everolimus	1 μg/mm^2	PtCr + PLGA	Boston Scientific	2020
Orsiro	Sirolimus	1.4 μg /mm^2	CoCr + PLA	Biotronik	2021
BioFreedom	Biolimus A9	15.6 μg/mm^2	SS (polymer free)	Biosensor	2022

Lastly, fast-release polymer-free DES have demonstrated comparable clinical outcomes to existing, slow-release polymer-coated DES at 5-year follow-up [50]. In 2010 Tada et al. evaluated the local delivery of Biolimus A9 from a polymer-free BioFreedom stent where the surface is functionalized with the drug applied directly to the device via a solvent coating process [51]. The authors found that the BioFreedom stent demonstrates a superior reduction of intimal proliferation compared with a sirolimus-eluting stent in a porcine model [51]. While pre-clinical studies have shown reduced neointima formation with these devices, it is also noted that the stent struts showed delayed re-endothelialization when compared to an equivalent BMS [52].

1.1.4 Drug delivery mechanisms

The bioactive agents are released from DES surfaces via a carrier-free platform or, more often, they are embedded in a matrix, typically polymer-based [37]. The time dependency of drug release kinetics is crucial, even though an ideal drug release strategy is currently unavailable. Various factors could influence the kinetics of drug release from polymer encapsulation: the property of the drug, the polymer behavior in aqueous solutions, and the coating parameters should be of crucial consideration when designing DES [53]. Different drug release models have been established in order to understand the release mechanism and further optimize the delivery profile from DES coatings. In many drug delivery systems, almost the majority of the molecules are released shortly after being in contact with the elution medium, typically referred to as "burst release". This phenomenon leads to high drug loss and high local drug concentration, causing toxic side effects. The polymer-free approach involves coating the drug directly on the stent surface, whose modifications, including porous and micro-textured or drug reservoirs machined directly onto the strut, are necessary for the success of this approach to retain and release the drug in a controlled way [44].

Passive hydrolysis is the most common method of degradation for synthetic polymers and can be influenced by various aspects, such as the type of chemical bond that governs the polymer backbone and the neighboring functional groups [54]. Their hydrophilicity is also crucial, as increased hydrophilicity would allow further water penetration into the polymer. On the other hand, a high crystallinity would decrease the rate of hydrolysis. The way the polymer hydrolytically degrades could be classified as bulk erosion or surface erosion, where bulk erosion keeps the size of the polymer but loses strength and structural integrity over time. Surface erosion, more predictable due to linear mass loss at the surface, causes polymers to keep their original shape while reducing in size [54].

Figure 1.5 illustrates possible strategies involved in drug release from DES. Drugs may be held in the polymer by covalent bonds (e.g., C-C bonds, sulfur bridges) or non-covalent bonds (e.g., ionic, hydrogen bonds). By dipping or spraying the stent, the blended matrix can subsequently adhere to the stent surface. Drugs are released by dissolution or diffusion when non-degradable materials are used or during polymer breakdown when incorporated into a degradable matrix [53]. Langer and Peppas summarized the classification of drug-loaded polymeric systems with controlled release performance, including diffusion-controlled systems, swelling-controlled systems, and chemically-controlled systems [55]. Diffusion-controlled systems, formulated into two basic configurations (reservoirs and matrix models), are the most widely used platforms: in a matrix model (Figure 1.5a), the drug is uniformly distributed throughout a polymer layer, which leads to a significantly higher drug release rate; in a reservoir model (Figure 1.5b), the drug molecules are incorporated in a core surrounded by a drug-free layer of polymer. The device in swelling-controlled systems (Figure 1.5c) is initially dry, but when inserted in the body it absorbs water and swells, and the drug release begins instantly to diffuse

through the swelled network into the injury site. In the case of chemically-controlled systems (Figure 1.5f), the drug is distributed in the same way as in the matrix model, with the difference that, in this case, the polymer matrix is degraded during the drug release [56]. With the selection of an appropriate mathematical model, the drug release profile from a specific delivery platform could be precisely elucidated [55]. However, it should also be kept in mind that the various theoretical models that have been proposed to explain the drug release processes are often quite insufficient to reliably and precisely predict *in vivo* dissolution rates.

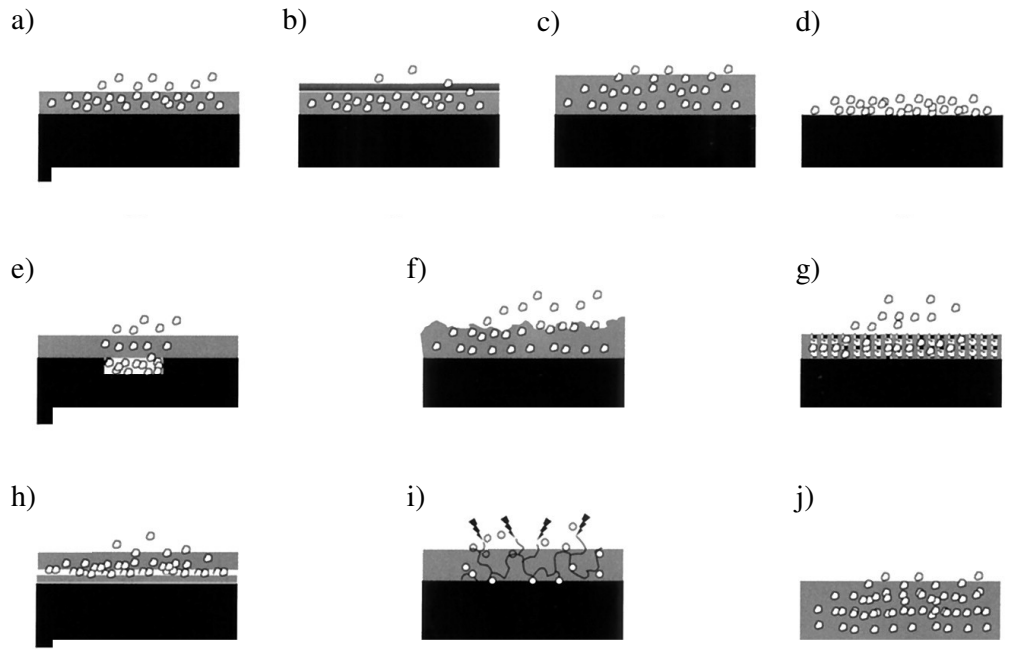

Figure 1.5. *Schematic representation of different modalities of drug-eluting from DES. Black represents the stent strut; gray, coating. a) Drug-polymer blend, release by diffusion. b) Drug diffusion through additional polymer coating. c) Drug release by swelling of coating. d) Non–polymer-based drug release. e) Drug loaded in stent reservoir. f) Drug release by coating erosion. g) Drug loaded in nanoporous coating reservoirs. h) Drug loaded between coatings (coating sandwich). i) Polymer-drug conjugate cleaved by hydrolysis or enzymatic action. j) Bioerodable, polymeric stent. Adapted from Sousa et al [53].*

To date, the most employed method for facilitating drug adhesion and delivery from a stent has involved the use of permanent synthetic polymer coating materials such as PEVA, PBMA, and the triblock copolymer poly(styrene-b-isobutylene-b-styrene) (SIBS), as anticipated in Paragraph 1.1.3. By carefully mixing drugs with these materials, a drug-polymer matrix can be formed and applied to the surface of the stent platform. Upon deployment, drug delivery is driven by diffusion from the matrix, and the rate of this diffusion is determined by the type, composition, and number of polymers used in the drug-polymer formulation. For example, the Taxus stent uses a diffusive approach, where a non-

degradable polymer (SIBS) is used as the paclitaxel housing system. SIBS is a hydrophobic thermoplastic triblock copolymer with elastomeric properties, allowing it to deploy without any mechanical disruption on the Taxus DES. A complication with SIBS is the high adhesive characteristics, requiring high forces needed for the withdrawal of the deflated balloon when deployed in curved areas [57]. The Cypher stent consists of a drug-free layer of PBMA which controls the sirolimus release from the drug-containing layer (a blend of PEVA and PBMA). The drug diffuses from the medium to the upper layer and undergoes an initial burst release which slows down over time [41]. The Endeavour stent uses phosphorylcholine as the matrix material, which allows for rapid Zotarlimus release, with total elution by two weeks after implant [58]. The Xience V stent uses a two-layer coating consisting of a PBMA base adhesive layer and a drug reservoir polymer layer (poly(vinylidene fluoride-co-hexafluoropropylene mixed with everolimus). As with the other durable polymer coatings, the drug is released via molecular diffusion [59].

The latest generation of DES includes several degradable polymers, with poly(lactic acid) [PLA] being the main polymer used, which undergoes slow hydrolysis, breaking down to carbon dioxide, lactic acid, and water. In the Orsiro stent, a degradable PLLA layer is used as a carrier for sirolimus; its bioabsorption takes 15 months, while the drug is eluted in 3 months, resulting in prolonged presence of the polymer long after the drug has been eluted [60]. Additional problems may arise from poor mechanical performance and the generation of acidic products from polymer degradation, which may lead to inflammatory responses and induce neointimal hyperplasia and subsequent restenosis, as well as thrombosis [61]. Similarly, the acidic by-products of poly(glycolic acid) [PGA] make it an unfavorable candidate to be used as a single polymer matrix and can lead to local inflammation as a degrading component of a PLGA polymeric system, such as in the case of the Synergy stent [62]. On the other hand, PLGA in the Synergy coating allows a controlled and sustained delivery of the drug (the release was complete by 90 days) during its own bioabsorption (by 120 days more than 90% of the polymer was eluted). From a clinical perspective, biodegradation of the polymer matrix reduces the polymer burden and eliminates its long-term exposure, potentially mitigating the risk of adverse effects, such as late stent thrombosis [32].

Without using a polymer (e.g., in the case of Zilver PTX or BioFreedom stents), the elution time of the chosen drug is very short. For example, when the Zilver PTX stent is deployed, 95% of paclitaxel is taken up by the cells within 24 hours. This rapid uptake gives the Zilver PTX stent an elution profile similar to that of a drug-coated balloon. However, reports also described that paclitaxel can still be detected in the vessel wall up to 56 days later in nanogram levels [63].

1.1.5 Endothelialization & cytocompatibility

Blood vessels consist of three main sections: intima (tunica intima), media (tunica media), and adventitia (tunica adventitia), as shown in Figure 1.1b. The intima is the innermost layer directly in contact with flowing blood, consisting of an endothelial cell layer. Multiple layers of SMCs make up the media, which regulates blood vessel diameters by contracting or relaxing in response to chemical and neurological impulses. Adventitia is made up of fibroblasts and connective tissue, as well as interspersed SMCs, nerves, and small blood vessels that supply the artery itself [64].

PCI often disrupts the endothelium through mechanical trauma from the guide wire, balloon expansion, and stent implantation. As explained in Paragraph 1.1.1, stent-induced vascular injury is manifested by the removal of the endothelium and phenotypic changes in the underlying SMCs layers. Over time the injury heals with the development of a neointima. Failure of or delayed cell proliferations and migration over injured areas and stent struts have direct clinical consequences [65]. In the case of a stent, its surface is the point of direct contact with the vessel wall and hence would determine the stent efficacy and the healing properties associated with the device.

While first-generation drug-eluting stents (i.e., Cypher and Taxus) contain anti-proliferative agents to inhibit the proliferation of SMCs to combat restenosis, they also delay the regrowth of the intimal endothelial cells resulting in the subsequent development of stent thrombosis, the most notable clinical impact of poor endothelial proliferation [20]. Several studies reported that the endothelialization of BMS struts occurs more rapidly than first-generation DES, reaching completion in 3 months [25]. This is further supported by high-resolution optical coherence tomography and angioscopic studies showing uncovered DES struts two years after implantation, frequently associated with thrombus formation [66, 67]. Scanning electron microscopy (SEM) images of explanted rabbit iliac stents (day 28 post-implant) show poorly endothelialized struts in sirolimus- and paclitaxel-eluting stents. On the other hand, BMS showed a complete and smooth layer of neointima with no visible uncovered struts [33]. It is now well-established that both sirolimus and paclitaxel increase endothelial cells apoptosis, inhibiting migration and proliferation, thereby retarding the endothelialization of stent struts [33, 40, 66]. Moreover, continued inflammation around the permanent polymers may stimulate ongoing neointima formation and late restenosis during long-term follow-up, as evidenced by both clinical and histologic studies [43]. It can be concluded that the phenomenon of delayed endothelialization with first-generation DES can be attributed both to inflammatory reactions to the synthetic durable polymers and the cytotoxicity of the eluted drugs.

Second-generation DES (Endeavor, Xience V, Promus…) evolved by reducing stent strut thickness and improving the biocompatibility of the coated polymer leading to an improvement in endothelialization. Reduction in the incidence of stent thrombosis reported with such DES supports the notion that encouraging endothelial healing translates to tangible clinical benefits [68]. Although the use

of second-generation DES can minimize stent-associated restenosis, there are several areas of concern: the drugs chosen were not intended nor specifically designed to address thrombosis, and non-degradable polymers can interrupt the natural post-injury cellular response (i.e., re-endothelialization) [69]. Only recently, third-generation stents covered with fully degradable polymers such as PLGA and PLA have appeared on the market, with in-depth studies and long-term follow-ups still needed.

1.1.6 The hemocompatibility issue

Although stenting has several benefits over bypass grafting, such as lower risks of complications and a much shorter recovery period, it can result in thrombosis and ISR, which are still the major drawbacks of coronary stent placement in patients with CHD [23, 65, 70]. The beginning of the new millennium saw the introduction of drug-eluting stents, and even though their advantage over bare metal stents was clear in suppressing ISR by elution of anti-proliferative drugs, a new issue of stent thrombosis was identified (Figure 1.6) [43].

As mentioned in the above paragraph, blood vessels are lined with a thin layer of cells which play a pivotal role in maintaining vascular homeostasis. Stent thrombosis is the build-up of a thrombus (blood clot) inside the stented artery and can cause partial vascular occlusion, thus minimizing oxygenated blood flow to the target organ. Before a stent is expanded and deployed at the site of coronary artery stenosis, it is exposed to cellular-protein systems in the blood. Platelets and coagulation factors are the main components of the hemostatic pathway and, in physiological conditions, prevent uncontrolled hemorrhage. The exposure of the underlying cell layer of the vessel to the blood flow induces a mechanism that attracts platelets to the injury site, resulting in eventual aggregation and the formation of a thrombus and sudden occlusion of blood flow, as described in Paragraph 1.1.1.

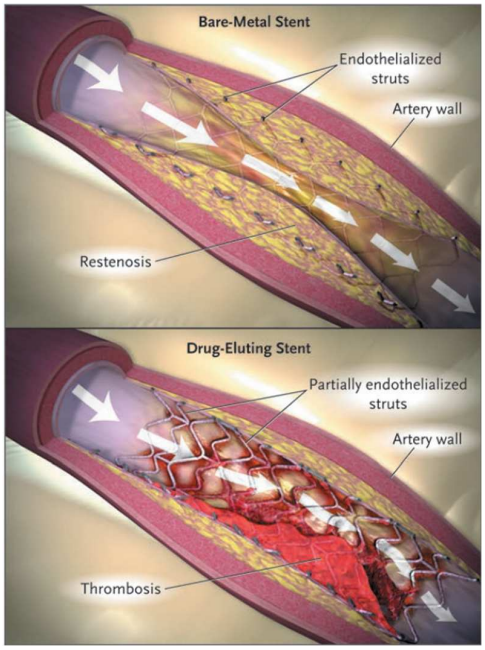

Figure 1.6. *Potential complications of coronary stenting. Restenosis in a traditional bare-metal stent and thrombosis in a drug-eluting stent. White arrows indicate blood flow. Adapted from Curfman et al* [71].

Central to the formation of a hemostatic plug is the linking by fibrinogen (Fg) of adjacent platelets via the αIIbβ3 receptors, which have low affinity for fibrinogen on resting platelets. Following stimulation, a conformation change occurs, engendering a high-affinity state for Fg. Beyond linking platelets, Fg induces phospholipase C activation, which in turn extends platelet activation [72]. This step has important implications for material thrombogenicity where a non-physiological change in Fg conformation results in the stimulation of resting platelets. Coating thrombogenicity is a complex process that involves multiple interrelated mechanisms. Interaction between these processes and the material surface is mediated by a layer of rapidly physically absorbed plasma proteins. This layer develops almost instantaneously on the coating surface upon contact with the plasma [73]. The intrinsic and extrinsic coagulation pathways have both been implicated co-dependently in material-induced thrombosis. Post-mortem studies of patients with DES thrombosis found exposed struts surrounded by an abundance of fibrin clot [33]. To sum up, the initiation of thrombosis in response to a stent depends on two main factors:

1) Disruption of the endothelium with stent deployment, exposing the thrombogenic subendothelial matrix to the flowing platelets and the coagulation cascade factors [74];

2) The inherent thrombogenicity of the stent, involving both the host reaction to the polymer coatings and the detrimental impact of the cytotoxic drugs [61].

Taking these factors into consideration, a biocompatible platform that is innately thromboresistant and simultaneously encourages the recovery of the traumatized endothelium has the

potential to mitigate stent thrombosis. The devastating clinical outcomes of DES thrombogenicity (mortality of 20-40% and myocardial infarction of 50-70%) have made it even clearer that an urgent re-examination of the hemocompatibility of DES coatings is required [75]. Furthermore, it needs to be taken into consideration that the causes of stent thrombosis also depend on the patient (medical history and medication usage), the lesion itself (dimensions, bifurcation, pre-stent stenosis percentage), and the PCI procedure [76].

1.2 Degradable polymers for biomedical coatings

The biological behavior of a biomedical implant is highly dependent on its chemical composition, the morphology of the surface, and its behavior in body fluids. A variety of coating systems have been developed to modify the surface properties of metallic implants, trying to improve their biocompatibility and blood-to-implant contact. Polymeric materials have been widely used in regenerative medicine for tissue fixation or replacement, orthopedics, scaffolds, and drug delivery vehicles [77, 78]. At the same time, polymeric coatings also act as a barrier to shield the implant from the body's fluid environment, thus protecting against possible corrosion. Furthermore, the prepared layer can serve as a local drug delivery platform, releasing biomolecules (growth factors, flavonoids, peptides, etc.) for a specific application, as well as improving the biocompatibility of a medical device [56].

Biodegradable polymers are of key importance in the field of tissue engineering and particularly within the drug delivery aspect. Such systems offer significant advantages over non-degradable matrices, as the degraded polymer is metabolized in the body and a second surgery to remove the drug delivery platforms becomes unnecessary. Biodegradable materials for biomedical applications can be of synthetic or natural origin or a combination of both (Figure 1.7). Novel coating materials aim not only to repair the damage but also quickly regenerate the target tissue and its function. Therefore, biodegradable polymeric materials are nowadays considered superior alternatives in comparison to biostable ones regarding most medical applications [79].

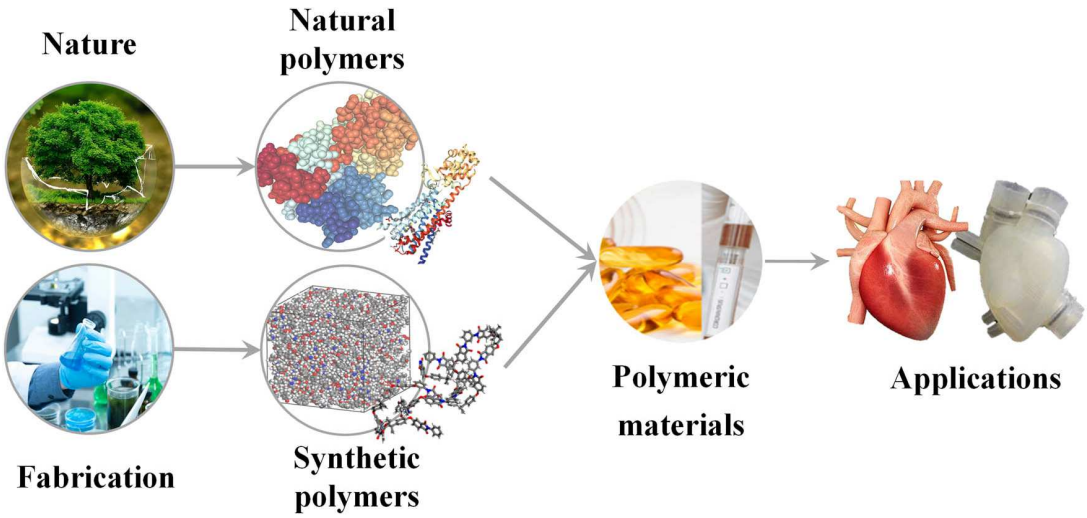

Figure 1.7. *Biodegradable polymers can be divided into two major categories: natural polymers, which can be extracted from natural sources, and synthetic polymers, which are man-made. Adapted from Jian et al [80].*

1.2.1 Synthetic polymers

Synthetic biodegradable materials mainly comprise polymers where tunable degradation occurs over time via hydrolysis [81]. The most widely used for biomedical coatings are polyglycolide (PGA), polylactides (PLA), poly(lactic-co-glycolic acid) (PLGA), polycaprolactone (PCL), and poly(ethers) including poly(ethylene oxide) (PEO), poly(vinyl alcohol) (PVA), and polyurethane (PU). In the 1970s, the shorter molecular version of PEO, poly(ethylene glycol) (PEG), gained notoriety when researchers found that such polymer prevents a variety of proteins from being absorbed [82]. Regarding biomedical applications, PEG-based polymers are non-ionic, biocompatible, and mildly immunogenic [83]. Polyurethanes are another wide class of biodegradable polymers under investigation, particularly for soft tissue engineering applications, as opposed to aliphatic linear polyesters, which are better suited for hard tissue engineering due to their high glass transition temperature and high modulus. Even if polyurethanes display a wide range of characteristics, they still have limited usage as biomedical implants due to the toxicity of their degradation products [77].

Polyester-based polymers are extremely popular due to their susceptibility to properties modification [78]. The critical aspect that needs to be addressed is their level of biocompatibility as well as the by-products of degradation. For instance, PCL is a tough, aliphatic, semicrystalline polymer with questionable biocompatibility. According to reports, the hydrophobic nature of PCL inhibits cell attachment and growth, and various investigations have reported an adverse foreign body response on the material [84]. Similarly, PVA has been applied in multiple biomedical areas due to its favorable properties but lacks cell-adhesive properties [84]. The versatility of polyester-based polymers, and synthetic materials in general, allows for highly controlled degradability: in particular, the use of co-

polymeric coatings allows fine-tuning of their mechanical properties and degradation rates by varying the polymers ratio [79]. PGA and PLA are structurally related, with PLA having an additional single methyl group resulting in increased hydrophobicity. Their minor structural differences have a significant impact on the degradation rate: while PGA rapidly degrades within one month, PLA breakdown can take place from months to years [81]. Degradation rates of several synthetic biodegradable polymers decrease in the following sequence, according to various studies: PGA ~ PLGA > PDLLA > PLLA > PCL [84].

1.2.2 Natural polymers

Finding a suitable material supporting cell proliferation and differentiation for the formation of new tissue continues to draw significant research efforts across the globe in the fields of tissue engineering and regenerative medicine. Naturally-derived polymers (often termed "biopolymers") are highly attractive among various kinds of materials due to their biocompatibility, biodegradability, and similarity to the extracellular matrix components (e.g., collagen, gelatin, hyaluronic acid). Moreover, several biopolymers contain cell-recognition domains and biomolecule binding sites (e.g., RGD and LDV sequences in silk fibroin and keratin proteins) and may have inherent antibacterial and anti-inflammatory properties (e.g., chitosan, alginate), despite batch-to-batch variations in terms of mechanical properties and their relatively short shelf-life [83, 85]. Biopolymers are roughly classified into two classes based on their monomeric units [84]:

- Polysaccharide-based: starch, chitosan, alginate, hyaluronic acid, cellulose, agarose, dextran …
- Protein-based: collagen, gelatin, silk, keratin, zein …

Additionally, polyhydroxyalkanoates (PHA), a class of thermoplastic polyesters, are synthesized by various genera of bacteria (*Bacillus, Rhodococcus, Pseudomonas*, etc.) through the fermentation of sugars or lipids and recently have been acknowledged as natural biodegradable materials for coatings [86]. Bioactivity, biocompatibility, 3D geometry, and non-toxic by-products of biodegradation are the most important properties of natural polymers. The crucial aspect involved with biodegradable polymers for biomedical applications is the rate and type of degradation, which directly contributes to the drug release profile. Synthetic polymers usually degrade hydrolytically, whereas natural polymers are degraded both hydrolytically and via enzymatic reactions [84].

Polysaccharides form a group of naturally occurring polymers that are made of different units of monosaccharide or disaccharide chains. By mixing multiple saccharide isomers using a variety of chemical linkages, the outcome is an incredibly vast number of structurally-varied polysaccharides. As a result, it is not surprising that various saccharides and polysaccharides play a significant part in fine-tuning cell environmental responses [87]. Polysaccharides such as gums, chitosan, alginate, hyaluronic acid, and cellulose were found to be promising materials for different biomedical applications. For

instance, it is known that hyaluronic acid-based coatings enhance the hydrophilicity and biocompatibility of other (bio)materials [84, 87]; chitosan has been widely used as a biomaterial for the repair of articular cartilage in the form of a hydrogel [88]; alginate dressings resulted incredibly helpful as delivery platforms in order to provide a controlled release of therapeutic substances to the skin (e.g., pain-relieving, antibacterial, and anti-inflammatory agents) [85].

Proteins are the other biopolymer group, widely studied for biomedical applications given their abundance in the body and nature in general [89]. These biomacromolecules show excellent biocompatibility and binding capacity with various bioactive molecules, good cell adhesion properties, and targeting ability [90]. Furthermore, proteins are naturally digested *in vivo* by enzymes, generating non-toxic metabolites readily assimilated by the body and performing biological functions such as muscle maintenance, control of immune responses, cell signaling, and repair of damaged cells and tissues [84, 91]. Silk proteins have their primary sequence with a high degree of repetition, which results in a large concentration of β-sheets structures that give silk fibers their favorable mechanical characteristics. Silk fibroin has been claimed to have the potential to be employed in tissue engineering applications that require mechanically robust, long-term degradable materials [83]. For instance, adult mesenchymal stem cells (MSCs) were combined with highly porous silk scaffolds for *in vitro* cartilage tissue engineering [92]. Keratin has also been transformed into films, scaffolds, hydrogels, and other structures as novel drug-eluting biomaterials and has got much interest recently because of its ultrastructure, biodegradability, excellent biocompatibility, and presence of cell interaction motifs [93, 94]. Yang et al. demonstrated the layer-by-layer deposition of keratin on quartz film and showed how a keratin coating might provide a biocompatible surface appropriate for tissue engineering [95]. Recently, Trojanowska et al. showed how micropatterns composed of keratin particles were printed on glass substrates, offering binding sites to cell surface ligands, thus promoting cell adhesion [96].

In this context, plant-derived proteins are readily available, inexpensive, and can be generated as by-products when cereal grains are processed for food or fuel. They represent an alternative to animal-derived proteins since the latter have been reported to have disadvantages like immunogenicity, high cost, batch-to-batch variations, possible transmission of diseases, and ethical issues for the use of animal products [97]. The principal plant-derived proteins are zein (from corn), soy protein, and wheat proteins (gluten, gliadin, and glutenin). They often have higher net negative charges than collagen and silk (i.e., animal proteins) and are thus more suited for delivering positively charged drugs. Moreover, plant proteins possess a higher content of polar amino acids that make them more favorable to attract cells. Due to the above mentioned advantages, increasing efforts are being devoted to exploring possibilities to use plant-derived proteins in various biomedical applications, including tissue engineering [98, 99], drug delivery [100, 101], and wound dressings [102]. For example, Silva et al. reported a bioglass-incorporated bioactive soy protein composite for bone tissue engineering application [103]. Also, soy protein films may find applications as microencapsulating agents of flavors and pharmaceuticals or

in coatings of fruits, vegetables, and cheese. However, chemical modifications such as crosslinking are often required to achieve necessary mechanical properties and water stability for these biomaterials [89].

1.2.2.1 Zein protein

Zein, the main storage biomolecule in corn germ and endosperm, is a prolamine-rich protein that can be extracted from maize (*Zea mays*) gluten meal (a protein-rich by-product of starch production) with aqueous alcohol solutions and dried to a granular powder [104]. Zein is categorized into four sub-families, namely α-zein (19 and 22 kDa), β-zein (14 kDa), γ-zein (16 and 27 kDa), δ-zein (10 kDa). α-Zein accounts for 75% to 85% of the total protein, according to sodium dodecyl sulfate-polyacrylamide gel electrophoresis (SDS PAGE) [105]. Zein comprises hydrophobic, neutral, and polar amino acid residues and shows an amphiphilic behavior, making it capable of self-assembly to form mesostructures with application in foods and pharmaceuticals. It has approximately 50% hydrophobic residues, with high percentages of leucine (20%), proline (10%), and alanine (10%), while the hydrophilic component is owing to the high glutamine content (21%-26%). Moreover, zein stands out from other proteins because it almost completely lacks lysine and tryptophan residues [106]. It is insoluble in water due to a large number of uncharged amino acid residues; nevertheless, in the presence of alcohol, a significant amount of urea, an alkaline pH (> 11), or anionic surfactants, it becomes soluble. The chemical structure stability is attained via van der Waals interactions and intramolecular hydrogen bonding [104, 107]. A proposed three-dimensional structure was established through a small-angle X-ray study of the α-zein, assuming that each of the tandem repeat units formed a single α-helix joined by glutamine-rich turns or loops, as illustrated in Figure 1.8.

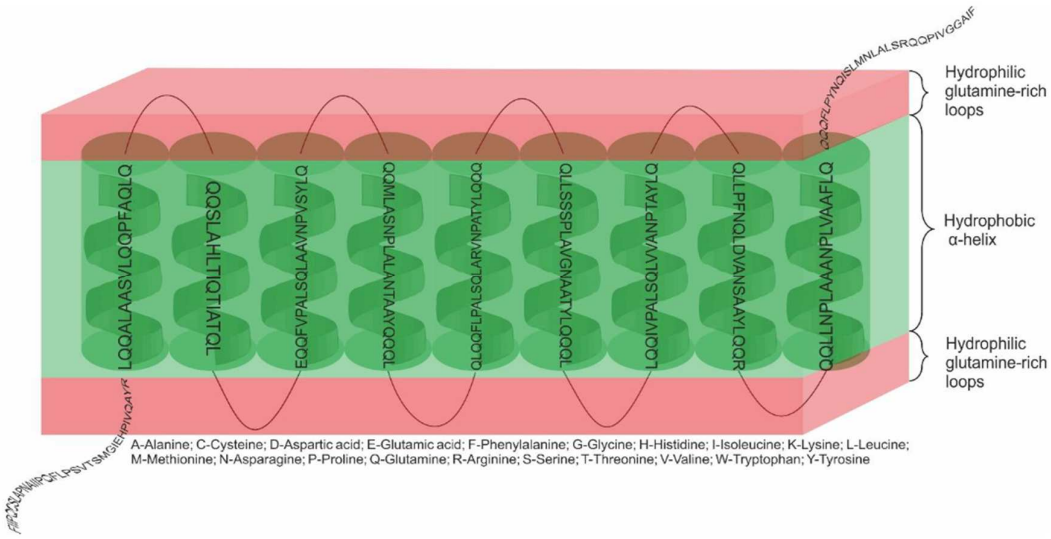

Figure 1.8. *Structural representation of α-zein. The structure is presented by cylinders and abundant amine functionalities on the glutamine (Q)-rich turns (loops) joining them. Non-polar amino acids are located in the hydrophobic core while Q-rich loops are forming the two hydrophilic edges. Adapted from Barbosa et al* [108].

Zein is commercially available in two varieties: yellow zein and white zein, with the former showing a purity of 88–90% and a high concentration of xanthophyll pigments (8–9%) [104]. Zein could quickly be processed in different shapes and structures, such as microparticles, nanoparticles, micelles, films, and gels. Several drugs and bioactive compounds such as ivermectin, gitoxin, anti-cancer drugs, essential oils, food-grade antimicrobials, coumarin, and 5-fluorouracil have been encapsulated in zein-based structures that were investigated for biomedical applications [107, 109]. Zein scaffolds for potential bone replacement implants were investigated as well, with results showing appropriate mechanical characteristics, including Young's modulus of 28–87 MPa and compressive strength of 1.5–11.8 MPa, comparable to cancellous bone [110]. On the porous zein scaffolds, adult mesenchymal stem cells demonstrated excellent adhesion, proliferation, and differentiation into osteoblasts when dexamethasone was present. Wang and coworkers further showed that adding oleic acid as a plasticizer increased the mechanical characteristics (tensile and flexural) of the porous zein scaffold [111]. These findings can be added to the already many unique properties of zein, strengthened its use in tissue engineering, and revealed some promising drug delivery properties with controlled-release characteristics being attained. It is worth noting that the isoelectric point value of zein (6.2) might influence the drug release at different pH values, possibly by promoting some electrostatic interactions with charged drugs [104]. Table 1.2 summarizes some of the key properties of zein as a natural biomaterial for applications in drug delivery and tissue engineering.

Table 1.2. *Desirable properties of zein for applications in drug delivery and tissue engineering. Adapted from Paliwal et al* [104].

Properties	Application in drug delivery & tissue engineering
Insoluble in water but soluble in aqueous-alcohol solutions (2/3 hydrophobic and 1/3 hydrophilic amino acids)	Protein precipitation from the anti-solvent approach leads to particles formation; more sustained drug release rates than hydrophilic proteins; hydrophilic as well as hydrophobic drugs can be encapsulated
Gelling character	Hydrogels can be developed
Inexpensive and generally regarded as safe (GRAS) status	Commercial availability
Adhesive nature	Suitable for mucoadhesive drug/vaccine delivery
Antimicrobial character	Protection of loaded drugs from microbial degradation

The film-forming properties of zein have been recognized for decades and are the basis for its commercial utilization [112]. Coatings are formed on hard surfaces by covering them with zein solutions and allowing the solvent (usually aqueous aliphatic alcoholic solutions) to evaporate. The dried zein residue forms hard, glossy, tough, scuff-proof, grease-resistant, protective coatings that are also resistant to microbial attack. During the coating development process, various natural polymers or plasticizers can be used to further enhance some of the zein features, such as poor mechanical strength. Zein coatings are nowadays already used as oxygen, lipid, and moisture barriers for nuts, candies, confectionery products, and other foods [113]. Based on a long history of zein use in the food industry, the USA FDA approved zein in 1985 as a generally regarded as safe (GRAS) excipient for film coating of drugs, especially tablets [114]. Several examples are available in the current literature; for instance, Liu et al. in 2006 proposed zein as the coating for pectin beads for indomethacin delivery to the colon. The developed coating increased the water resistance of the pectin beads while also protecting the drug from the acidic environment of the stomach [115].

Recently, zein has been probed for its potential as a biomaterial for coating biomedical implants because both zein and its by-products display favorable *in vivo* tissue compatibility [99]. Rehman et al. showed that bioactive glasses/zein coatings for orthopedic implants increased the resistance of a magnesium substrate to electrochemical corrosion and that hydroxyapatite crystals were formed on the coated substrate after three days of incubation in a simulated body fluid [116]. Similarly, in order to improve corrosion resistance and prevent the release of toxic metal ions in the physiological environment, Ahmed et al. used zein and hydroxyapatite to coat SS substrates used for orthopedic

applications. The results show that the proposed coatings were successfully deposited on the steel substrate, and after immersion in simulated body fluid, the coating capacity for bone connections was confirmed [117]. Moreover, previous studies have demonstrated that zein functions as a bioactive molecule since, with the enzyme thermolysin, α-zein hydrolyzes to form peptides that inhibit the angiotensin-converting enzyme; in hypertensive rats, such hydrolysates can lower blood pressure, as demonstrated by Ariyoshi et al [118]. The antioxidant and anti-inflammatory activities of zein-derived peptides on the vascular systems were further investigated by Liang et al., who found a reduction in NF-κB ("nuclear factor kappa-light-chain-enhancer of activated B cells") activation levels and TNF (tumor necrosis factor)-α-induced inflammatory responses and oxidative stress in endothelial cells [119]. The same cell line was tested by Shen et al. in their recent work, where the authors positively evaluated zein-based electrospun fibers as basement membranes for cell retention [120]. Recently, the adhesion of endothelial cells on zein-based 3D-printed tubular structures was investigated by Xue et al., providing a system for 3D cell culture, drug screening, and tissue engineering [121].

1.3 Microfluidics for bionanotechnology

Microfluidics is the discipline of science that deals with the flow and manipulation of a small amount of fluid retained in a confined space [122]. It is a newly developing branch of engineering and has the ability to address different areas of research like chemical analysis, electronics, physics, biomedicine, pharmaceutical sciences, etc. Its attraction in a variety of fields of investigations stems from its microdimension where fluid behavior differs from macroscale, i.e., laminar in microfluidics and turbulent at macroscale due to low and high Reynolds numbers, respectively [122]. The birth of microfluidics can be traced way back to 1950 when it appeared for the first time in different chromatographic systems [123]. Afterward, scientists continued to develop miniaturized systems with improved performance. Fluids in these microfluidic platforms behave similarly to those in certain human physiological systems, such as blood capillary [124], bone [125], tissue interstitial compartment [126], and kidney proximal tubules [127]. The highly predictable microscale physics (e.g., capillarity and laminar flow) dominate over classical macroscale physics (e.g., gravity), resulting in a great degree of control in the design and operation of the devices for the user [128].

In the biomedical field, these miniaturized devices include microreactors for a range of important (bio)chemical reactions, such as mixers to allow studies of protein dynamics over microsecond timescales [129], and devices that improve important biochemical assays such as polymerase chain reaction (PCR) [130] and enzyme-linked immunosorbent assays (ELISA) [131]. Microfluidic devices can accurately control physical and chemical conditions (e.g., temperature, gas tension, medium composition, and concentration of soluble factors) at the microscale level, benefiting from the laminar flow configuration and the high surface-to-volume ratio in order to create *in vivo*-like conditions, while

being compatible with flow-based assays [132]. Another advantage of microfluidic devices is the ability to manipulate multiphase flows. These dispersions provide novel ways to make polymer particles, emulsions, and foams by enabling the development and control of monodisperse bubbles or droplets of a dispersed gas or liquid phase in a continuous liquid stream [122]. Microdimension of microfluidic tools provides different advantages that could be summarized as follows [123, 128, 133]:

1) consumption of small quantity of samples and reagents, thus addressing safety (anticancer drugs, biological and radioactive molecules) and economic issues;
2) parallelization on microfluidic chips allows high throughput and multiple analyses at one time;
3) precise control over flow, i.e., laminar flow where viscous forces are dominant;
4) continuous flow operations;
5) production of particles where the coefficient of variation is less than 5% and high encapsulation efficiency for drug delivery systems;
6) miniaturization allows portability and on-spot analysis due to integration and low power consumption.

1.3.1 Materials and microfabrication processes

Many materials are becoming suitable for building microfluidic devices. Polydimethylsiloxane (PDMS) is an elastomeric polymer that behaves as an elastic solid that maintains its molded structure when cured. Despite the many desirable properties of PDMS, which is nowadays the most commonly used material in microfluidic systems, PDMS has poor chemical resistance to certain solvents, and it can absorb small hydrophobic molecules (e.g., many drugs and fluorescent dyes), thus compromising rigorous chemical testing of potential therapeutic agents. As a result, several research teams are developing substitute materials that may be able to address some of the drawbacks of PDMS. Other polymers have also been widely used, including polymethylmethacrylate (PMMA) and polycarbonate, and fabrication methods include hot embossing and injection molding systems. Glass has the potential to become one of the most suitable material for biological applications, primarily because of its favorable material properties. Fused silica or quartz glass is a type of glass made of almost pure silica in an amorphous (non-crystalline) form that is resistant to a wide variety of chemical agents, with only a few compounds, such as hydrofluoric acid (HF), capable of etching it. Fused silica-based chips are more expensive to fabricate compared to PDMS-based platforms but exhibit excellent pressure and chemical resistance quality, gas impermeability, high stiffness (shear modulus ~30 GPa), low auto-fluorescence, they are optically transparent, and excellent insulators [123, 133].

A limited number of techniques are capable of fabricating microfluidic devices since few strategies have enough resolution to create these structures at a submicron scale. Lithography is the gold standard in the fabrication of microfluidic devices, especially when using PDMS as a replica. The

manufacturing of the photoresist master mold, which requires substantial knowledge and expensive equipment, is the source of most of the costs in the soft lithography production process. Furthermore, the master mold is susceptible to deterioration and has a limited casting life [133]. Ultrashort laser is nowadays one of the most important contact-free tools for micro structuring on a wide variety of materials. Thanks to the short time duration and the very high peak power, ultrashort laser pulses enable new mechanisms of material modification and removal due to a peculiar timescale characterizing the laser-matter interaction. The ultrashort laser fabrication of microfluidic devices represents a niche market in response to the need to find alternative processes to manufacture these components with high accuracy and high-quality surface finishing. In particular, among the techniques which have enabled advances in the field of microfluidic fabrication, Femtosecond Laser Irradiation and Chemical Etching (FLICE) is becoming a valuable and reliable microfabrication technology for the fabrication of embedded microchannels in transparent materials (e.g., glass and fused silica), especially when customization or rapid design modifications are required (Figure 1.9). FLICE is based on permanent bulk modifications that a very intense and ultrashort radiation induces when interacting with a medium. As the second and last step of the technique, the chemical etching is performed with HF, which is applied to the previously irradiated specimens in order to create directly buried microfluidic structures. Finally, the samples must be carefully rinsed for several minutes in an ultrasonic bath with deionized water before being used. The FLICE method offers several immediate benefits over the more well-established photolithography technology: for instance, it is not easy to construct complex 3D structures with photolithography since the process must be repeated numerous times, owing to its inherent 2D nature. On the contrary, femtosecond micromachining allows for the production of 3D geometries, also with circular cross-sections, in addition to avoiding the need for clean rooms [134-136].

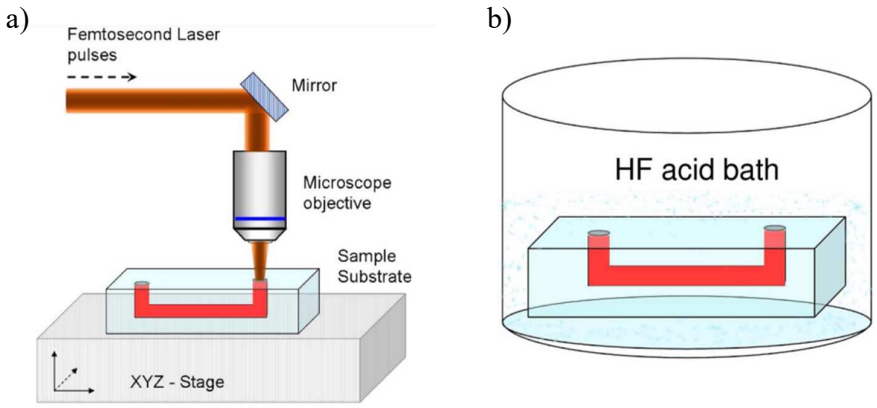

Figure 1.9. *Femtosecond laser fabrication of channels for microfluidic devices. Schematic diagram of the (a) writing setup and (b) etching of the written structure in an HF acid bath. Adapted from Chaitanya Vishnubhatla et al [134].*

1.3.2 Interfacing microfluidic devices

Microfluidic systems allow researchers to recapitulate the physiological microenvironment more faithfully than experiments in conventional static cell culture dishes or larger-scale bioreactors where the flow is turbulent [132]. Microdevices can have either an integrated detection module or are coupled to an external instrument. While optical and fluorescence microscopy are commonly employed, interfaces to many other analytical methods are currently being advanced, opening multiple options for assays, with or without the need for labels [133]. If florescent dyes are used in the flowing medium, chips can be designed with transparent regions to allow real-time microscopy or other imaging modalities with very low working distances [137]. The microfabrication techniques mentioned in the previous paragraph can be used to produce chips for mixing, separation, and analysis of chemical compounds and drugs and also to create on-chip systems for cell culture and assays. These so-called "organ-on-chip" can mimic the cell culture conditions of a biological tissue or organ and allow the reduction or partial replacement of animal studies [138]. Alternatively, microarrays for high-throughput studies enable large numbers of small cell samples to be interrogated in parallel in order to investigate a wide range of cell culture conditions [139]. Interactions between biological systems and materials, governed by phenomena occurring at small length scales, are essential in the development of biomaterials, particularly for applications such as regenerative medicine or drug delivery [140]. Microfabrication technologies have also been used to produce and pattern surface functionalities, such as micro- and nano-topographies, which are of interest in biomaterials science. The resulting chips can mimic a biological niche to study corresponding cell-material interactions *in vitro*. For instance, Kent et al. described a custom-made parallel plate flow chamber (PPFC) to analyze platelet–von Willebrand factor interactions under controlled shear rates (Figure 1.10) [141].

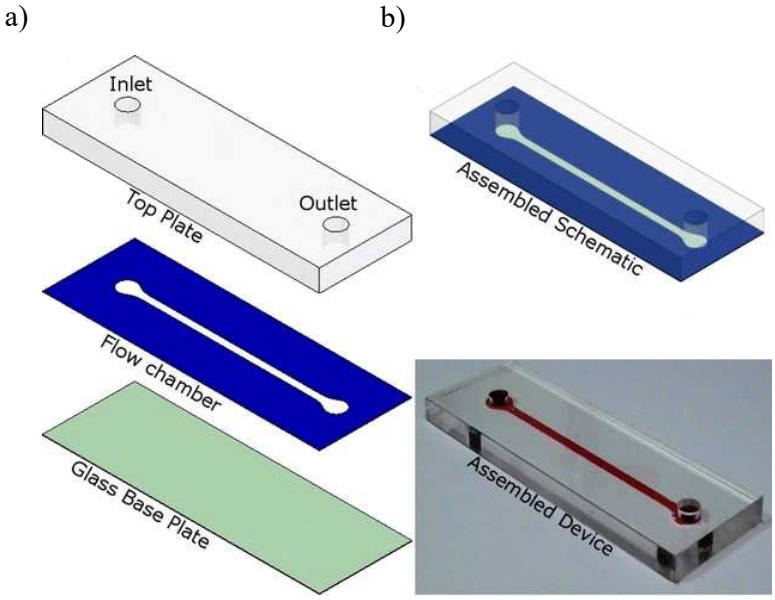

Figure 1.10. *Parallel-plate device schematic. (a) View of the constituent components of the device: top plate, flow chamber layer, and the glass (microscope coverslip) base plate. (b) The layers fully assembled (above), and a photograph of an assembled device (below). Adapted from Kent et al* [141].

PPFCs have been developed to assess various parameters under dynamic settings and are typically built with two plates made of polymeric material (e.g., polycarbonate, PMMA) between which the fluid flows, and a gasket, generally made of silicone rubber, is placed between the plates and defines the height of the flow channel [142]. On the part of the device that houses the samples, it is possible to perform specific surface treatments (e.g., coating with extracellular matrix proteins).

The constant development and research into stent technology have not demonstrated a correlative representation of studies on microfluidic systems that assess the efficacy of stents and/or stent coatings. In earlier studies, Li et al. developed a rectangular PDMS-based channel to exclusively detect the release of fluorescent model drugs from a gold coating [143]; Jia et al. investigated the degradation characteristic of PLGA coatings for stents with a not-well-specified dynamic system [144], while Zheng et al. employed a PPFC to investigate the drug release from PLGA films under different shear stress using an aqueous Tween 20 solution as the release medium [145]. Conversely, the dynamic degradation of magnesium alloy-based stents has been evaluated with modified media and buffers. Wang et al. in 2016 assessed the degradation of magnesium wires (as a stent model) using Dulbecco's Modified Eagle Medium (DMEM) with 10% fetal bovine serum (FBS) and 1% penicillin/streptomycin as standard culture medium with a flow rate of 100 ml/min under normal incubator conditions for five days [146]. Their study focused primarily on comparing the degradation *in vivo* to that of their *ex vivo* bioreactor model. The latter was a commercially available system consisting of a vessel chamber (50

mL of volume), pumps, a flow control channel, and a hertz oscillator. Nevertheless, this system was subsequently considered inaccurate due to the large volume and absence of blood proteins that could affect the stent degradation [147]. Lastly, Ye et al. fabricated a DES using poly(1,3-trimethylene carbonate) on a magnesium-based stent and studied solely its degradation behavior with microfluidic chip, electrochemical, *in vitro*, and *in vivo* tests [148]. Microfluidics has also been recently employed to fabricate diverse functional materials for stent coatings. As an example, Cheng et al. combined electrospinning techniques with microfluidics to generate fibers to coat vascular stents, with the aim of preventing neointimal hyperplasia through the local delivery of selective drugs [149].

Given the recognized involvement of platelets in normal hemostasis and pathological thrombosis, several techniques have been developed to evaluate the processes behind platelet (dys)function. Although flow chamber technology using PPFC is a well-established method for testing platelet function and antithrombotic treatments, it has certain drawbacks, mostly due to a lack of standardization in chamber construction and to the dimensions of the perfusion chamber. Recent efforts to downscale this technology using a variety of microfluidic devices have opened up new avenues for investigating platelet adhesion and activation under finely regulated flow conditions [150]. However, previous studies have almost exclusively focused on platelet behavior on selected molecules, such as tissue factors and antithrombotic drugs, using both custom-made and commercial flow devices, as described by Provenzale et al [151]. To date there is a lack of research focused on assessing the efficacy of stent therapeutics and coatings with regard to thrombus formation. Developing a near-physiological *in vitro* system that could indicate whether a particular drug or material is more hemocompatible than another will not only reduce the number of animals for surgery but will also cut down on cost and time.

1.4 Aim of the study

Drug-eluting stents have been one of the major healthcare advancements in the last three decades in treating vascular diseases, including CHD. Since the introduction of vascular stents, the progression of stent development has been a key field of research. Moreover, due to the nature of such cardiovascular diseases, it is evident an increase in the number of patients that suffer from stent-related complications inherited in the current commercially available stents, including in-stent restenosis and thrombosis [70]. From the literature review, it is clear that a truly biocompatible and hemocompatible stent coating remains elusive. Unfortunately, metallic alloys are inherently thrombogenic, and the multitude of approaches (biodegradable polymer for DES, polymer-free DES …) reflects a lack of a definitive solution to the issue of stent biocompatibility, with low thrombogenicity (Paragraph 1.1.6) and encouragement of endothelial adhesion and proliferation (Paragraph 1.1.5) being the essential determinants.

Based on these premises, this multi-disciplinary research focused on developing naturally-derived coating materials for DES to increase their performance by improving physico-chemical characteristics, drug release, antioxidant properties, and enhancing hemocompatibility and endothelialization. The first project (Chapter 2) aimed to design and develop biodegradable and biocompatible zein-based bilayer coatings for DES with the ability to release rutin, a naturally-derived drug. Such antioxidant and anti-inflammatory active compound was chosen since inflammation after balloon injury plays an important role in the initiation and progression of restenosis, as described in Paragraph 1.1. Particular attention was dedicated to the exclusive use of green solvents and fabrication approaches. Release profiles, physico-chemical properties, and biocompatibility with endothelial cells and fibroblasts were examined for single and bilayered coatings.

Although the stenting procedure is well established, it is clear from clinical data that there is a large lack of comprehension of coatings impact in preventing thrombosis. As a more representative manner of studying stent-blood interaction would require three dimensionalities, the second project (Chapter 3) aimed to establish a microfluidic platform to study stent coatings behavior under dynamic conditions. The work presented here involved the development of a fused silica-based platform (with FLICE fabrication techniques), modeled to mimic the microenvironment of a healthy and obstructed stented artery in order to better investigate existing and novel DES coatings. Flowing whole mice blood and simulated blood fluids contributed to a deeper understanding of the dynamic impact of blood flow on the performance (e.g., matrix degradation and drug release kinetics) of the proposed sustainable, plant-based biomaterials.

Chapter 2 - Design and development of zein-based bilayer coatings for drug-eluting stents

2.1 Introduction

This chapter section is partially taken from Lenzuni M. et al., "Development of biodegradable zein-based bilayer coatings for drug-eluting stents" RSC Advances (2021).

As broadly discussed in Chapter I, the purpose of creating new coatings for DES is based on the need to reduce the side effects of their implantation. The carrier, often a polymeric matrix, keeps the selected drug in place, preserves its chemical stability, and, most importantly, manages its release kinetics. Long-term follow-up studies have revealed that patients with first-generation DES (i.e., Cypher and Taxus, described in Chapter 1, Paragraph 1.1.3) have an increased risk of stent thrombosis due to a delay in vascular healing and re-endothelialization, despite several clinical trials have endorsed the effectiveness of DES over BMS in blocking restenosis [152]. Durable synthetic polymers are frequently associated with complications such as persistent inflammation and adverse reactions at the implant site [153]. Additionally, the production of acidic by-products from non-permanent synthetic polymers like PLGA and PLLA might delay tissue repair and induce localized inflammation [154].

The use of naturally-derived polymers as coating materials for biomedical devices has recently attracted scientific interest since they combine biodegradability with other essential qualities, such as cell attachment and excellent biocompatibility. As discussed in Chapter 1, Paragraph 1.2.2, biopolymers physiologically break down into molecules of low molecular weight that can be readily excreted or assimilated by the body, resulting in reduced inflammation in long-term applications [154, 155]. However, a few of these materials present drawbacks when applied to the vascular system (e.g., thrombogenicity, low mechanical resistance, and mild immunogenicity) [83, 84]. Plant-based polymers are in high demand as an alternative to animal-based materials due to high availability, low cost, health advantages, and sustainability issues [85, 91]. Besides looking for new plant protein alternative sources, current research has focused on extraction methods, modification techniques, the addition of functional features, and the performance of plant-based proteins as structural building blocks of carrier systems [91]. As anticipated in Chapter 1, zein is a promising corn-derived protein and has been increasingly considered for biomedical applications [156]. Zein may be used as a vehicle for controlled drug release since it can form biodegradable and biocompatible matrices, has strong adhesive properties, and it is soluble in aqueous alcohol solutions but not in water [99, 113]. Moreover, zein could be easily transformed into a variety of

shapes and structures, such as films, nanoparticles, and fibers. More information on this plant-based protein can be found in Chapter 1, Paragraph 1.2.2.1.

Despite the wide range of drugs used in DES coatings, most currently authorized compounds (e.g., sirolimus, paclitaxel, zotarolimus, everolimus, dexamethasone) are deemed toxic and carry a high risk of adverse effects. Flavonoids are plant-based polyphenolic compounds with a wide range of biological functions and, as such, have attracted significant interest in CAD treatments due to their potential to lower the risk of cardiovascular diseases [157, 158]. Rutin (Figure 2.1), also known as quercetin-3-rutinoside, is a flavonoid extracted from different plants and fruits (e.g., buckwheat, tobacco, forsythia, viola, blackberry, quince, cherry) and offers noteworthy pharmaceutical efficacy as an antioxidant, anti-inflammatory, and antiplatelet compound [159, 160]. Additionally, rutin can enhance vascular functions and accelerate re-endothelialization by promoting the production of the basic fibroblast growth factor [161]. Rutin may thus be a suitable choice for future DES coatings, with the ability to minimize thrombosis and inflammatory events, reduce oxidative stress in surrounding tissues, and enhance endothelium healing.

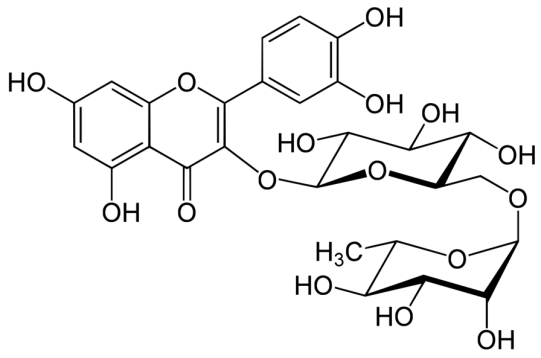

Figure 2.1. *Chemical structure of rutin.*

Currently, the most used techniques to produce DES coatings are dipping and spraying [162]. The process of dipping entails submerging the strut of the stent in a solution usually composed by one or more solvents, polymers, and drugs. Concentrations and timings may differ with the dipping procedure used, which is usually completed by gradually removing the stent, drying, and/or curing. Using the spray method, the solvent evaporates once the mixture has been applied to the stent. Depending on the required coating thickness, a multi-step coating may be used to create a multi-layered DES. An important concept to consider during spray coating is that all parameters must be optimized and then kept fixed. These include the distance between the airbrush tip and the stent, the solvent, the airflow, the time of spray, as well as the amount of polymer and drug dissolved in the solution.

In this first PhD project, naturally-derived double-layer coatings for DES applications were fabricated and characterized. An optimal composition for a plant-based bilayer coating is provided here,

comprising an active layer (a rutin-loaded zein matrix) and a sacrificial layer (cross-linked alginate), the latter providing a more controlled and sustained release of the underlying drug. Sodium alginate, a natural polysaccharide extracted from brown seaweed varieties, was chosen after a preliminary analysis for its ability to rapidly cross-link to form gel networks in the presence of calcium ions and prevent non-specific adsorption of blood proteins and platelets on the device surface, as suggested by the literature [163]. The exclusive use of green solvents and natural polymers of which the coating is composed can ensure complete biodegradation without harmful by-products. In this project, rutin release, antioxidant profiles, degradation analyses, as well as the physico-chemical characteristics of both single and double-layer coatings were investigated under simulated physiological conditions. Lastly, the biocompatibility of the constructed systems was assessed by evaluating how endothelial cells and fibroblasts adhere and proliferate on each polymeric substrate.

2.2 Materials & Methods

This chapter section is partially taken from Lenzuni M. et al., "Development of biodegradable zein-based bilayer coatings for drug-eluting stents" RSC Advances (2021).

2.2.1 Materials

Zein powder, rutin hydrate, alginic acid sodium salt, poly(ethylene glycol), 2,2-diphenyl-1-picrylhydrazyl free radical (DPPH•), 2,20-azinobis(3-ethylbenzothiazoline-6-sulfonic acid) diammonium salt (ABTS) and potassium persulfate ($K_2S_2O_8$) were provided by Sigma-Aldrich (St Louis, USA) and used as received without further purification. Granular calcium chloride ($CaCl_2$) was purchased from Merck KGaA (Darmstadt, Germany). Hyaluronic acid sodium salt (MW = 350,000) was purchased from ABCR (Karlsruhe, Germany). Commercial stainless steel (SS) springs (L = 15.7 mm, D = 2.75 mm) and flat sheets (316L SS, 500 mm x 300 mm x 0.5 mm) were purchased from RS Component (Milan, Italy). Dulbecco's Phosphate Buffered Saline (PBS), dimethyl sulfoxide (DMSO), and ethanol (≥ 99.8%) were purchased from Sigma-Aldrich (St Louis, USA), while deionized water (ddH_2O) was supplied by a Milli-Q Integral purification system (Millipore, Bedford, USA).

2.2.2 Fabrication of zein-coated substrates

To generate two-dimensional model substrates for coating deposition, 316L SS sheets were cut into squared pieces measuring 18 mm x 18 mm (herein referred to as "coupons"), while stainless steel springs were used as 3D models. Since zein has strong adsorption to hydrophilic surfaces, the SS springs

and coupons were initially ultrasonically cleaned with ethanol and deionized water for 10 minutes to remove impurities and then pretreated with O_2 plasma for 2 minutes at 100W using a Tucano plasma system (Gambetti Kenologia, Milano, Italy) to avoid the following peeling off of the coatings from substrates. This preliminary step allows for achieving a homogeneous thickness of the zein coating on a more hydrophilic substrate surface than traditional stainless steel. The rutin-loaded zein (ZR) solution was prepared by dissolving rutin powder in 5% v/v DMSO and diluting it with a combination of 76% v/v ethanol and deionized water (Figure 2.2a). Following that, zein powder was added to create a homogenous solution with 15% w/v zein and rutin 10% w/w_{zein}. The mixture was then stirred at room temperature for 60 minutes at a speed of 700 rpm until completely dissolved. (Figure 2.2b).

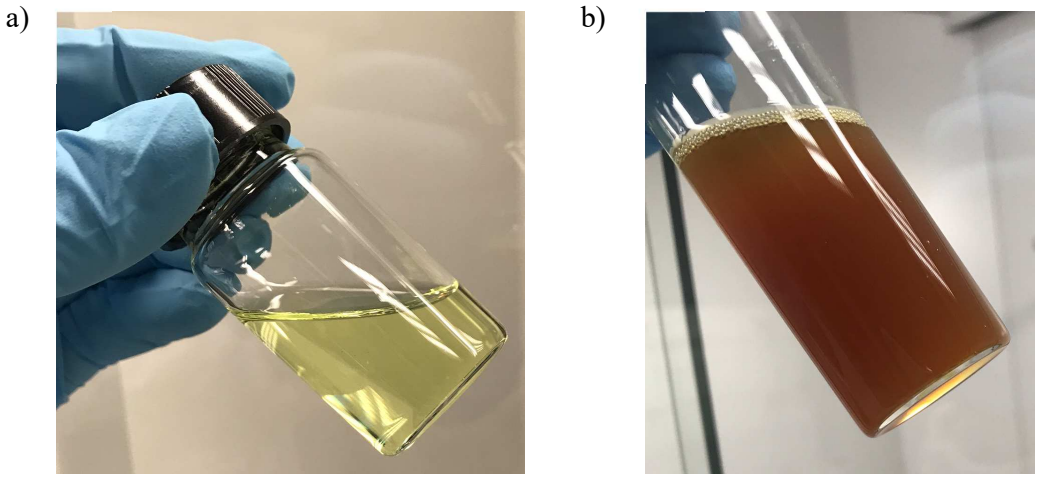

Figure 2.2. *Preparation of ZR solutions with the exclusive use of green solvents. A photograph of rutin dissolved in DMSO, ethanol, and water (a) and a photograph of the rutin-loaded zein (ZR) solution (b).*

Cleaned and pretreated stainless-steel springs and coupons were weighted by an analytical balance (ABT 120–5DM, Kern) with a level of accuracy of 0.01 mg and promptly dip-coated with the rutin-loaded zein solution. Briefly, the substrates were submerged for 10 seconds in a 50 mL glass beaker filled with the previously prepared mixture. The samples were then gradually removed from the solution and kept in a fume hood for 12 hours to allow any remaining solvents to evaporate and create a thin, hardened zein-based layer. The resultant substrates were weighed once again after the coating was applied. An indication of the coating volume deposited onto each substrate was given by the difference between the two weights compared to the weight of 1 mL of dried ZR solution. This data was then used to calculate the amount of zein and rutin deposited on each sample for the following characterizations.

2.2.3 Fabrication of sacrificial layers

With the aim of optimizing the sacrificial top layer, several materials were tested in a preliminary phase of the study: a 3% w/v sodium alginate solution (Alg) in ddH_2O, a 1% w/v hyaluronic acid (HA) solution in ddH_2O, a 1% w/v hyaluronic acid (HA) solution with 1% w/v PEG in ddH_2O (HA/PEG) and a 15% w/v zein (Z) solution in 80% v/v EtOH were prepared and applied by a dipping method on the dried ZR-coated samples. Alginate was chosen as the most suitable biopolymer for the sacrificial layer, and a two-step ionic cross-linking procedure was carried out using a 10% w/w $CaCl_2$ ethanolic solution (1.35 M, containing 75% v/v EtOH). In particular, using an airbrush spray instrument (0.55 mm nozzle diameter, model VL-SET, Paasche Airbrush Company, Chicago, USA), the calcium chloride solution was sprayed onto the ZR/Alg-coated surfaces, and the samples were subsequently immersed in the same $CaCl_2$ solution for additional 15 seconds to achieve a uniform cross-linked layer. Prior to characterization, the resultant samples (ZR/cAlg) were dried overnight at room temperature. Table 2.1 lists the formulation details used for the chosen plant-based bilayer coating.

Table 2.1. *Drug-polymer formulations for the bilayer coating.*

Layer	**Matrix Material**	**Functional Molecule**
Active layer **(ZR)**	Zein 15% w/v in ethanol/ddH_2O /DMSO (76:19:5 v/v)	Rutin 10% w/w_{zein}
Sacrificial layer **(cAlg)**	Alginate 3% w/v in ddH_2O + $CaCl_2$ 10% w/v in H_2O/ethanol (25:75 v/v)	___

2.2.4 Surface topography

Scanning electron microscopy (SEM) is a characterization technique that allows for high-resolution three-dimensional viewing of the sample surface. SEM JSM-6490LA microscope (JEOL Inc., Peabody, USA) at 10 kV accelerating voltage was used to analyze the morphologies of the coated SS samples. To increase the electrical conductivity of the surfaces, the specimens were placed on conductive carbon tape, mounted on SEM stubs, and sputter-coated with a 10 nm coating of gold. At various magnifications, digital photographs of surface topographies and cross-sections were obtained.

Additional coated specimens were manually scratched with a lancet, and their thickness was measured with a profilometer (Ambios XP-2, Ambiostech, Santa Cruz, USA) equipped with a diamond-tipped stylus. A constant load of 0.5 mN with a speed of 0.5 mm/s was applied to the stylus tip (radius = 2 μm). The average roughness of each layer was calculated using similar parameters. In particular,

the stylus tip was used to draw a straight line of 2 mm on each sample, and the in-built software XP-2 was used to determine the arithmetic roughness of each sample over the drawn path.

2.2.5 Fourier-transform infrared spectroscopy

Infrared (IR) spectroscopy is based on the transfer of energy from radiations to molecules through molecular absorption, which happens when the wavelength of an incoming IR radiation matches the frequency of oscillation of a molecular bond. Stretching, bending, and other movements are considered molecular oscillations (vibrations). The absorption intensity may be used to identify the kind of molecular vibrations and the functional groups present in a sample since each motion entails an oscillation at a particular frequency (or wavelength or wavenumber). An infrared spectrometer (Vertex 70 FT-IR Spectrometer, Bruker, Germany) was used to collect Fourier Transform Infrared (FTIR) spectra of the prepared substrates. ATR (Attenuated Total Reflection) measurements were taken between 4000 and 750 cm^{-1}, with 32 scans at a resolution of 4 cm^{-1}.

2.2.6 X-ray photoelectron spectroscopy

X-ray photoelectron spectroscopy (XPS) belongs to the class of surface characterization methods based on the study of the energy of the electrons emitted from the surface of a sample irradiated with an X-beam towards the external environment under vacuum conditions. By measuring the kinetic energy of the photoemitted electrons, the XPS technique can give information on their binding energy, uniquely identifying the atomic species in the sample. Here the chemical components of the coated surfaces were studied on an electron spectrometer (Lab2, Specs, Berlin, Germany) equipped with a monochromatic X-ray source (set at 1486 eV) and a hemispherical energy analyzer (Phoibos, HSA3500, Specs, Berlin, Germany). The applied voltage and current of the Al Kα X-ray source were adjusted at 13 kV and 8 mA, respectively. The analytical chamber had a pressure of ~ 1×10^{-9} mbar. The resulting spectrum is composed of different peaks at very precise energies: each of them corresponds to an energy level and, thus, to a chemical element.

2.2.7 Water contact angle measurements

The wettability to water can be measured via contact angle analysis by means of a water droplet deposited on the material surface. This parameter has significant consequences for biomaterials exposed to *in vivo* aqueous environments, such as stents in the vascular system. It drives protein adsorption to the surface and influences the structural shape of adsorbed plasma proteins. The interaction between a blood-contacting material and blood cellular components is conveyed through a rapidly adsorbed

protein layer, as previously described in Chapter 1, Paragraph 1.1.1. Using a contact angle goniometer (Dataphysics OCA 20, Filderstadt, Germany) and the sessile drop technique, static contact angle measurements were calculated for the coated coupons. By means of a microsyringe, 5 µL droplets of ddH_2O were placed on each sample surface in ten separate places, and the acquired images were elaborated using the SCA 20 Software (Data Physics Instruments GmbH, Filderstadt, Germany). The angle between the drop baseline and the tangent at the drop boundary was calculated, and the contact angle measurements were computed by taking the arithmetic average of the left and right contact angles from each droplet. Generally speaking, a surface is thought to be hydrophilic (high wettability) if the contact angle is less than 90 degrees, and hydrophobic if the angle is more than 90 degrees (low wettability).

2.2.8 Mechanical analysis

The adhesion is a critical property to investigate for improving the long-term reliability of polymer-coated stents. Coating failures (e.g., delamination, fracture, cracks), mainly related to lack of interfacial and cohesive adhesion, could induce major complications, such as thrombogenesis. However, to date, no specific adhesion test for coated stents has been reported by the FDA [164]. Here, scratching tests were conducted with a Micro-combi Tester (Anton-Paar, Peseux, Switzerland) and a diamond conical indenter with a 0.1 mm diameter to determine the critical load values (i.e., the load at which the coating begins to delaminate at the borders of the scratch track) of the proposed coatings on stainless steel. A 5 mm scratch test was performed on the samples' surfaces, with a progressive load ranging from 30 to 1000 mN and a 5 mm/min speed rate. Three distinct spots on each coating were used to confirm the uniformity of the deposition process, and optical microscopy was used to verify the critical load values obtained.

2.2.9 Coating degradation and drug release studies

A zein solution (15% w/v) in 80% v/v EtOH was used to coat SS coupons in order to evaluate the kinetics of polymer degradation in PBS buffer. In 6-well plates, several precisely weighted samples (both before and after the zein coating) were inserted at the bottom of each well filled with 3 mL of PBS (pH 7.4). In order to mimic the blood flow and the physiological milieu of the human body, the plates were covered with parafilm and put in an incubation shaker with continuous agitation (75 rpm and 37 °C). The incubation medium was entirely removed for analysis at defined time points (varying from 15 minutes to 21 days), and 3 mL of fresh PBS were immediately replaced into each well. A Cary 6000i UV-Vis-NIR spectrophotometer (Varian, Palo Alto, USA) was used to measure absorbance at 270 nm (zein λmax), and the quantity of zein released from each coupon was computed using an

appropriate calibration curve. The results were reported as the cumulative percentage of degraded zein as a function of incubation time using Equation (1).

$$Cumulative\ amount\ of\ degraded\ zein\ (\%) = \frac{Mass\ of\ zein\ into\ the\ medium\ (at\ time = t)}{Total\ mass\ of\ zein\ (at\ time = 0)}\ x\ 100 \qquad \text{Eq. (1)}$$

Similar criteria were used to evaluate rutin released from various coated SS coupons (either with one or two layers). To create a calibration curve and quantify the concentration of the active component in the incubation medium at each time point, solutions with known concentrations of rutin dissolved in PBS were utilized. The absorbance at 360 nm (rutin λmax) was recorded, and Equation (2) was used to represent the results as the cumulative percent of rutin released as a function of the incubation time.

$$Cumulative\ amount\ of\ released\ rutin\ (\%) = \frac{Mass\ of\ rutin\ into\ the\ medium\ (at\ time =\ t)}{Total\ mass\ of\ rutin\ initially\ loaded\ (at\ time = 0)}\ x\ 100 \qquad \text{Eq. (2)}$$

A reference sample was selected at the end of fixed time points, rinsed with deionized water, and vacuum dried for 24 hours to determine the existence of surface morphological changes during the studies. SEM was used to observe morphological features of the degraded coatings, as previously described in paragraph 2.2.4. Using the ImageJ analysis software (Wayane Rasband, NIH, http://rsbweb.nih.gov/ij/), a porosity analysis was performed on acquired images to determine the mean pore sizes and pore size distribution curves. On average, 200 pores from three different SEM micrographs were manually analyzed for each time point.

2.2.10 Antioxidant assays

The $ABTS^{\bullet+}$ and $DPPH^{\bullet}$ assays are extensively used methods for assessing the antioxidant capabilities of natural and synthetic products; both are spectrophotometric procedures based on the quenching of stable colored radicals ($ABTS^{\bullet+}$ or $DPPH^{\bullet}$) and demonstrate the antioxidant capacity of a molecule/system to scavenge radicals. These assays were used in this study to assess and confirm rutin scavenging ability after the coating preparation steps and long-term release assays. For the $ABTS^{\bullet+}$ test, the radical cation was produced by mixing a 7.0 mM solution of ABTS in ddH_2O with a 2.45 mM solution of potassium persulfate. The mixture was kept in the dark for 15-16 hours until the reaction was completed and the absorbance at 728 nm was stable. The $ABTS^{\bullet+}$ solution was then diluted with deionized water to achieve an absorbance of 1.00 ± 0.02 at 728 nm. At predetermined time intervals, an aliquot of the extracts (150 µL) was mixed with 1850 µL of $ABTS^{\bullet+}$ diluted solution, and the absorbance was measured using a UV-Vis spectrophotometer after 1 minute. The absorbance of a control sample containing 150 µL of PBS was measured similarly, and a rutin stock solution in PBS and its diluted

products were used for comparison. The $ABTS^{\bullet+}$ scavenging ability of each sample was determined according to Equation (3), where A_0 is the absorbance of the radical control solution, and A_1 is the absorbance of the radical solution after adding the extract.

$$Radical\ Scavenging\ Activity\ (\%) = \frac{(A_0 - A_1)}{A_0}\ x\ 100 \qquad \text{Eq. (3)}$$

The $DPPH^{\bullet}$ free radical scavenging method was also employed to assess the antioxidant capability of the released samples. To create a 0.2 mM solution, $DPPH^{\bullet}$ powder was dissolved in ethanol and stirred for 30 minutes. Cuvettes containing aliquots of 150 µL of the extracted sample solutions and 1 mL of the $DPPH^{\bullet}$ solution were incubated for 30 minutes at room temperature in the dark. A UV-Vis spectrophotometer was then used to detect their absorption at 522 nm. Similarly, the absorbance of a control sample with 150 µL of PBS was measured, and, for comparison, a rutin stock solution in PBS and its diluted products were employed. The $DPPH^{\bullet}$ scavenging activity of each sample was calculated using Equation (3).

2.2.11 *In vitro* studies with human umbilical vein endothelial cells

Human umbilical vein endothelial cells (HUVEC, Carlo Erba, Italy) were used to test the biocompatibility of glass coverslips (12 mm Ø) coated with ZR and ZR/cAlg. The samples were UV-sterilized and placed on a 24-well plate (1.9 cm^2). Cells were seeded onto each slide at a density of 10 x 10^5 cells per well and cultured for 24 and 48 hours at 37 °C in an incubator humidified with 5% CO_2. Standard controls were cells grown in a growth medium. The HUVEC vitality after each experiment was determined using the alamarBlue™ assay (Thermo Fisher, Italy): briefly, cells were washed once with pre-warmed PBS before being treated for 3 hours at 37°C with DMEM without red phenol (with 4.5 g/L glucose, ampicillin, sodium pyruvate, and without L-glutamine) containing 10% v/v alamarBlue™. A microplate reader (FLUOstar Omega Microplate Reader, BMG LabTech, Ortenberg, Germany) was used to measure the fluorescence intensity (excitation wavelength, 544 nm; emission wavelength, 590 nm) from each well. Four repetitions were performed for each type of sample, and the fluorescence results were compared using a one-way ANOVA (i.e., analysis of variance) followed by a post-hoc Tukey HSD statistical test. Differences were considered statistically significant at a level of $p < 0.05$.

Furthermore, cells cultured for 48 hours on each sample (ZR- and ZR/cAlg-coated glass slides with Ø = 13 mm) were fixed for 2 hours at room temperature with a 3% v/v glutaraldehyde solution in PBS. The substrates were then washed three times with PBS before staining the cellular cytoskeleton and nuclei for 40 minutes in the dark with 150 µL (50 µg/mL) of Phalloidin-Atto 488 (Sigma-Aldrich, Italy) and 10 minutes in the dark with 250 µL of Hoechst 33258 (Sigma-Aldrich, Italy), diluted 1:10000

in PBS. Samples were photographed using a Confocal Laser Scanning Microscope (CLSM, Leica TCS SP2, Leica Microsystems, Italy) at λex = 501 nm and λem = 523 nm for Phalloidin-Atto 488 and λex = 346 nm and λem = 460 nm for Hoechst 333258 dyes.

2.2.12 *In vitro* studies with human dermal fibroblasts

To further confirm the biocompatibility of the manufactured plant-based coatings, adult primary human dermal fibroblasts (HDFa, Thermo Fisher Scientific, Italy) were utilized as an additional cellular model. Cells were cultivated in T75 culture flasks in an incubator at 37 °C and 5% CO_2 in the presence of Medium 106 (under low-serum growth supplement, Thermo Fisher Scientific, Italy). For the biocompatibility assays, fibroblasts were seeded at a density of 7000 cells/cm^2 onto 24-well plates and allowed to attach overnight. Following the ISO10993-5:2009 standard test, the extraction medium from the coatings was prepared. Briefly, the samples (ZR coatings and ZR-cAlg coatings deposited onto 18 mm x 18 mm glass coverslips) were placed into 35-mm Petri dishes and sterilized under UV light for 20 minutes (10 minutes per side). One mL of culture medium was added to each plate, and the wet samples were left at 37 °C for 24 hours. The attached HDFa were treated with 0.5 mL of the extraction medium the following day and cultured for 24 or 48 hours, while cells incubated in standard conditions were used as controls. The MTS test (tetrazolium salt, CellTiter 96® AQueous One Solution Cell Proliferation Assay, Promega, USA) was performed to evaluate fibroblast viability. In particular, the MTS compound is reduced by the mitochondrial NADPH- or NADH-dependent dehydrogenase enzymes of viable cells into purple formazan, soluble in the culture medium; the intensity of the purple color developed is directly proportional to the number of viable cells. Following established protocols, after 24 or 48 hours of incubation, cells were rinsed with 0.5 mL fresh culture medium [93, 94, 102]. A volume of 25 µl of the MTS reagent was added to each specimen and incubated at 37°C for 3 hours. 200 µl from each well was then placed into a 96-well plate, and the absorbance at 490 nm was measured with a microplate reader. One-way ANOVA with post-hoc Tukey HSD test was used for statistical analysis. Differences were considered statistically significant at a level of $p < 0.05$.

In addition, fibroblasts were grown onto glass coverslips at a density of 5000 cells/cm^2 and treated as previously described to observe the morphology of cells exposed to ZR coatings and ZR-cAlg coatings extracts. After 24 and 48 hours of treatment, cells were rinsed with pre-warmed PBS and fixed for 20 minutes in 3.7% v/v paraformaldehyde. The nuclei were stained for 15 minutes in the dark with DAPI (2.5 µg/mL in PBS; Sigma-Aldrich, Italy). The samples were then permeabilized for 8 minutes with 0.3% v/v Triton X-100 and rinsed twice with PBS before being incubated for 20 minutes in the dark with Alexa Fluor® 488 Phalloidin (Thermo Fisher Scientific, Italy), diluted 1:100 in PBS. The coverslips were mounted on glass slides with Fluoromont-G medium (Sigma Aldrich, Italy) and photographed using a Nikon A1 confocal microscope (equipped with 405 nm and 488 nm lasers).

2.3 Results & Discussion

This chapter section is partially taken from Lenzuni M. et al., "Development of biodegradable zein-based bilayer coatings for drug-eluting stents" RSC Advances (2021).

2.3.1 Surface topography of zein-based coatings

Following solvent and oxygen plasma cleaning, the SS surfaces were manually dipped in the rutin-loaded zein solution (ZR). The resulting coatings appear homogeneous and smooth both to the naked eye and under the SEM, as seen in Figure 2.3a. Small holes in the ZR film, also visible in the cross-sectional picture (Figure 2.3b), are most likely the result of the solvent (ethanol) evaporating quickly during the drying process.

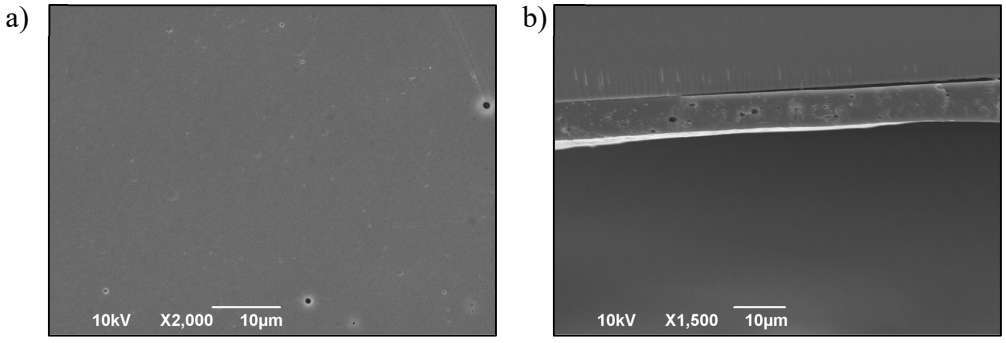

Figure 2.3. *Morphological analysis of flat, ZR-coated samples. SEM micrographs of the rutin-loaded zein coatings, with the surface (a) and cross-sectional (b) views of a stainless steel-coated coupon.*

The coated surface of a stainless-steel spring, which resembles the curved structure of a stent, also resulted homogeneous and free of fractures (Figure 2.4a).

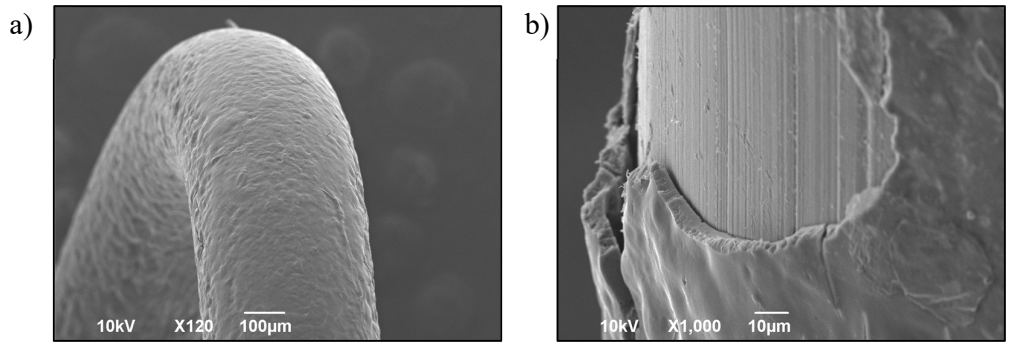

Figure 2.4. *Morphological analysis of ZR-coated springs. SEM micrographs of the rutin-loaded zein coatings, with the surface (a) and cross-sectional (b) views of a stainless steel-coated spring.*

After the samples were purposefully scratched with a lancet, the ZR layer thickness on SS coupons was measured with a stylus profilometer. The coating thickness was 6.9 ± 0.8 μm (Figure 2.5), which is comparable to the results from the analysis of SEM cross-sectional pictures, which yielded values of 7.2 μm and 7.1 μm from Figures 2.3b and 2.4b, respectively. Moreover, the measurements with the profilometer allowed the assessment of the arithmetic roughness of the flat, coated surfaces, which was 219.2 ± 6.8 nm.

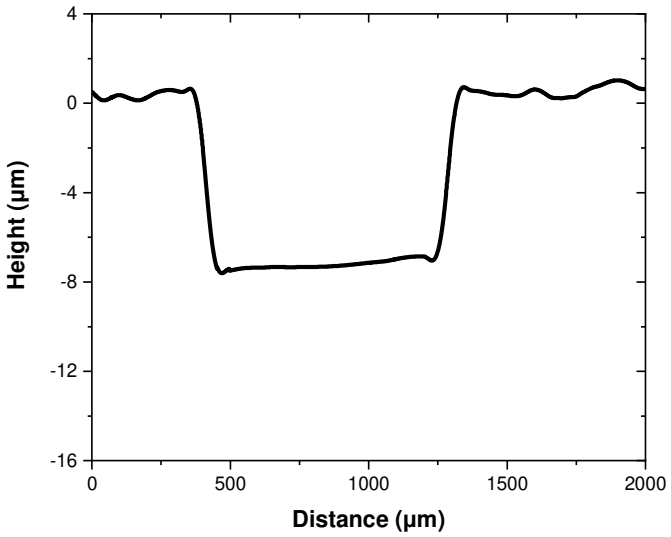

Figure 2.5. *Thickness and roughness measurements of a previously scratched ZR-coated sample. The analysis was performed with the surface profilometer.*

2.3.2 Single layer characterization: Fourier-transform infrared spectroscopy

Both ATR-FTIR and XPS performed a chemical analysis of the drug-loading layer. Figure 2.6 depicts the FTIR spectra of zein, rutin, and ZR films, while Table 2.2 presents a list of the relative IR absorption peaks and their assignments. Zein spectrum shows four characteristic bands: around 3229 cm^{-1} appears the amide A band corresponding to the stretching of the N–H and O–H bonds of the amino acids of the protein. At 1641 cm^{-1}, a second band known as amide I can be seen. This band is caused by the carbonyl (C=O) stretching of amide groups found in peptide bonds. The amide II band, located at 1533 cm^{-1}, mainly results from in-plane N-H bending (40% - 60%) and C-N stretching (18% - 40%) vibrations in secondary amides. Finally, the range between 1300 and 1242 cm^{-1} (amide III) corresponds to the bending and stretching vibrations of N-H and C-N bonds [102, 156, 165]. The symmetrical spectral peak at 1641 cm^{-1} supports the existence of a higher quantity of α-helices in the secondary structure of zein. Characteristic stretching bands were identified in the IR spectrum of rutin at 1653, 1452, and between 1358 and 1287 cm^{-1}, attributable to C=O, C=C, and C-O bonds, respectively.

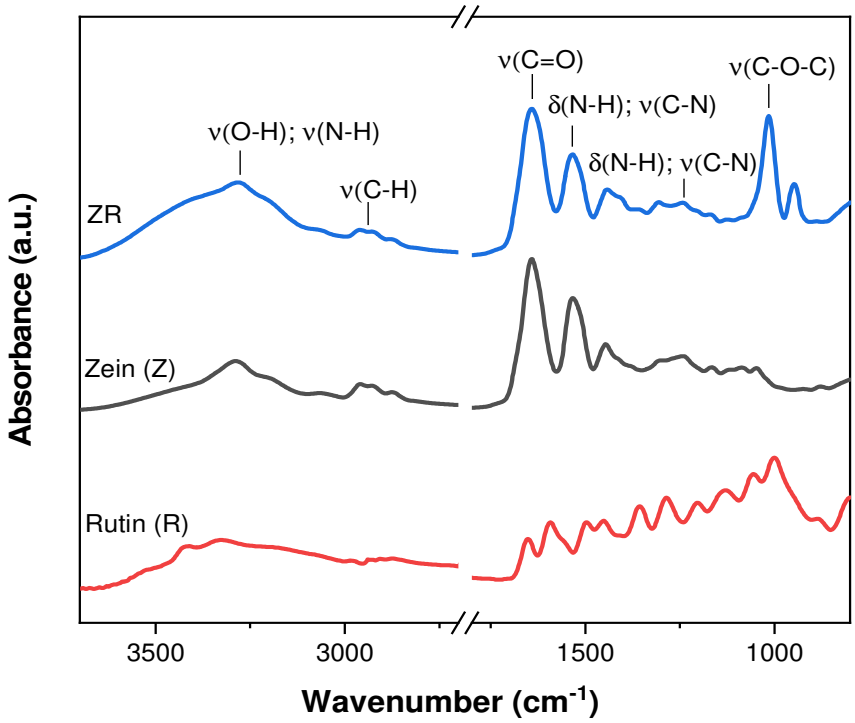

Figure 2.6. *FTIR spectra of rutin powder, zein, and rutin-loaded zein (ZR) films.*

Table 2.2. *Characteristic FTIR absorption bands assigned to vibrational modes of zein, rutin, and rutin-loaded zein functional groups.*

FT-IR peaks (cm^{-1})			**Vibrational mode**
Pure Zein	Pure Rutin	Rutin-loaded Zein	
3229	3327	3283	Amide A (ν(O-H), ν(N-H))
2959-2876	2986-2874	2961-2882	ν(C-H)
1641	1653	1641	Amide I (ν(C=O)), ν(Ar-C=O)
1533		1533	Amide II (ν(C-N), δ(N-H))
1447	1452	1443	δ(C-H), ν(C=C aromatic ring)
	1358	1360	δ(C-OH)
1300-1242	1287	1306-1242	Amide III (δ(N-H), ν(C-N)), ν(C-C-O)
	1204	1204	ν(C-O-C)
1165		1171	ν(C-N)
1117	1132	1124	ν(C-OH), ν(C-O-C)
	1001	1015	ν(C-O)
	943	947	ν(C-C)

On the right side of the ZR spectrum, distinct peaks of rutin are visible, particularly those indicating the aromatic moiety, the C-O and C-O-C bonds of the flavonoid structure, confirming drug incorporation into the protein film. The two types of polymeric films (zein and rutin-loaded zein) had comparable spectra patterns, and no unassigned peaks appeared, suggesting that no covalent chemical interactions occurred between the drug and the polymer during the coating production process. The shifting of the O-H stretching vibration peak of zein from 3229 to 3283 cm^{-1} following rutin loading suggests that FTIR spectra can also reveal information regarding hydrogen bonding among components in ZR films. Similar small shifts demonstrate how hydrogen bonding, van der Waals, and electrostatic forces contribute to the film structure following solvent evaporation.

2.3.3 Single layer characterization: X-ray photoelectron spectroscopy

XPS spectroscopy allows the identification of chemical elements in the surface layers of selected materials, the determination of their binding state, and the quantification of their atomic percentage. The surface composition of zein and ZR films was investigated, and the associated chemical percentages are presented in Table 2.3.

Table 2.3. *Atomic percentages of the elements obtained via XPS analysis of zein and rutin-loaded zein (ZR) films.*

	Atomic Percentage (%)		
	C 1s	O 1s	N 1s
Zein	73.3	16.1	10.6
Rutin-loaded Zein	77.7	14.5	7.8

The integration of rutin into zein films reduces the percentages of nitrogen (N) and oxygen (O) atoms on the surface while increasing the amount of carbon (C) atoms. This finding reveals the existence of rutin near the sample surface due to its high carbon content and lack of nitrogen atoms (Figure 2.1).

2.3.4 Single layer characterization: mechanical analysis

A scratch test was performed to determine the force required to remove the ZR coating from the steel substrate. An increasing load, from 30 to 1000 mN, was applied to define the critical load value, which was 321.8 ± 50.2 mN, as reported in Figure 2.7a. The coating completely delaminates

from the metal substrate when this value is reached, as illustrated in Figure 2.7b. Generally speaking, the higher the critical load, the more scratch-resistant and sticky the coating is to the substrate.

There is currently little information in the literature concerning the adhesive strength of polymeric coatings on SS stents. As a comparison, the critical load value obtained from ZR-coated samples is much higher than that obtained from a chitosan-silica coating (52.0 mN). However, a more negligible difference is evident when comparing PDLLA (550 mN), even though adhesion experiments were performed on cobalt-chromium substrates [166, 167].

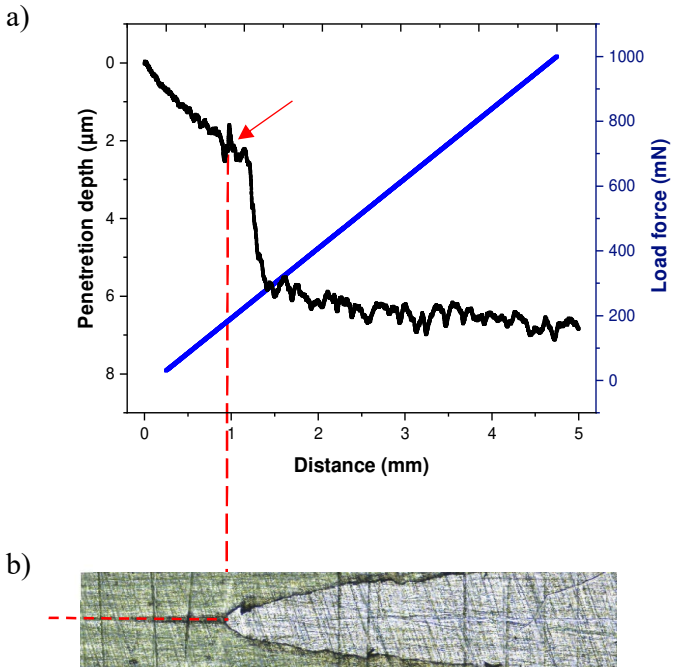

Figure 2.7. *The load-displacement curve and the corresponding optical image of the ZR-coated specimen. A red dotted line was drawn in order to compare the curve with the optical image of the scratch path and to determine the exact critical load value for each sample. The arrow indicates the drop in the penetration depth signal, which corresponds to the critical load at the onset of coating cracking.*

2.3.5 Coating degradation and release profiles

Zein-coated SS coupons were incubated in a warmed PBS buffer for 21 days to monitor the degradation behavior. A preliminary analysis of the samples coated with a drug-free polymer layer was conducted in order to evaluate the matrix reaction in a water-like environment. Figure 2.8 presents the results of the polymer degradation study, which appears biphasic with an initial rapid degradation over the first 3-4 days, followed by a slower but steady degradation rate for the next 20 days. The amount of zein degraded was determined according to Equation (1). Within 21 days, the samples released approximately 55% of the zein polymer mass initially deposited on each coupon, indicating that the

protein coating was slowly breaking down by gradual hydrolysis. In fact, it is well known that the primary cause of protein degradation in aqueous conditions is the hydrolysis of the peptide bonds in the backbones of the macromolecules [91]. However, in comparison with other natural proteins, such as soy protein and whey protein, zein resistance to aqueous degradation and dissolution is higher due to its hydrophobic nature [168].

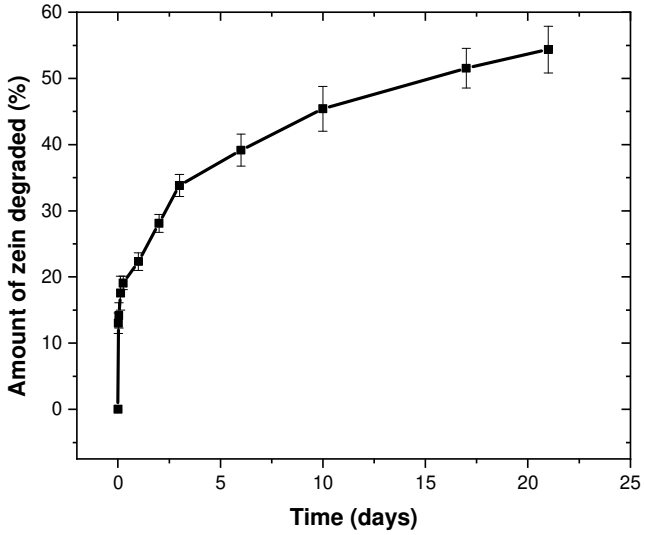

Figure 2.8. *Matrix degradation kinetics from zein-coated SS substrates.*

Zein was then investigated as a possible drug-encapsulating polymer. Figure 2.9 depicts the rutin release curve from ZR-coated coupons, calculated as the cumulative percentage of drug released as a function of time, using Equation (2). According to the release profile, rutin elution from ZR coatings is due to the drug diffusion mechanism, which is facilitated by the swelling of the zein polymeric layer. A diffusional-degradation controlled phase follows this burst effect up to the conclusion of the experiment as a result of hydrolysis and penetration of water molecules inside the zein matrix. Approximately 90.6% of the drug is lost during the first 24 hours, and a total release of 98.7% occurred throughout 21 days. The results obtained from the ZR single-layer system are consistent with earlier work on drug-eluting zein matrices [165, 169, 170].

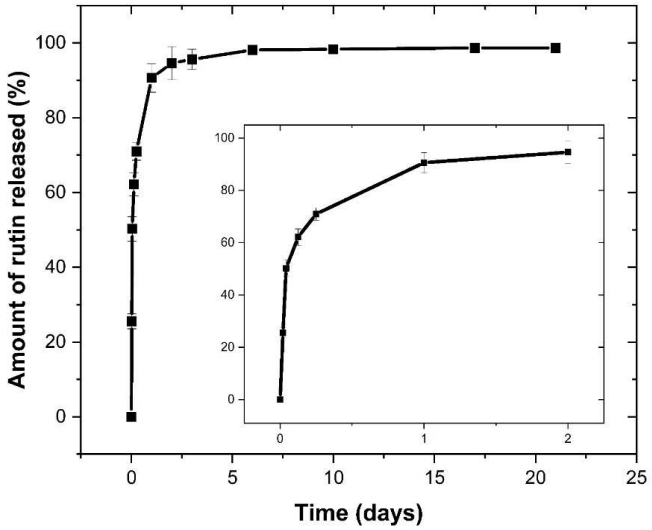

Figure 2.9. *Cumulative rutin release profile from ZR coatings, with an inset highlighting the release kinetics between 0 and 2 days.*

Zein shows a faster biodegradability when compared to synthetic degradable polymers, such as PGA, PLGA, PLLA, and PCL, which exhibit degradation times of more than 3, 6, 24, and 30 months, respectively, as anticipated in Chapter 1, Paragraph 1.2.1 [171]. For example, Pan *et al.* found a 60% mass loss for PLGA-coated films after three months in PBS, while after 18 days of incubation, almost 70% of the curcumin loaded was released. [172]. The literature frequently reports slow but incomplete releases of hydrophobic drugs from synthetic degradable polymers, including curcumin, sirolimus, and paclitaxel. Kim *et al.* investigated the sirolimus release kinetics from PLGA-coated stents, finding that there is an early burst release (about 51% after two days) and that 69% of the drug is freed after 28 days [173]. Similarly, Bedair *et al.* noticed an initial burst release of sirolimus from PDLLA-coated substrates and the complete detachment of the coated layer after 28 days of incubation in PBS [166]. However, these early burst releases in DES are undesirable, especially when potentially hazardous drugs like sirolimus are used. Regarding materials with natural origins, studies on blend films using polymers made from bacteria, such as poly(3-hydroxyoctanoate) and poly(3-hydroxybutyrate), have shown 97% of aspirin released over 25 days. However, this slow and controlled drug-release rate is only seen when the drug is present in the polymer crystalline regions [174]. In a separate experiment, silk-fibroin films treated with ethanol displayed a delayed but incomplete release of sirolimus (41% after one day and 64% after 14 days) [175]. Given that most commercially available devices are covered with synthetic polymers that do not entirely degrade after releasing their drugs and result in adverse side effects, these findings are encouraging for the successful construction of a safe DES.

2.3.6 Morphological changes during degradation assays

After thoroughly washing the samples in deionized water, the morphological changes that occurred during drug release and degradation assays were examined by SEM (Figure 2.10).

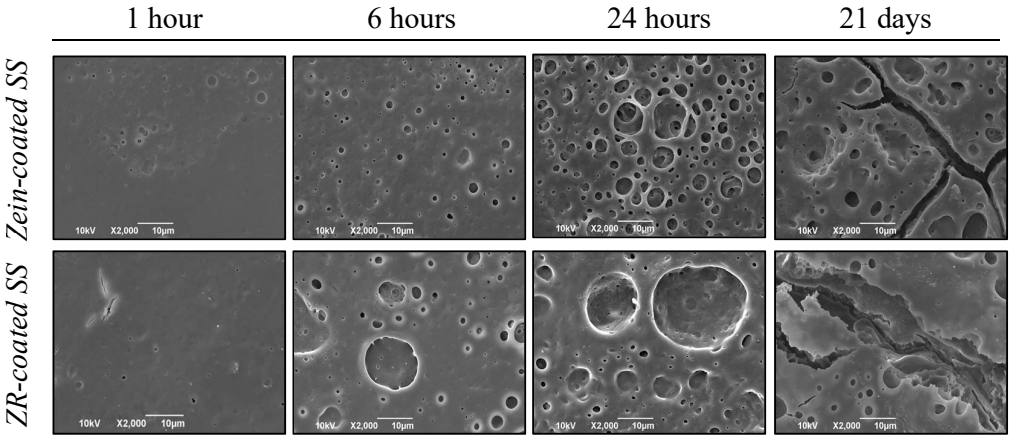

Figure 2.10. *SEM images of zein and ZR coatings after different incubation times. Pitting, craters and cracks are more visible with time.*

Although both coatings (drug-free and drug-loaded) seemed intact to the naked eye even after many days of exposure to the aqueous environment, SEM pictures indicated a degree of surface degradation beginning within the first few hours. Based on these data, it is feasible to conclude that polymer hydrolysis occurs equally across the matrix (i.e., surface erosion, as described in Chapter 1, Paragraph 1.1.4). Small holes with average sizes of 1.9 and 2.1 μm appear on the surfaces of zein and ZR films after a brief period of PBS incubation (Table 2.4). These pores are the earliest evidences of coating degradation. The materials exhibit deeper and larger holes during extended testing periods, with mean diameters growing and distributions becoming denser. Table 2.4 and Figure 2.11 report the analysis of the pore diameters changing over time. Interestingly, pores tend to merge over time to generate bigger cavities and surface fractures, as seen in Figure 2.10.

Table 2.4. *Values of the mean and median diameters of the pores observed in SEM images.*

	Zein-coated SS substrate		**Rutin-loaded Zein-coated SS substrate**	
	Mean pore diameter (μm)	Median pore diameter (μm)	Mean pore diameter (μm)	Median pore diameter (μm)
1 hour	0.866	0.757	0.479	0.429
6 hours	1.891	1.674	2.130	1.584
24 hours	3.341	3.012	4.748	2.755

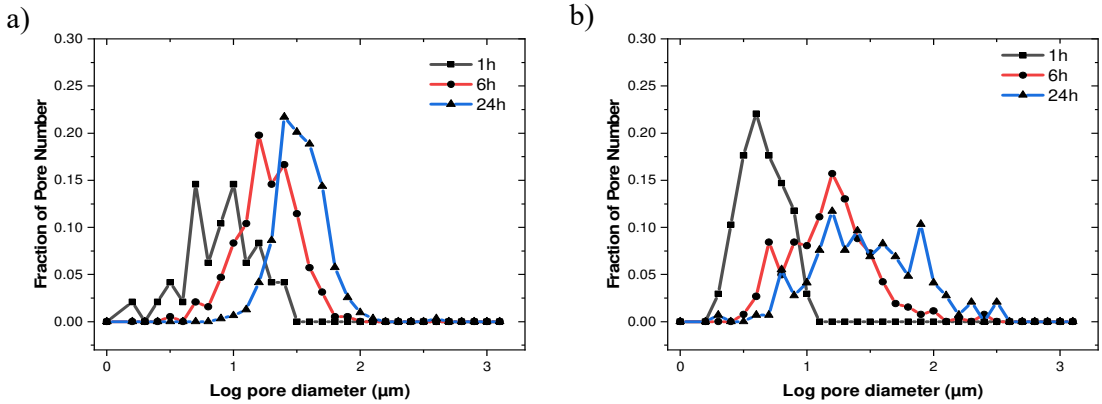

Figure 2.11. *Pore size distribution on degrading zein-based coatings. The pore size distribution was quantified from the SEM images of zein- (a) and ZR- (b) coated samples using ImageJ software. On average, 200 pores from 3 different SEM micrographs were analyzed for each time point.*

2.3.7 Surface topography of bilayer coatings

The ZR/cAlg bilayer coating on SS surfaces was applied in four steps, as shown in Figure 2.12. The 3% w/v alginate solution was applied to the dried ZR surface using a similar dip-coating procedure. Following that, a 10% w/w calcium chloride solution in 75% v/v EtOH was sprayed over the alginate layer with a spray gun system, and subsequently, the substrate was dip-coated in the same solution. As already demonstrated in the literature, the presence of calcium ions creates cross-linking bonds between the carboxyl groups of guluronic residues from distinct alginate chains, creating an "egg-box" shape with calcium ions at the core [176]. Cross-linked alginate was added as a sacrificial layer on top of the ZR active coating to inhibit alginate matrix dissolution in aqueous environments, protect the bottom layer from light and moisture, and fine-tune the drug release rate from the underlying rutin-loaded layer.

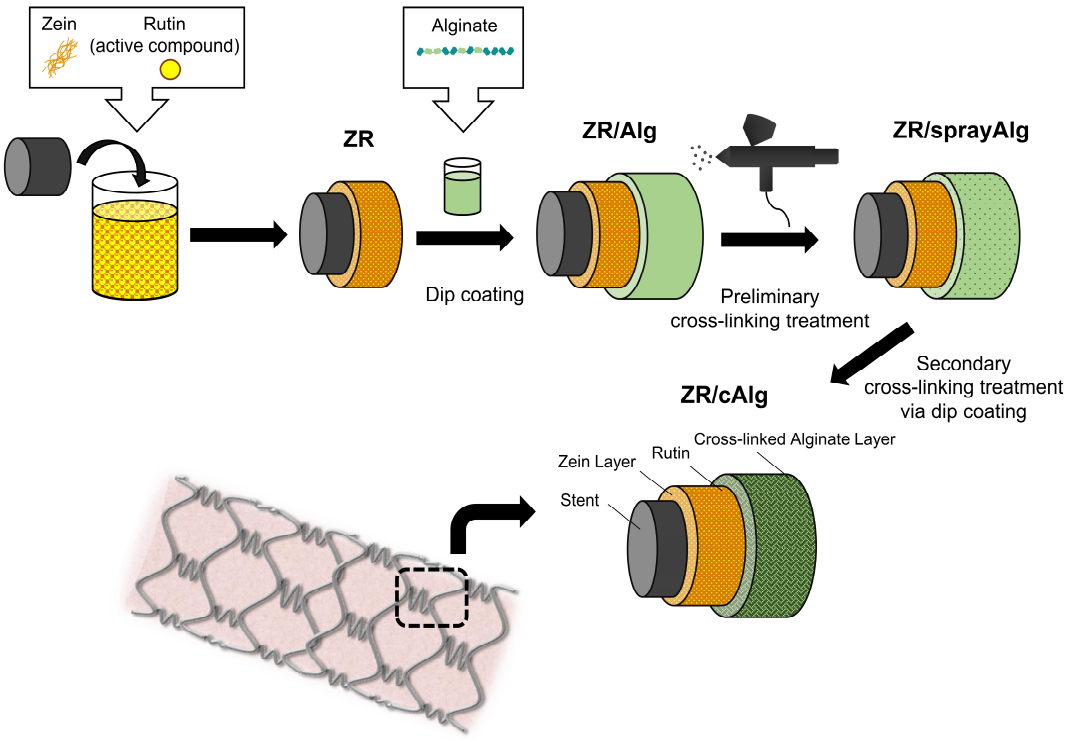

Figure 2.12. *Schematic illustration of the fabrication process and the 3D cross-sectional final rendering of the bilayer coating on stainless steel substrates (e.g., stent).*

Adding ethanol into the $CaCl_2$ water solution was necessary to avoid the dissolution of the underlying alginate layer during spray and dip coating procedures. Moreover, Li *et al.* claimed that such alcoholic solutions could improve the surface homogeneity and mechanical properties of alginate films, which can be attributed to the reduced swelling degree during the cross-linking process [176]. The surface morphologies and cross-sectional microstructures of the resulting ZR/cAlg bilayer coating on the flat substrates were examined using SEM, as shown in Figure 2.13. Both images reveal a homogeneous layer with minimal structural defects, which is essential to ensure uniform drug delivery and the hemo- and cytocompatibility of the resulting device.

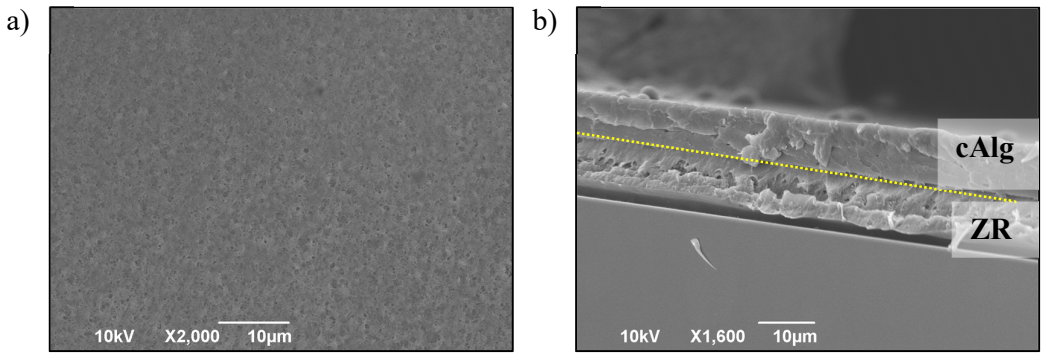

***Figure 2.13**. Morphological characterization of the ZR/cAlg bilayer coating on flat substrates. SEM micrographs of ZR/cAlg layers, with the surface (a) and cross-sectional (b) views of a stainless steel-coated coupon. The yellow dotted line in (b) delimits the separation between the two layers.*

Figure 2.14 depicts SEM micrographs of the coated SS springs after cutting them with shears. As a result of this cut, a slight delamination of the coating occurred from the substrate, highlighting the bilayer structure along the coated spring.

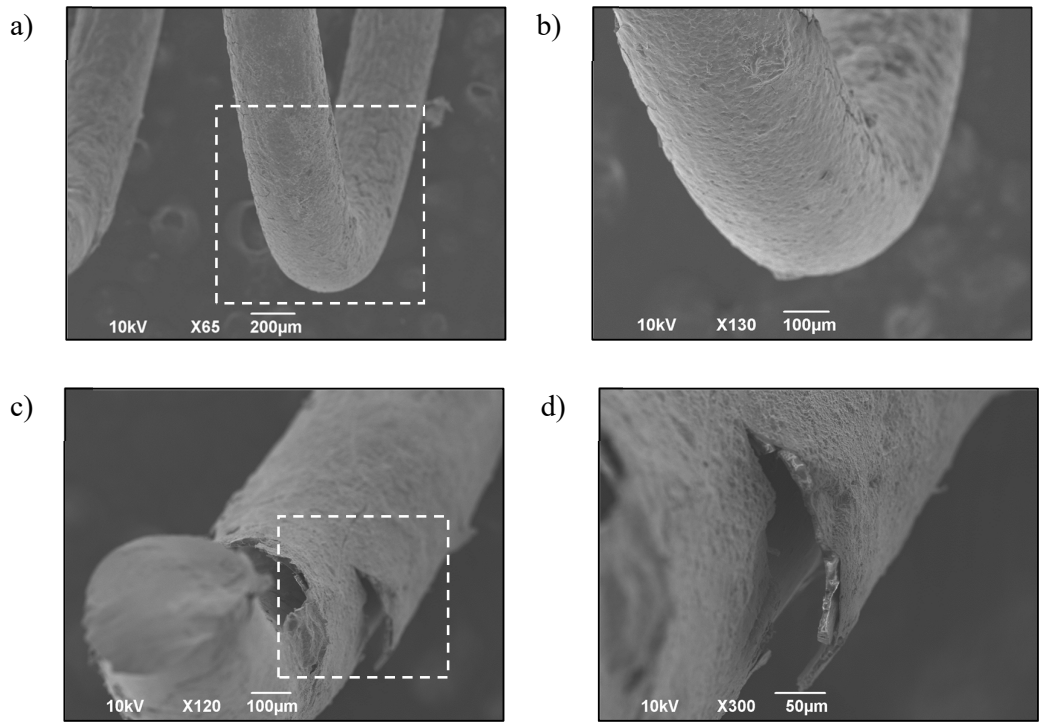

***Figure 2.14.** Morphological characterization of the ZR/cAlg bilayer coating on SS springs. SEM micrographs of ZR/cAlg coatings, with the surface (a, b) and cross-sectional (c, d) views of coated stainless-steel springs.*

In a parallel experiment, other natural polymers were tested as sacrificial layers, such as zein and hyaluronic acid, the latter with and without the addition of PEG. SEM cross-sectional pictures, shown in Figure 2.15, provide evidence of the development of bilayer films over previously deposited ZR-coated substrates using the dip-coating method. As expected, with the addition of a second layer of zein (Figure 2.15a), the two films were no longer distinguishable since the solvent of the zein solution (80% EtOH) dissolved the underlying coatings to form a single, thick rutin-loaded zein.

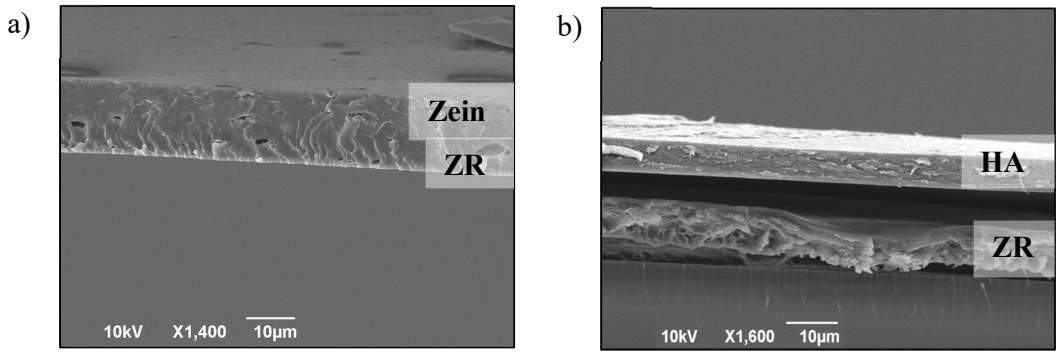

Figure 2.15. *Morphological characterization of bilayers made with different sacrificial layers. Cross-sectional view SEM images of bilayer coatings made with zein (a) and hyaluronic acid (b) as polymers for the top layer.*

The thickness of the scratched ZR/cAlg coating was evaluated using a stylus profilometer, and measurements of 15.4 ± 0.7 µm were obtained, as shown in Figure 2.16. This result is consistent with the mean value of 14.9 µm that was determined using an image analysis software from SEM cross-sectional micrographs (Figures 2.13(b) and 2.14(d)). Surprisingly, even when the cross-linked alginate layer was evenly applied to the samples, the surface roughness of the ZR/cAlg coatings increased (749.9 ± 42.6 nm) if compared to ZR/Alg (559.4 ± 18.1 nm) and ZR (219.2 ± 6.8 nm) coatings. Most likely, the presence of Ca^{2+} in the "egg-box" structure created by the interactions between alginate and calcium ions is the leading factor for these results. As reported in the literature, when cross-linking occurs, roughness and tiny imperfections on the surface of alginate films tend to appear [177].

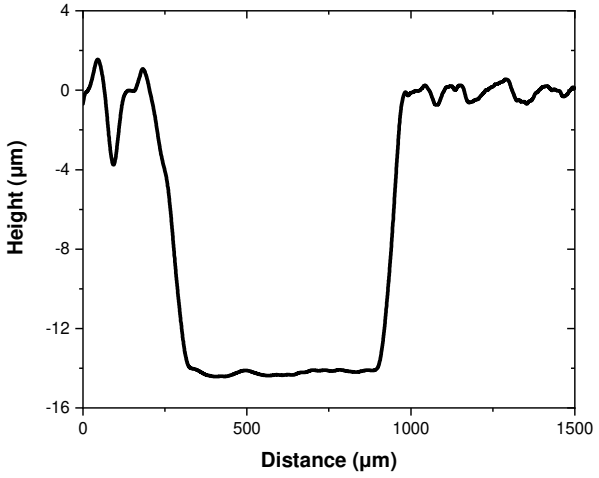

***Figure 2.16**. Thickness and roughness measurements of a previously scratched ZR/cAlg-coated sample. The analysis was performed with the surface profilometer.*

2.3.8 Water contact angle measurements

Experimental data on the degree of hydrophilicity/hydrophobicity of the coated SS surfaces were collected using the sessile drop technique (Figure 2.17). According to the literature, zein has almost equal amounts of hydrophobic and hydrophilic amino acids, which promote zein aggregation and self-assembly into films, as previously described in Chapter 1, Paragraph 1.2.2.1. With no active component inside the polymer, water contact angle measurements yielded a value of 61.03 ± 1.6° for the zein-coated coupons, while rutin-loaded zein coatings were more hydrophilic (38.7 ± 2.1°). This is owing to the hydrophilic drug being exposed to the coating surface, as already confirmed by XPS data (Table 2.3), causing a decrease in the water contact angle. Following the application of the alginate layer and calcium chloride on the ZR-coated coupons, the water contact angle decreased from 38.7 ± 2.1° to 25.9 ± 3.7°. In line with the findings from the literature, the surface turned out to be highly hydrophilic, and such property will improve the biocompatibility of the metal substrates by reducing the quantity of adsorbed platelets and proteins [163].

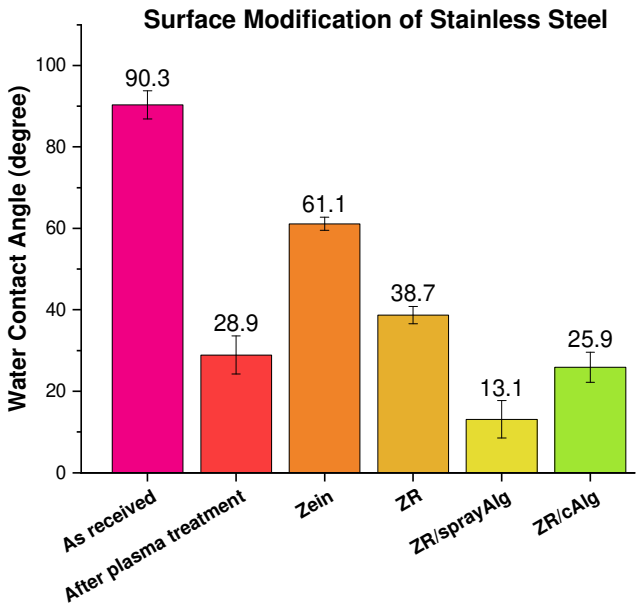

Figure 2.17. *Water contact angle measurements of the control and the coated SS samples.*

2.3.9 Bilayer coatings characterization: Fourier-transform infrared spectroscopy

The chemical composition and potential interactions between the ZR and cross-linked alginate layers were investigated using ATR-FTIR spectroscopy. Figure 2.18 shows the spectrum of cross-linked alginate, which shows four prominent bands at 3227, 1589, 1406, and 1022 cm^{-1}, which may be attributed to O-H vibrations, asymmetric and symmetric C-O-O vibrations, and C-O-C vibrations of glycosidic bonds, respectively. The zein amide I band at 1641 cm^{-1} appears to overlap in the ZR/cAlg spectrum with the characteristic alginate band at 1589 cm^{-1} and is presently detected at 1636 cm^{-1} as a single asymmetric band. Small peaks moving to lower wavenumbers may be caused by ionic interactions, such as those between alginate carboxylate groups and calcium ions or protonated zein amino groups. The band corresponding to the vibrations of the amide II groups occurs at 1518 cm^{-1} in the bilayer spectrum, demonstrating the presence of protein-polysaccharide interactions. A new band at 1732 cm^{-1} is observed, corresponding to the asymmetric stretching of C=O bonds in some protonated carboxylic acid groups of alginate, which appears after washing the ZR/cAlg samples with deionized water to remove the unbounded ions [170, 176, 177]. The IR absorption bands related to the samples under investigation are listed in Table 2.5.

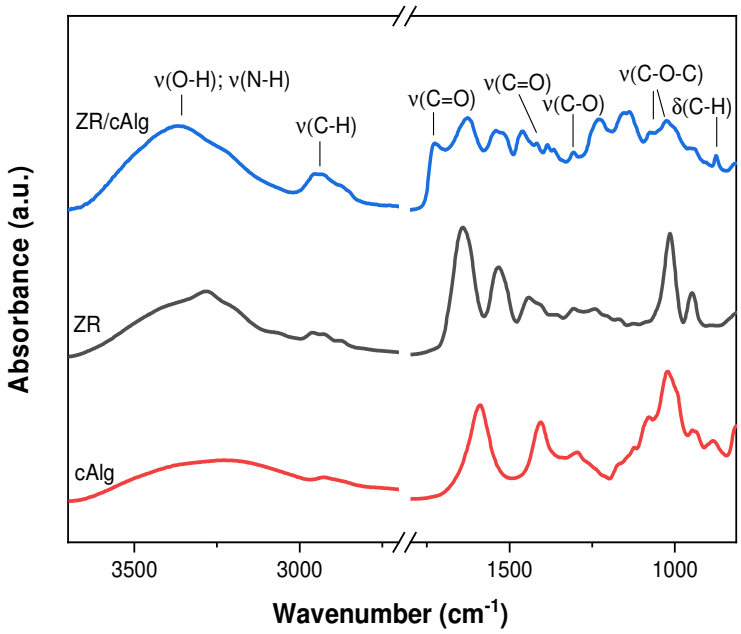

Figure 2.18. *FTIR spectra of cross-linked alginate, ZR, and ZR/cAlg films.*

Table 2.5. *Characteristic FTIR absorption bands assigned to vibrational modes of cross-linked alginate, ZR, and ZR/cAlg functional groups.*

FT-IR peaks (cm^{-1})			Vibrational mode
cAlg	ZR	ZR/cAlg	
3227	3283	3373	Amide A (ν(O-H), ν(N-H))
2924	2961-2882	2955	ν(C-H)
1589	1641	1636	ν_{as}(C-O-O), Amide I (ν(C=O))
-	1533	1518	Amide II (ν(C-N), δ(N-H))
-	1443	1449	δ(C-H), ν(C=C aromatic ring)
1406	-	1389	ν_{s}(C-O-O)
-	1360	1366	δ(C-OH)
1296	1306-1242	1310-1240	Amide III (δ(N-H), ν(C-N)), ν(C-O)
-	1171	1171	ν(C-N)
1123	1124	1130	ν(C-OH), ν(C-O-C)
1078	-	1065	ν(C-O) pyranose ring
1022	1015	1013	ν(C-O-C), ν(C-C)
947	947	951	ν(C-O)
885	-	891-839	δ(C-H) mannuronic residues

2.3.10 Bilayer coatings characterization: X-ray photoelectron spectroscopy

XPS analysis was used to describe the chemical composition of the bilayer samples at a depth of 10 nm below their surfaces. The results are shown in Table 2.6.

Table 2.6. *Atomic percentages of the elements obtained via XPS analysis of ZR/Alg and ZR/cAlg coatings.*

	Atomic Percentage (%)					
	C 1s	O 1s	N 1s	Na 1s	Ca 2p	Cl 2p
ZR/Alg	71.4	23.8	2.8	1.4	0.6	-
ZR/cAlg	53.4	16.3	2.5	-	9.5	18.3

Considering the use of sodium alginate in the fabrication of the sacrificial layer, the main elements found on the surface of the ZR/Alg samples were carbon and oxygen, with a percentage of 71.4 and 23.8%, respectively, with a small amount of sodium (Na) and calcium (Ca) ions (1.4% and 0.6%). The high amount of calcium in the ZR/cAlg samples demonstrates that the cross-linking procedure was successful. Moreover, the ratio between calcium and chlorine is around 1:2 (Ca^{2+}: $2Cl^-$), which is consistent with the $CaCl_2$ chemical formula.

2.3.11 Bilayer coatings characterization: mechanical analysis

A scratch test was used to quantify the adhesion stability of the ZR/cAlg bilayer coating on stainless-steel substrates. The critical load was calculated using the scratch profile of the load-displacement graph, as shown in Figure 2.19a, and confirmed using the matching optical picture of the scratch track, as shown in Figure 2.19b. The average critical load value was 768.3 mN, indicating strong adhesion between the ZR/cAlg coating and the SS substrate, which is required for the construction of a successful DES.

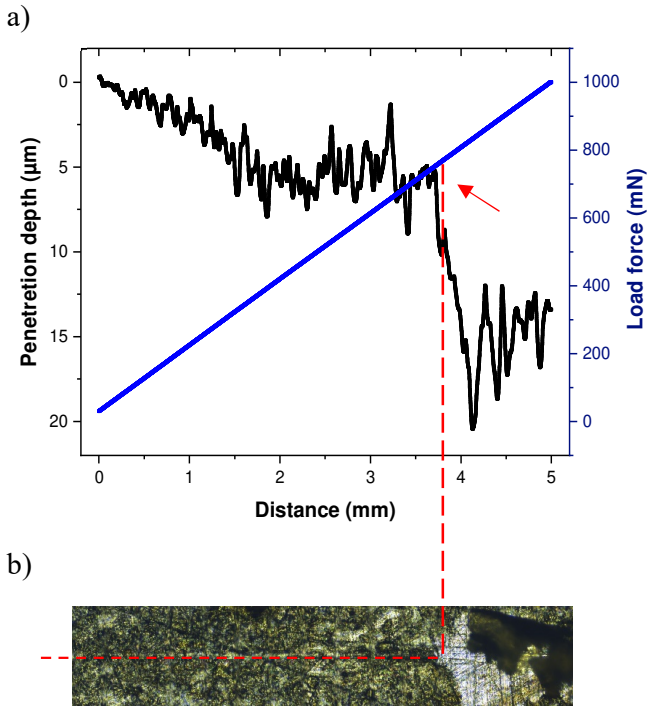

Figure 2.19. *The load-displacement curve and the corresponding optical image of a ZR-cAlg coated specimen. A red dotted line was drawn in order to compare the curve with the optical image of the scratch paths and to determine the exact critical load value for each sample. The arrow indicates the drop in the penetration depth signal, which corresponds to the critical load at the onset of coating cracking.*

2.3.12 Release profiles from the bilayer coatings

Figure 2.20 reports the cumulative release percentages of rutin from single-layer ZR, bilayer ZR/sprayAlg, and ZR/cAlg coatings on SS coupons during a 21-day period. The drug release rate from zein films was finely regulated and sustained by placing the sacrificial layer on top and hardening the upper alginate matrix with an appropriate quantity of $CaCl_2$. Both samples coated with alginate and cross-linked in one or two stages showed a slower rutin release profile. Furthermore, the drug elution from these bilayer samples exhibits a reduced initial burst release: the ZR/cAlg and ZR/sprayAlg samples showed 66.1 ± 3.2% and 73.1 ± 2.0% of rutin released, respectively, after 24 hours of incubation in warmed PBS. Both values are indeed lower than those obtained from the ZR samples (90.6 ± 3.2%, Figure 2.9). In conclusion, the second cross-linking procedure not only helped to uniformly cover the ZR underlying film with a fully cross-linked alginate layer but also to fine-tune the rutin burst release.

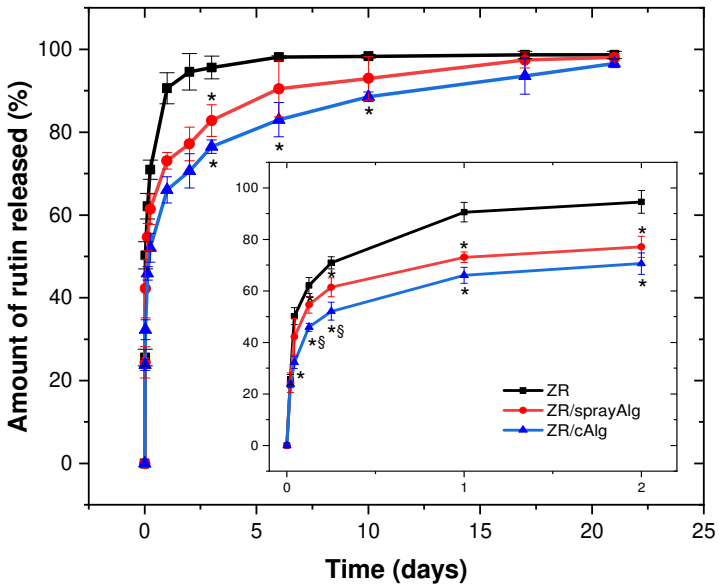

Figure 2.20. *Rutin release behaviors from single and bilayer coatings presenting alginate as the sacrificial layer. The cumulative release profile of rutin from ZR (black line), ZR/sprayAlg (red line), and ZR/cAlg (blue line) coatings, with an inset highlighting the release kinetics between 0 and 2 days. A significance of $p < 0.05$ (* for ZR/sprayAlg or ZR/cAlg and ZR and § for ZR/sprayAlg and ZR/cAlg) was considered.*

In the preliminary phase of this study, other commonly used naturally-derived biomaterials, including zein and hyaluronic acid, were evaluated as polymers for the construction of the top sacrificial layer. The bilayer drug release kinetics were determined at regular intervals for a period of 10 days. Among all, zein as the sacrificial layer allowed a more controlled release of the drug, even if, as seen in Figure 2.21, the bilayer structure was completely lost. Compared to hyaluronic acid, adding cross-linked alginate as a sacrificial layer allowed a slower drug release rate from the underneath ZR layer coating, and incorporating PEG in the HA solution did not help the retention of the drug. On the contrary, as already suggested by the literature, the presence of PEG increased both the ability to absorb water and the rate of hydrolytic degradation of hyaluronic acid matrices [178]. Ultimately, cross-linked alginate was chosen among the investigated materials due to its hydrophilicity, firm adherence to the protein film underneath, tunable drug release, and degradability by crosslinking procedures.

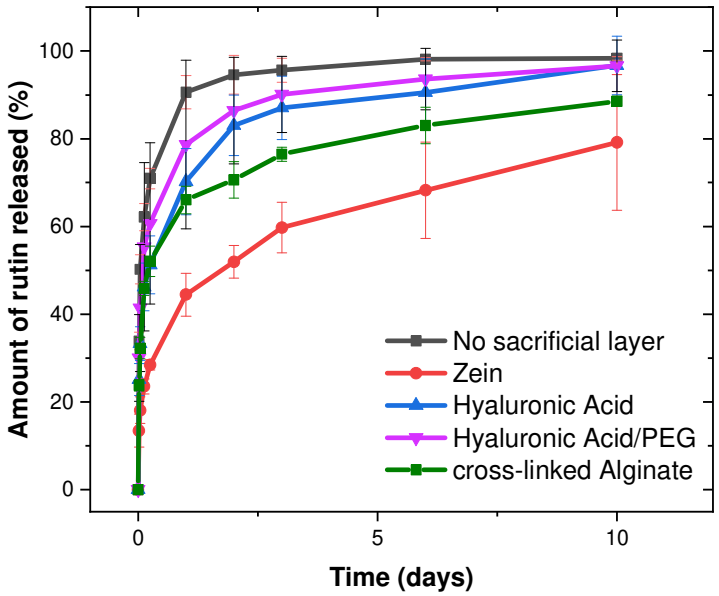

Figure 2.21. *The cumulative release profiles of rutin from different bilayer coatings.*

Regarding drug release kinetics, the developed ZR/cAlg coating seems advantageous compared to other bilayers made with degradable synthetic coatings, even if few data are available to date in the literature. Huang *et al.*, for example, employed PLGA to manufacture both the inner and outer layers of a DES coating and found a burst release of triflusal (a hydrophilic drug) of 60% on the first day, reaching almost 100% of release by day 5 [179]. Thakkar and colleagues reported sirolimus release over 48 days from a complex blend of PLLA, PLGA, and PVP, with an extra PVP top layer, with nearly all of the drug lost within five days [180]. The ZR/cAlg bilayer exhibits a more gradual drug-release rate also when compared with other naturally-derived bilayer coatings. Chen *et al.*, for example, created multi-layers of cross-linked collagen and found that 90% of sirolimus was released within four days [181].

2.3.13 Morphological changes during degradation assays

Surface morphologies of the degraded ZR/cAlg-coated samples at different time points were captured by SEM and are reported in Figure 2.22. Since the alginate matrix is a hydrophilic material, even when cross-linked both bulk and surface erosion tend to occur quickly. During the first 24 hours, little portions of the cross-linked alginate layer begin to dissolve from the coating, and at the same time, the appearance of tiny holes confirms that the underlying ZR layer is starting to degrade. Nevertheless, the presence of the sacrificial layer delays the formation of these pores, compared to what was observed for zein and ZR single layers in Figure 2.10.

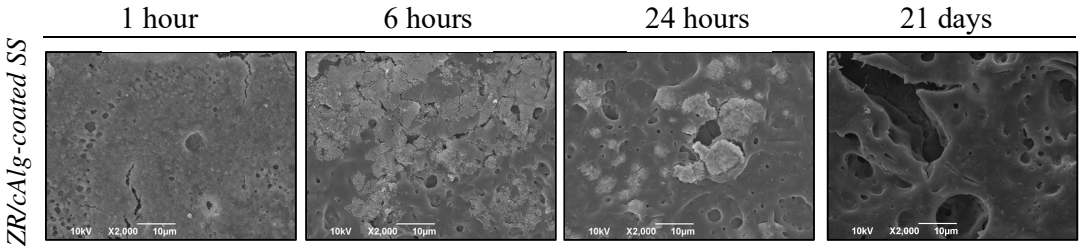

Figure 2.22. *SEM images of ZR/cAlg coatings after different incubation times.*

2.3.14 Antioxidant assays

As described in paragraphs 2.3.5 and 2.3.13, rutin as a strong antioxidant agent was found in high concentrations in the aqueous extracts from ZR and ZR/cAlg coatings. Figures 2.23a and 2.23b illustrate the measured free radical scavenging activities (RSA) of the extraction media from the analyzed coatings at specified time points for up to 144 hours against $DPPH^{\bullet}$ (a) and $ABTS^{\bullet+}$ (b) radicals.

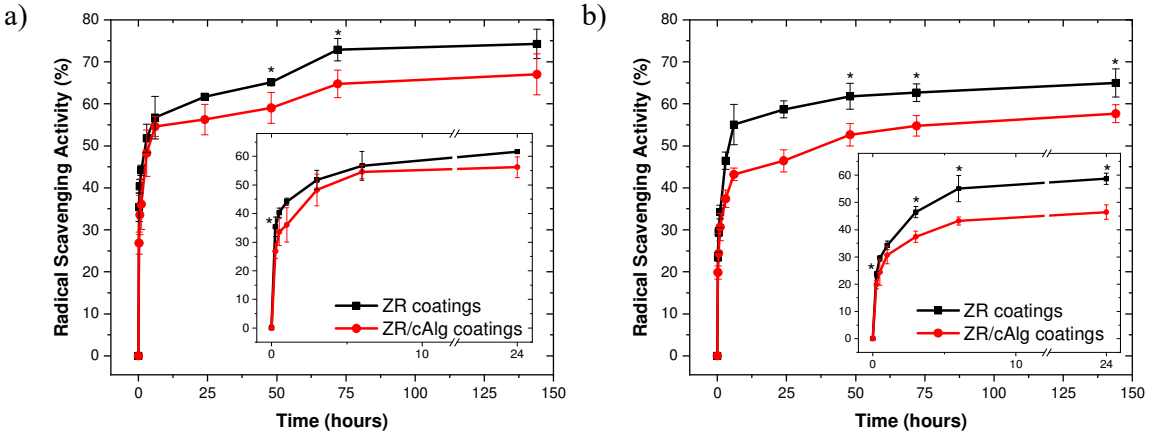

Figure 2.23*. Antioxidant activity of rutin in extraction media. Radical scavenging activity (RSA) was calculated against* $DPPH^{\bullet}$ *(a) and* $ABTS^{\bullet+}$ *(b) free radicals using PBS extracts from ZR coatings (black lines) and ZR/cAlg coatings (red lines). Insets highlight the RSA between 0 and 24 hours. A significance of* $p < 0.05$ *(*) was considered.*

Rutin extracts, obtained at different time points, were more efficient in scavenging DPPH$^{\bullet}$ than ABTS$^{\bullet+}$ radicals. After 144 hours, the RSA values against DPPH$^{\bullet}$ and ABTS$^{\bullet+}$ free radicals were 74.3 ± 3.5% and 65.0 ± 3.3% for ZR extracts, and 67.0 ± 4.9% and 57.7 ± 2.1% for ZR/cAlg extracts. The chemical characteristics and complexity of the released materials might result in varied bioactivity findings depending on the technique used, which could explain the variations between the two tests. Both assays are based on the hydrogen-donating ability of the radicals and involve the reduction of a colored molecule; however, the DPPH$^{\bullet}$ assay is conventionally conducted in ethanol or methanol, while the ABTS$^{\bullet+}$ assay is carried out in aqueous media. Factors such as radical stereo-selectivity and flavonoid solubility have also been observed to influence the capacity of antioxidant compounds to quench various radicals in different testing methods [182]. For comparison purposes, Figures 2.24a and 2.24f illustrate the scavenging activity of pure rutin powder dissolved in PBS against DPPH$^{\bullet}$ and ABTS$^{\bullet+}$ free radicals as a function of rutin concentration, and comparable patterns can be seen.

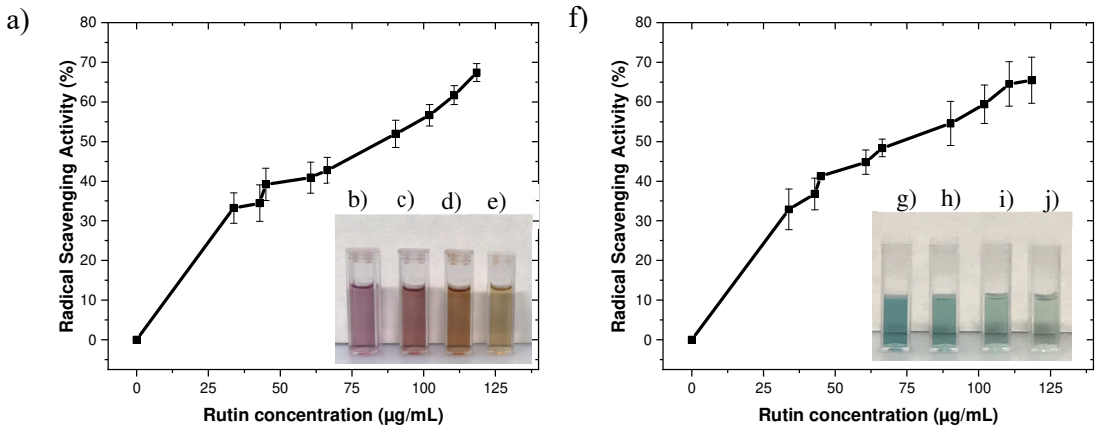

Figure 2.24. *Antioxidant activity of rutin in PBS. The graphs (a, f) were obtained with rutin-containing solutions at different concentrations (from 33.8 to 118.5 µg/mL). The insets in (a) and (f) show the color change of the DDPH and ABTS scavenging solutions at room temperature in the presence of 0 µg/mL (b, g), 33.8 µg/mL (c, h), 45 µg/mL (d, i) and 118.5 µg/mL (e, j) of rutin.*

It is clear that both RSAs increase with increasing rutin content, as predicted, following a pattern called "dose-dependent antioxidant activity". These data confirmed that rutin maintains its biological activity both during the manufacturing process and the following release test in aqueous media for an extended period of time.

2.3.15 *In vitro* studies with human umbilical vein endothelial cells

As mentioned in Chapter 1, endothelial cells and fibroblasts are both involved in the healing process and the maintenance of the homeostasis of the cardiovascular system physiology. Based on the potential application of our coatings in drug-eluting stent production, it is essential to demonstrate their compatibility on both cell lines. As reported in Figure 2.25, the plant-based coatings showed good biocompatibility on HUVEC compared to the standard control. Cells grew up to 86.2% and 100.5% after 24 and 48 hours on ZR-coated substrates, respectively, and up to 113.4% and 92.7% after 24 and 48 hours on ZR/cAlg-coated substrates, as compared to 100% growth on the control. Moreover, no statistical differences between the control and the cells grown on the ZR or ZR/cAlg layers were detected.

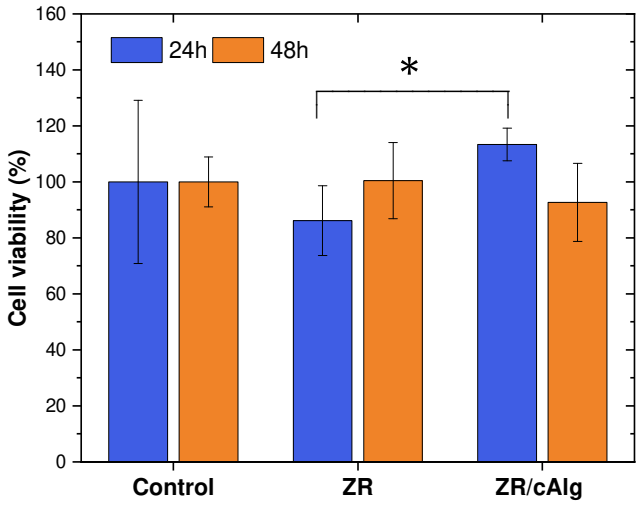

Figure 2.25. *Biocompatibility testing with HUVEC. HUVEC viability was evaluated via alamarBlue™ assay for cells grown onto ZR, ZR/cAlg coated glass coverslips and under standard conditions (control, uncoated glass coverslips) for 24 and 48 hours; data are presented as mean values ± SD. A significance of $p < 0.05$ (*) was considered.*

Figure 2.26 reports confocal microscopy images of HUVEC adherence on ZR and ZR/cAlg coatings after 48 hours of culture. Both samples exhibit a strong zein autofluorescence signal that can be seen in the blue channel, somewhat obscuring the cell nuclei staining. Both samples show strong cellular adherence, demonstrating that the coated substrates supported HUVEC attachment without hampering their proliferative ability. In particular, cells grown on ZR layers were more polygonal with

a cobblestone-shaped morphology, whereas cells grown on ZR/cAlg coated glasses grew elongated with a spindle-shaped morphology.

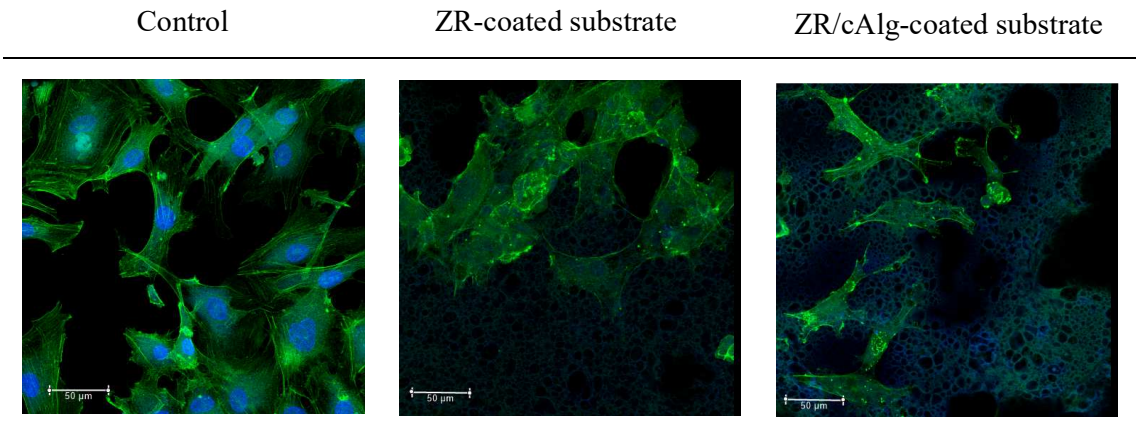

Figure 2.26. *Confocal images of HUVEC exposed to ZR and ZR/cAlg coatings. Cells were grown onto a control glass slide or glass coverslips coated with ZR and ZR/cAlg layers for 48 hours before the staining and imaging analysis (scale bar 50 µm). Nuclei are marked with Hoechst 33582 (blue) and cytoskeletons with Phalloidin FITC (green).*

The morphological response and variations of cells cultured on ZR and ZR/cAlg were partly induced by the surface alterations caused by the predictable coating degradation, resulting in an unstable growth surface. This finding is corroborated by PSB degradation investigations, detailed in paragraph 2.3.5 and shown in Figures 2.10 and 2.22. Taking into account both viability data and CLSM analysis, ZR and ZR/cAlg layers were shown to be excellent biocompatible materials with no discernible cytotoxic impact on HUVEC.

2.3.16 *In vitro* studies with human dermal fibroblasts

Regarding the MTS experiment on HDFa, cell viability values of 102.5% and 97.5% were recorded after 24 hours with ZR- and ZR/cAlg-based media, respectively; after 48 hours the cell viability was 103.8% and 103.6% with ZR and ZR/cAlg coatings extracts, respectively (Figure 2.27). No significant differences in the percentage of viability of the treated cells were observed compared to the control.

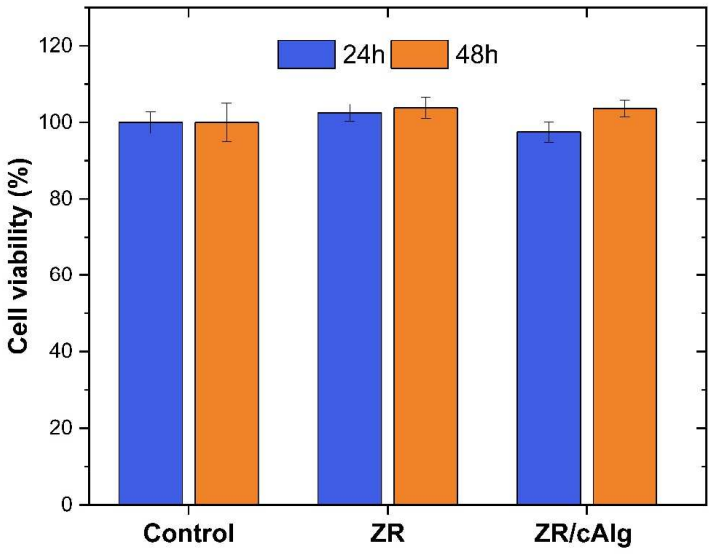

***Figure 2.27**. Biocompatibility testing with HDFa. HDFa viability was evaluated via MTS assay for samples treated with ZR and ZR/cAlg cell culture medium extracts and under standard conditions (control, normal growth medium) for 24 and 48 hours; data are presented as mean values ± SD.*

The morphology and cytoskeletal arrangements of HDFa cells treated with different coatings extracts were detected by fluorescence staining after 24 and 48 hours and are presented in Figure 2.28. After the treatments, the HDFa cells uniformly spread onto the glass substrates, indicating a healthy state.

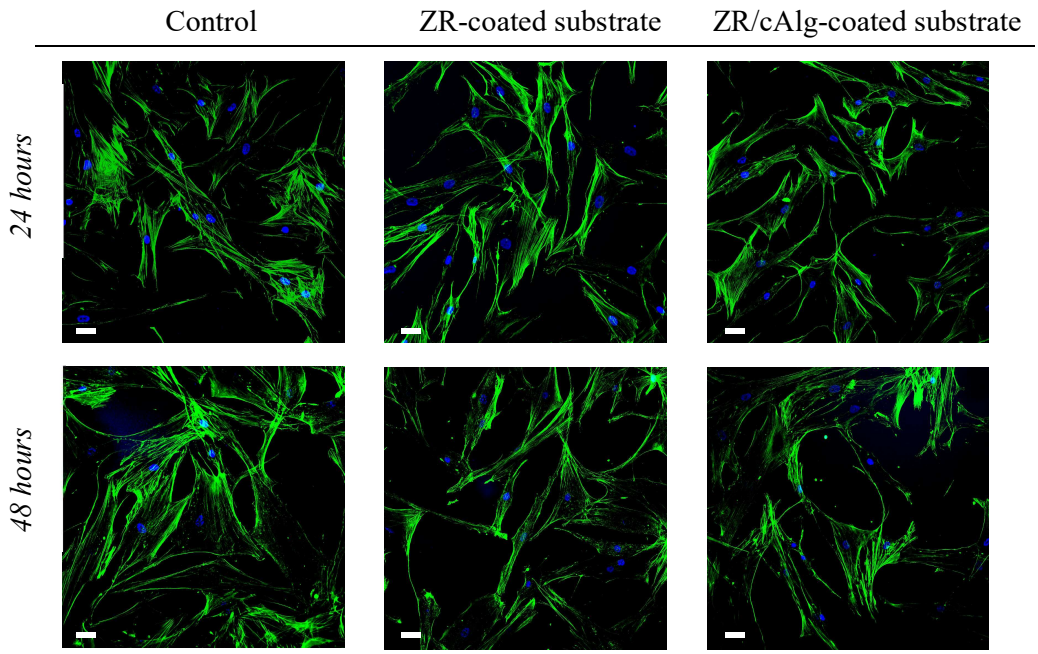

***Figure 2.28**. Confocal images of fibroblasts exposed to ZR and ZR/cAlg coatings extracts. Cell nuclei marked in blue (DAPI) and cell cytoskeletons highlighted in green (Alexa Fluor® 488 Phalloidin) after 24 and 48 hours of treatment (scale bar 100 μm).*

2.4 Conclusions

This chapter section is partially taken from Lenzuni M. et al., "Development of biodegradable zein-based bilayer coatings for drug-eluting stents" RSC Advances (2021).

In this first PhD project, a novel, biodegradable bilayer coating for drug-eluting stents was proposed. Zein, particularly in the form of thin films, was explored for its potential as a carrier matrix for drug delivery applications, owing to its slow biodegradability. The drug-eluting capabilities of our plant-based polymeric multifunctional coatings were evaluated by studying the release of rutin (i.e., the active component) from single-layer and bilayer systems. Cross-linked alginate showed to be the most promising sacrificial covering layer among the examined natural polymers due to its strong adherence to the underlying protein film and hydrophilicity. Moreover, when cross-linked, alginate succeeded in delaying the delivery profile of the entrapped antioxidant drug and ensured the biocompatibility of the coated metal substrate. Both zein and alginate are widely available natural polymers easily extracted from vegetable waste through green and sustainable approaches. ZR/cAlg layers were successfully fabricated and uniformly coated onto SS substrates by fast, green, cost-effective dip and spray coating methods. The applicability of these coatings for stents was determined, after looking at their physico-chemical characteristics, by assessing the adhesion and growth of endothelial cells and fibroblasts.

Studies on biocompatibility validated the safety of the developed bilayered plant-based coatings as interfacial biomaterials capable of forming a pro-healing stent surface that promotes the endothelialization of the device.

In conclusion, the developed plant-based bilayer meets the major parameters for an effective drug-eluting coating for DES, exhibiting strong physico-chemical qualities, drug antioxidant stability, excellent biocompatibility with vascular cells, and the capacity to precisely tune drug elution. These findings pave the way for developing a new generation of bio-based multi-layer DES and dual-drug eluting stents in the near future, with the goal of enhancing the cyto- and hemocompatibility of the coating materials while accurately adjusting their drug release kinetics.

Chapter 3 - Dynamic behavior and hemocompatibility of zein-based coatings for drug-eluting stents: a microfluidic investigation

3.1 Introduction

This chapter section is partially taken from Lenzuni M. et al., "Dynamic investigation of zein-based degradable and hemocompatible coatings for drug-eluting stents: a microfluidic approach" RSC Lab on a Chip (2023).

As previously mentioned in Chapter 1 and Chapter 2, drug-eluting stents (DES) have been shown to be extremely successful in avoiding restenosis following stenting operations, and, in the last decades, they are largely regarded as one of the most promising treatment alternatives [152]. The therapeutic effects of DES are directly dependent on their drug release kinetics, which are connected to the matrix characteristics and degradation rates, according to preclinical animal research and clinical trials [145]. As a result, estimating these parameters is crucial for the evaluation of newly developed DES coating materials. Under static settings, stents or stent replacements are typically immersed in small containers containing a buffer solution, which is regularly replenished with a fresh release medium [183]. The disadvantages of this standard approach are:

- it does not take into consideration the fluid dynamic environment of DES in the vascular system;
- the saturation of the buffer with the released molecules lowers the concentration gradient between the matrix components and the surrounding solution, giving inaccurate release and degradation results [183];
- the composition of the elution medium affects the delivery profiles as both drugs and polymers could be susceptible to changes in the chemical properties of the solution [184]. Many conventional release studies for poorly water-soluble drugs may not accurately reflect *in vivo* pharmacokinetics and may produce incorrect results due to the inclusion of solubilizers and surfactants, such as Tween 20 and Pluronic [185].

As widely discussed in Chapter 1, Paragraph 1.1.6, blood compatibility is another major parameter to evaluate when assessing DES coating performance. During the first clinical experiences, there was a significant rate up to 45% of acute stent thrombosis (within a few days of stent deployment) [31]. Even if aggressive antithrombotic regimes combining antiplatelet agents and heparin (or warfarin) were used, meaningful reductions in stent thrombosis were offset by a high incidence of bleeding [186]. The injury of the quiescent endothelium and the inert thrombogenicity of the stent surface are regarded as critical factors. Rapid adsorption of plasma proteins to the material surface occurs within minutes after contact with the blood, after which both extrinsic and intrinsic coagulation pathways can be activated (the intrinsic pathway by factors in the blood, while the extrinsic one by the tissue factor released from endothelial cells) [187]. For the successful development of implantable medical devices, surfaces with high antithrombotic properties, such as low platelet activation potential, are essential [188]. Similar to the release assays, the analysis of how stent coatings composition influences the behavior of blood components has been largely limited to static studies that are simple to use and quick. However, these studies do not account for the activation of platelets in flow conditions [189]. On the other hand, *in vivo* studies are expensive, time-consuming, and ethically questionable. Additionally, because of their complexity, they might not give thorough explanations of how the coated device interacts with the blood components.

Microfluidic technology has recently attracted much attention and ushered in a new era of cutting-edge research to simplify challenging *in vivo* conditions and gather information to supplement animal studies. Lab-on-a-chip platforms provide the desirable option for performing *in vitro* tests in a dynamic setting, simulating the physiological conditions more accurately than experiments in conventional static cell culture dishes. Valuable features include small sample volumes and adaptable flow conditions [128]. More information on this new technology can be found in Chapter 1, Paragraph 1.3. As anticipated, microfluidic chambers for biomedical applications have been so far primarily made of soft polymeric materials, particularly PDMS, which are not entirely inert (they may absorb small molecules such as hydrophobic drugs, causing results to be misleading), have poor mechanical resistance and durability (they tend to dry out or tear after a short period of time), and are difficult to reuse or recycle [190]. To overcome these limitations, advancements in microfabrication tools (e.g., femtosecond laser micromachining), in combination with novel inert substrate materials (e.g., fused silica), have provided the ability to obtain unique 3D microfluidic systems, which result particularly suitable for chemical and biological research applications.

In this second PhD project, the design, manufacture, and validation of innovative fused silica-based microfluidic systems were carried out to examine the hemocompatibility and dynamic behavior of drug-eluting materials for stent applications. As reported in Chapter 2, innovative zein-based DES coatings were fabricated using green solvent, biocompatible naturally-derived materials and active compounds. More precisely, rutin, a plant-derived flavonoid, was loaded as the antioxidant and anti-inflammatory component, while zein, a protein extracted from maize, was positively appraised as a

slow-degrading carrier matrix. Preliminary results demonstrated excellent biocompatibility and overall potential for rutin-loaded zein (ZR) material as DES coating. In order to further investigate such sustainable plant-based coating under dynamic flow conditions, novel microfluidic chips were developed, comprising channels with vessel-inspired geometries in terms of shape and dimensions. In particular, round and square cross-section channels were fabricated individually to simulate a stented blood vessel in three dimensions under healthy and obstructed situations, respectively. Each channel was fully coated with a rutin-loaded zein layer in order to investigate the effect of different fluids and geometries on both drug release and matrix degradation kinetics. Lastly, the developed microfluidic systems were employed to assess the *in vitro* hemocompatibility properties of the proposed zein-based materials, with both the coatings and the blood cells exposed to physiologically-relevant conditions.

3.2 Materials & Methods

This chapter section is partially taken from Lenzuni M. et al., "Dynamic investigation of zein-based degradable and hemocompatible coatings for drug-eluting stents: a microfluidic approach" RSC Lab on a Chip (2023).

3.2.1 Materials

Zein powder, rutin hydrate, urea, glycerol, sodium chloride, sodium bicarbonate, potassium chloride, sodium phosphate dibasic, magnesium chloride, calcium chloride, sodium sulphate, heparin sodium salt, Trizma® hydrochloride, hydrochloric acid, and 5-µm-diameter polystyrene (PS) beads were provided by Sigma-Aldrich (St. Louis, USA) and used as received without further purification. Waterborne polyurethane, grade ICO-THANE 10, was provided by I-Coats NV (Berchem, Belgium). Poly(lactic acid) 6060D was purchased from Nature Works LLC (Minnetonka, USA). UV photocurable optical adhesive NOA63 was purchased from Norland Products (Cranbury, USA). Commercial stainless steel flat sheets (316L SS, 500 mm x 300 mm x 0.5 mm) were purchased from RS Component (Milan, Italy). Dulbecco's Phosphate Buffered Saline (PBS), dimethyl sulfoxide (DMSO), dichloromethane (DCM), ethyl acetate, and ethanol (≥ 99.8%) were purchased from Sigma-Aldrich (St. Louis, USA), while deionized water (ddH_2O) was supplied by a Milli-Q Integral purification system (Millipore, Bedford, USA).

3.2.2 Design and production of microfluidic devices

Femtosecond laser-assisted micromachining in conjunction with wet etching (known as FLICE, Femtosecond Laser Irradiation followed by Chemical Etching) was used to fabricate the microfluidic chips due to its capacity to quickly create 3D architectures without the need for masks or a clean room, as anticipated in Chapter 1, Paragraph 1.3.1. A square cross-section channel represents the scenario where atherosclerotic plaques significantly occlude a vessel, whereas a circular cross-section channel represents a partly occluded stented artery. The choice of a square geometry was supported by the evidence obtained from histological images available in the literature of atherosclerotic plaques and (partially) obstructed vessels [191, 192]. The peculiar manufacturing process is composed of two main steps. A fused silica substrate was initially exposed to an ultrashort-pulsed laser beam that follows the 3D-designed geometry. The physico-chemical characteristics of the material were only affected in the region limited to the beam spot volume. Wet etching, the next stage, included an ultrasonic bath and a chemical solution (20% aqueous hydrofluoric acid (HF)) to allow the material to be selectively removed to produce the desired 3D shape (Figure 3.1).

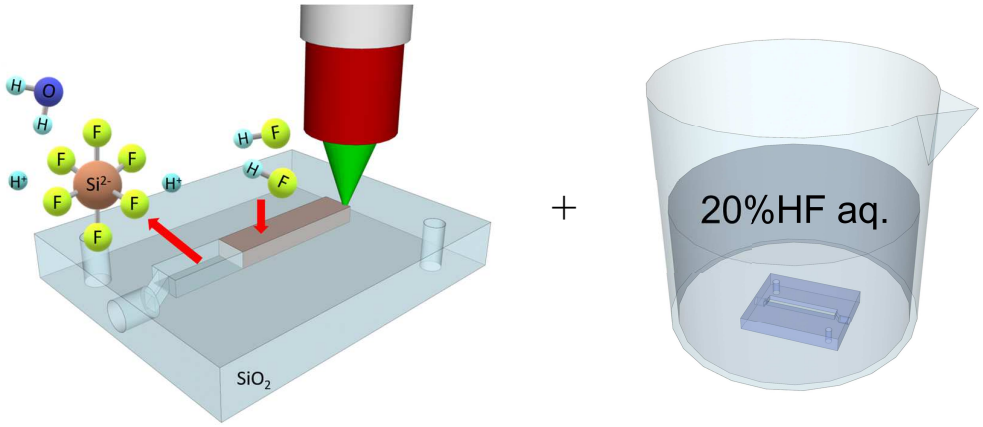

***Figure 3.1**. Illustration of the two steps of the FLICE fabrication method of fused silica-based microfluidic devices. Ultra-short pulse laser induces the nanogratings (or nanocracks) formation which are useful for the chemical etching process.*

For each geometry (round and square), two open chip portions were produced (Figure 3.2 a-d) instead of a single buried one. As a result, the two parts could be individually handled and evaluated before being stacked and aligned so that the same device may be used several times. The two chambers were sealed using a transparent optical glue. The dimensions of the constructed microfluidic chips were 9.8 mm (width) x 13.9 mm (length) x 2.8 mm (height). The geometry is supplemented by two access ports to integrate tubes (inlet and outlet) connecting the chips to the outside environment. The entire longitudinal distance between the inlet and outlet holes of the device was 10 mm (Figure 3.2e). The

round channel had a gap in the center with a circular aperture (Ø = 1.8 mm), whereas the square channel had an opening of 1.8 x 1.8 mm^2 (Figure 3.2f).

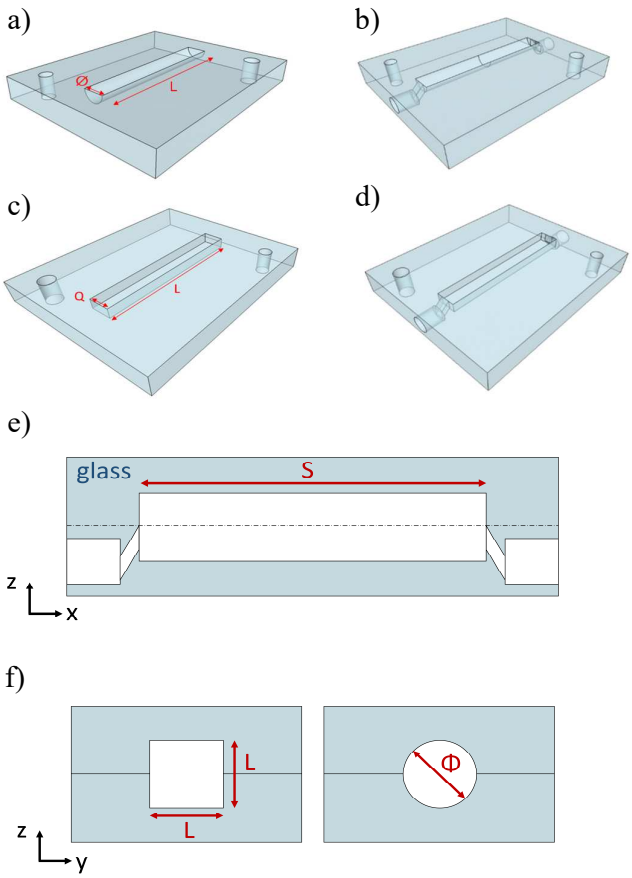

Figure 3.2. *Schematic representation of the microfluidic chips. 3D structures of round (a, b) and square (c, d) cross-section channels, and illustration of the chips along the z-x (e) and z-y (f) planes are schematically showed.*

3.2.3 Fabrication and characterization of zein-based coated-channels

The rutin-loaded zein (ZR) solution was prepared as described in Chapter 2, Paragraph 2.2.2. By changing the spray time, ZR coatings with different thickness were obtained on the fused silica-based channels, as shown in Figure 3.3. Following this preliminary examination, the ZR solution was sprayed for 6 seconds at a distance of 30 cm over each pair of open sections (lower and upper sides) of the microfluidic channels using an airbrush spray coating equipment (0.55 mm nozzle diameter, model VL-SET, Paasche Airbrush Company, Chicago, USA) in order to achieve a comparable thickness with the first project (Chapter 2). The coated chambers were then left to dry at room temperature overnight. Subtracting the weight of the empty chip from the weight of the coated chip yielded the weight of the

sprayed coating. All weighings were performed with an analytical balance (ABT 120–5DM, Kern) with a level of accuracy of 0.01 mg. The quantity of zein and/or rutin deposited on each chip was calculated by comparing this result to the weight of 1 mL of dried ZR solution.

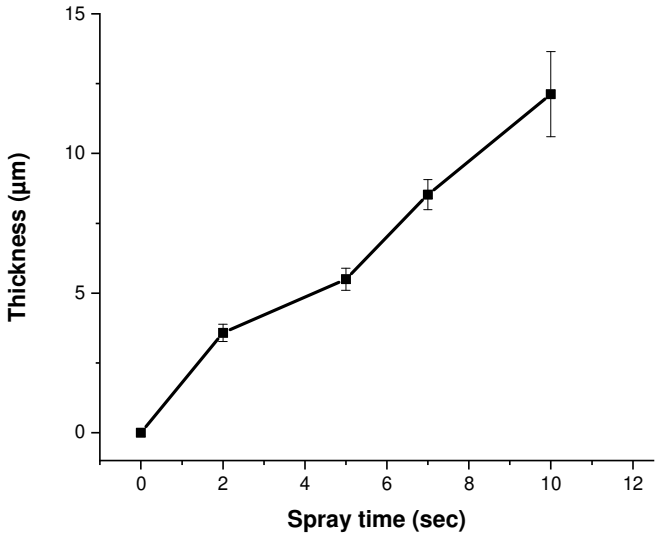

***Figure 3.3**. Thickness of ZR layers measured at different times of spray.*

SEM was used to examine the surface morphologies and thicknesses of the polymer coatings using a SEM JSM-6490LA microscope (JEOL Inc., Peabody, USA) at 10 kV accelerating voltage. A lancet was used to scratch the coated channels, and the results of thickness values were validated using a surface profilometer (Ambios XP-2, Ambiostech, Santa Cruz, USA) equipped with a diamond-tipped stylus (radius = 2 µm), which acted across the surfaces under a constant load of 0.5 mN with a speed of 0.5 mm/s. The average roughness was determined using similar parameters. To investigate the surface wettability, the ZR solution was sprayed over the flat portion of the chips using the same operational conditions, and water contact angle measurements were taken using a contact angle goniometer (Dataphysics OCA 20, Filderstadt, Germany). In brief, 5 µL droplets of ddH_2O were deposited on ten distinct spots with a microsyringe using a sessile drop technique, and the obtained pictures were elaborated using the SCA20 Software (Data Physics Instruments GmbH, Filderstadt, Germany). The angle between the drop's baseline and the tangent at the drop boundary was calculated, and the contact angle measurements were computed by taking the arithmetic average of the left and right contact angles from each droplet.

3.2.4 Simulated blood fluids (SBFs)

As previously anticipated, the selection of appropriate release media is critical when studying the behavior of biomedical coating materials. Two types of simulated blood solutions were produced for this study:

- In order to fabricate a fluid that could match the dynamic viscosity of human blood ($\mu \sim 4$ mPa*s), solutions with various mixing ratios of water, glycerol, and urea (SBF_wgu) were produced, following previous protocols [193]. The rheological parameters of these mixtures, stirred at room temperature for 12 hours, were measured using a Haakee Mars 40 Rheometer (Thermo-Scientific, Karlsruhe, Germany) equipped with a conical probe C60 1°/Ti. While maintaining a constant temperature of 25 °C, a shear rate sweep (shear rate ≈ 0.1 - 1000 s^{-1}) was used to determine the dynamic viscosity values.
- SBF_ws indicates an aqueous mixture to which various salts were added to fabricate a fluid whose ion concentrations were nearly equal to those of the human blood plasma (Table 3.1). SBF_ws was prepared according to the protocol described in the literature [194]. The reagents were dissolved one at a time in deionized water using a magnetic stir bar at 37 °C. The pH of the resultant solution was adjusted to 7.4 using a digital pH meter (HANNA HI2002, Hanna Instruments, Rhode Island, USA).

Table 3.1. *Comparison between ion concentrations of SBF_ws and human blood plasma.*

Ion	Na^+	K^+	Mg^{2+}	Ca^{2+}	HPO_4^{2-}	HCO_3^-	Cl^-	SO_4^{2-}	Buffer agent
Human Blood Plasma (mM)	142	5	1.5	2.5	1	27	103	0.5	-
SBF_ws (mM)	142	5	1.5	2.5	1	27	125	0.5	Tris

3.2.5 Microfluidic platform assembly

Once the ZR coating was dried, the top and bottom chambers were meticulously aligned, and UV-curable optical adhesive NOA63 was placed along the borders of the chambers before sealing each portion to provide a leak-free connection between the two coated chambers of each microfluidic chip. The sealed microfluidic chips were glued to a standard glass microscope slide (1 x 26 x 76 mm) using a small quantity of adhesive to boost the stability of the whole system. Perfluoroalkoxy (PFA) tubes measuring 1/16" OD x 0.02" ID were used to connect the microfluidic platforms, with the inlet and

outlet ports of each chip sealed using the NOA63 glue. A UVGL 58 lamp (UVP, Upland, USA) emitting at 365 nm was employed to polymerize the bonding agent. A LiveFlow peristaltic pump (IVTech, Massarosa, Italy) connected to the inlet tube via Luer adapters perfused the devices with fresh medium being supplied from the SBF-filled reservoir to the pump tubes. All studies were carried out at 37 °C with a constant flow rate of 500 μL/min to imitate the *in vivo* conditions of a cardiovascular stented artery. The physiological temperature was maintained by heating the SBF-filled reservoir on a hot plate. After passing through the microfluidic channel, the eluted medium was dropped into collection tubes and stored prior to analysis.

3.2.6 Three-Dimensional computational fluid dynamics

Fluid dynamics investigations based on computational models created in COMSOL Multiphysics 5.3 (Burlington, USA) were undertaken to study the flow environment of the microfluidic channels in the constructed devices. The fluid properties and boundary conditions of the numerical model were defined to mirror the experimental setting. A dynamic mesh volume length was employed to reach a compromise between computational cost and spatial resolution accuracy: less densely packed in the secondary parts (e.g., pipes, inlets) and denser in the core area of highest importance. The complete fluid dynamic field was obtained by solving the Navier-Stokes and laminar flow equations. Considering that the two proposed SBFs show similar densities values (1.03 g/cm^3 for SBF_ws and 1.15 g/cm^3 for SBF_wgu), the longitudinal and transversal velocity distributions were determined by imposing the SBF_wgu flow inside the channels.

3.2.7 Matrix degradation studies

In order to study the degradation rate of the zein-based polymeric coatings applied onto the microfluidic channels, each SBF was perfused into the round and square devices as the elution medium. The media were withdrawn for analysis at predetermined time intervals (ranging from 15 minutes to 6 hours), and fresh SBF was continuously replenished into the heated reservoir. Absorbance at 270 nm (zein λ_{max}) was determined for each sample with a Cary 6000i UV-Vis-NIR spectrophotometer (Varian, Palo Alto, USA). The amount of zein released at each time point was calculated by an appropriate calibration curve, and the results were expressed as the percent of cumulative zein degraded over time, according to Equation (1) already described in Chapter 2, Paragraph 2.2.9.

To assess the presence of morphological changes on the surface of the coatings during the dynamic flow experiments, at specific time points the microfluidic chips were quickly rinsed with deionized water to remove any residual salts crystal deposits, were opened by removing the NOA63 adhesive with a gentle swabbing of DCM and allowed to air-dry. SEM detected morphological

characteristics of the degraded coatings (surface and cross-section) as previously described. Differences in the degradation kinetics and morphology between microfluidic chips of different cross-section geometry resulting from the flow of different fluids were studied and compared.

3.2.8 Drug release kinetics and mathematical models

The samples collected as described in the previous paragraph were tested to determine the concentration of the active compound (rutin) released in the elution medium at each time point. The absorbance at 362 nm (rutin λ_{max}) was measured, and the data were represented as the cumulative percent of rutin released over time using an appropriate calibration curve and Equation (2), as indicated in Chapter 2, Paragraph 2.2.9. The effects of the channel geometry and the elution medium on drug release profiles were investigated and compared. Furthermore, the resulting drug release kinetics were studied using mathematical models. In particular, several commonly used power-law equations were employed to fit rutin release data and helped to explain the underlying transport mechanisms. The highest value of the correlation coefficient (r^2) was used as the criterion for selecting the best model for data fitting. Between the main drug release kinetic models, zero-order, first-order, Higuchi, Hixson-Crowell, and Korsmeyer-Peppas models were applied and compared:

- zero-order model: $\boldsymbol{Q_t = K \cdot t}$, where Q_t is the amount of rutin released at the time *t*, and K is the zero-order release constant.
- first-order model: $\boldsymbol{ln\ (1-Q_t) = -K \cdot t}$, where Q_t is the amount of rutin released at the time *t* and K is the first-order release constant.
- Higuchi model: $\boldsymbol{Q_t = K \cdot t^{1/2}}$, where Q_t is the amount of rutin released at the time *t*, and K is the Higuchi dissolution constant.
- Hixson-Crowell model: $\boldsymbol{1-(1-Q_t)^{1/3} = -K \cdot t}$, where Q_t is the amount of rutin released at the time *t*, and K is the Hixson-Crowell constant.
- Korsmeyer-Peppas model: $\boldsymbol{Q_t = K \cdot t^n}$, where Q_t is the amount of rutin released at the time *t*, K is the release rate constant, and n is the release exponent [195].

3.2.9 Polystyrene beads-loaded SBFs

Polystyrene (PS) beads with a diameter of 5 µm were used as a simple cell model, as previously described in the literature, to perform initial proof-of-concept experiments [196]. The PS beads were added to the previously prepared SBFs at a final concentration of 5 x 10^6 beads/mL to simulate the behavior of red blood cells (RBCs). Using a Zetasizer Nanoseries (Malvern Instruments, Worcestershire, United Kingdom), zeta potential recordings of diluted PS beads were obtained using dynamic light scattering (DLS). Freshly produced SBFs filled with PS beads were examined with an optical microscope (Axio

Scope 2, Zeiss, Oberkochen, Germany) to ensure a good dispersion of the particles, which were subsequently flown through the microfluidic devices for 30 minutes under identical conditions outlined in paragraph 3.2.5. After the dynamic experiments, the chips were opened by removing the NOA63 glue, a 15 nm gold layer was sputter coated on top, and SEM examination was immediately carried out to look into any potential bead adherence and the resulting ZR coatings morphology.

3.2.10 Hemocompatibility tests

Hemocompatibility tests were performed to determine the blood compatibility of the proposed zein-based coatings for stent application. As reported in Chapter 1, Paragraph 1.1.6, platelet attachment is the most critical phase during blood coagulation and thrombus formation on artificial surfaces. Since the presence of RBCs is known to have a significant influence on platelet adhesion, whole blood adhesion experiments involving all blood cell components were performed [197]. Specifically, 12 male C57BL/6 mice (Charles River, Calco, Italy) were used to perform and compare static and dynamic studies of blood cell behavior onto several coated surfaces. All procedures were carried out in conformity with the European Communities Council's Ethical Guidelines (Directive 2010/63/EU of 22 September 2010) and were approved by the Italian Ministry of Health. According to the "3Rs philosophy," every attempt was made to reduce animal suffering and to utilize the lowest number of animals necessary to provide accurate findings. The mice were kept in groups in ventilated cages with free access to food and water in a 12-hour light/dark cycle (lights turned on at 8:00 a.m.) at a constant temperature (21 ± 1 °C) and relative humidity (55 ± 10%). Whole blood was taken from mice in vacutainer tubes containing heparin (5000 U/mL), as is standard practice for hemocompatibility tests [198]. Within 2 hours of collection, the blood was diluted with normal saline (4:5 v/v) and utilized for the experiments.

3.2.10.1 Blood cells adhesion and hemolysis assays

Several coating materials on 316L SS flat samples (1.8 x 1.8 cm^2 exposure area) were first tested and compared. In particular, reference materials such as polyurethane (PU, dissolved in water) and poly(lactic acid) (PLA, dissolved in ethyl acetate) were employed as coating polymers for comparison reasons, in addition to zein-based coatings. According to the scientific literature, a 200 µL drop of diluted whole blood was applied to each sample and incubated for 30 minutes at 37 °C for the static blood cells adhesion experiments [199, 200]. The samples were then quickly washed three times with PBS to remove non-specifically adsorbed cells, and the remaining adherent platelets and RBCs were promptly fixed for 90 minutes at room temperature with 2% v/v glutaraldehyde in 0.1 M sodium cacodylate buffer (pH 7.4, Sigma Aldrich). After removing the fixative solution, the samples were

washed three times for 10 minutes each with the same buffer and kept overnight at 4 °C. The samples were post-fixed in 0.1 M sodium cacodylate buffer containing 1% v/v osmium tetroxide (Sigma Aldrich) and subsequently dehydrated in a succession of ethanol solutions. Finally, they were incubated in a series of hexamethyldisilazane (Sigma Aldrich) / ethanol solutions, air-dried, sputter-coated with 15 nm gold to minimize charging effects, and examined with SEM. Using the ImageJ software, the number of adherent platelets per mm^2 was calculated from the captured micrographs as a measure of platelet density on the selected materials. Activated platelets, easily detected by the presence of pseudopodia, were manually distinguished.

According to the international standard ISO 10993-4, the hemolysis assay was performed for the same materials [201]. In brief, samples with an exposure area of 1.8 x 1.8 cm^2 were soaked in 2 mL of normal physiological saline and stored at 37 °C for 30 minutes. Following previously established protocols, 0.04 mL of diluted blood was added to the samples, which were then maintained at 37 °C for an additional 60 minutes, and ultimately, the solutions were removed and centrifuged for 10 minutes at 1100 g at room temperature [202, 203]. Normal physiological saline and distilled water served as negative and positive controls, respectively. Using a Spark Multimode microplate reader (Tecan Group Ltd., Männedorf, Switzerland), the absorbance of the supernatant (100 µL) was measured at 542 nm (characteristic wavelength of hemoglobin). The hemolysis rate (HR) was calculated according to Equation (4).

$$\text{HR}\,(\%) = \frac{\text{Sample absorbance} - \text{Negative control absorbance}}{\text{Positive control absorbance} - \text{Negative control absorbance}} \text{ x } 100 \qquad \text{Eq. (4)}$$

3.2.10.2 Dynamic experiments

The dynamic flow experiments with mice blood were performed using the peristaltic pump at a continuous flow rate of 500 µL/min. Before the assays, the assembled microfluidic chips were perfused with PBS and checked for the absence of air bubbles or fluid leakage. After drawing whole blood samples (about 1.5 mL each) via the tubing system, the flow was sustained for 10 minutes before the devices were washed with pre-warmed PBS to eliminate unbound platelets and RBCs within the coated channels. Following the meticulous disassembly of the microfluidic platform, the adhering cells on the coatings were quickly fixed, as indicated in the above paragraph. SEM was used to evaluate blood cell adhesion, platelet shape, aggregation, and pseudopodia development on randomly selected locations. Additionally, the obtained pictures were examined with an image analysis software to measure the coating area covered by platelets.

3.2.11 Statistical methods

Using Origin 2019b 64Bit software, all measurements were statistically evaluated (OriginLab Corporation, Northampton, USA). An unpaired Student's t-test was performed to discover statistically significant differences between two groups. When more than two groups were compared, a one-way ANOVA followed by post-hoc Tukey HSD tests was employed for comparisons. Statistical significance was defined as $p < 0.05$ (*) and $p < 0.01$ (**) probability values.

3.3 Results & Discussion

This chapter section is partially taken from Lenzuni M. et al., "Dynamic investigation of zein-based degradable and hemocompatible coatings for drug-eluting stents: a microfluidic approach" RSC Lab on a Chip (2023).

3.3.1 Microfluidic system setup

Figure 3.4 depicts the resultant microfluidic platform, which comprises two asymmetric chambers joined together with an adhesive UV-curable glue. Two device designs with round and square 1.8 mm-cross-section channels were fabricated to examine the influence of geometric factors while simulating vessel profiles in healthy and blocked conditions (i.e., clogged stented artery).

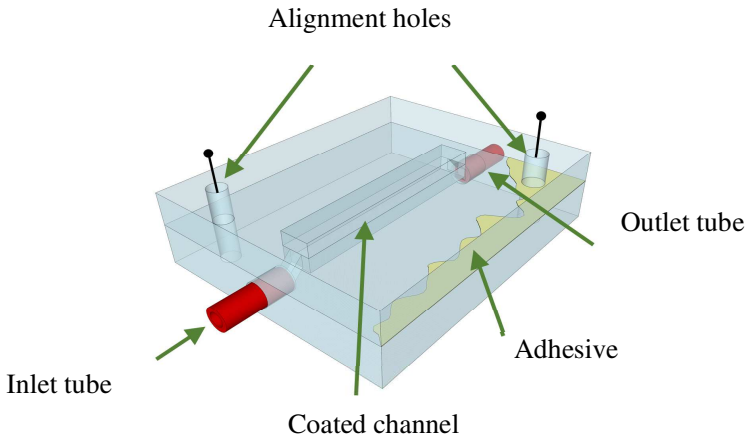

***Figure 3.4**. A 3D schematic of the assembled device.*

The preparation of the simulated blood fluid "SBF_ws" followed the chemical composition of human blood plasma (Table 3.2) in terms of ion concentrations. Additionally, during the preliminary stages of this study, several media with various amounts of urea, glycerol, and water were examined. The final characteristics of each two- and three-component "SBF_wgu" solution are listed in Table 3.2 and Figure 3.5.

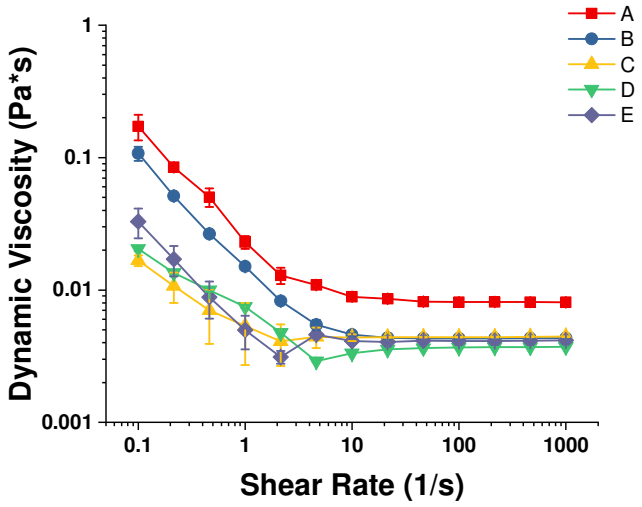

***Figure 3.5**. Dynamic viscosity as a function of shear rate of simulated blood fluid (SBF) solutions. Relationships between dynamic viscosity and shear rate for water/glycerol (wg) and water/glycerol/urea (wgu) solutions.*

***Table 3.2.** Dynamic viscosity values for water-glycerol solutions, with and without urea.*

Legend	Water (wt%)	Glycerol (wt%)	Urea (wt%)	Dynamic viscosity (mPa*s)
A	44.2	55.8	-	8.9
B	54.3	45.7	-	4.6
C	44.1	34.5	21.4	4.4
D	45.6	28.8	25.6	3.3
E	44.8	32.8	22.4	4.1

A release medium that included 32.8% w/w and 22.4% w/w urea was chosen as particularly suitable for our application and used in all subsequent experiments. In particular, compared to other fluids described in the literature that are frequently used in degradation and/or release tests, the dynamic viscosity (4.1 mPa*s) and pH (7.3) values of the chosen solution were closer to the physiological range.

Figure 3.6 depicts the microfluidic device setup processes and the final system configuration. The channels were sprayed with the rutin-loaded zein solution for 6 seconds before the chambers were assembled and put on top of a clean glass slide. The chips were connected to the peristaltic pump, and two different SBFs and mice blood were used as flowing media. The pump, which was joined to the inlet tube of each device, regulated the fluid flow rate. The final experimental setup also included the output collector vials and a heated reservoir containing the SBFs.

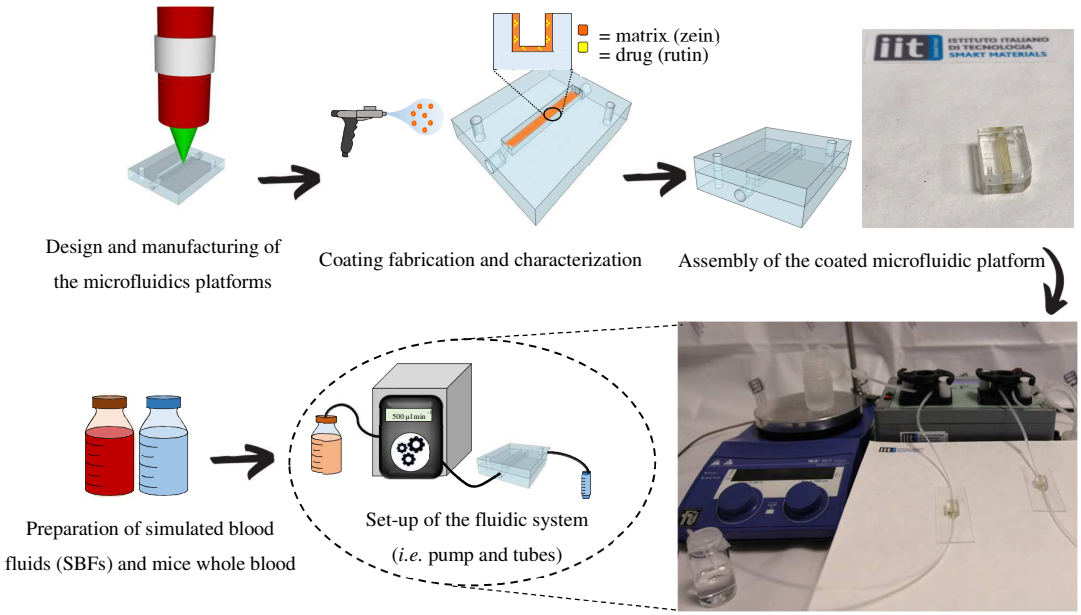

Figure 3.6. *Illustration of the setup of the microfluidic system.*

Alternatively, the chips might be placed in an incubator and eventually employed to study stimuli-responsive materials by applying external triggers. The quartz glass chips were also highly long-lasting, allowing several cleaning and recycling operations. The set flow rate of 500 µL/min was in the range of the blood speed calculated for the diameter of the fabricated vessel-mimicking devices [204].

3.3.2 Three-dimensional computational fluid dynamics

The hydrodynamic field characteristics in each microfluidic device were computed using computational fluid dynamics (CFD) analysis (COMSOL Multiphysics package & ANSYS). Figure 3.7 a, b illustrates a sequence of vertical cross-sections showing the local flow conditions in the channels. Even while the fluid dynamics behavior results similar in the area of interest, closer inspection of Figure

3.7 c, d reveals the following: in the first 100-150 microns from the glass walls towards the center of the channel, the velocity field of the fluid is almost zero (semi-stationary bearing effect). This is not a surprising finding in a microfluidic study. However, given that the drug-containing polymer matrix has a thickness of 6-7 µm, it is safe to assume that the process of drug release and matrix degradation is primarily driven by an erosion mechanism or an unforced diffusion mechanism that is based on the biochemical affinities and/or concentration gradients of the different species. The active molecule, in particular, diffuses through the fluid, reaches the most central flow lines, and is carried toward the exit. Continuous exchange with a fresh solution medium (as in the human body) prevents saturation levels from being attained, recreating the original concentration conditions that facilitate the release and degradation processes.

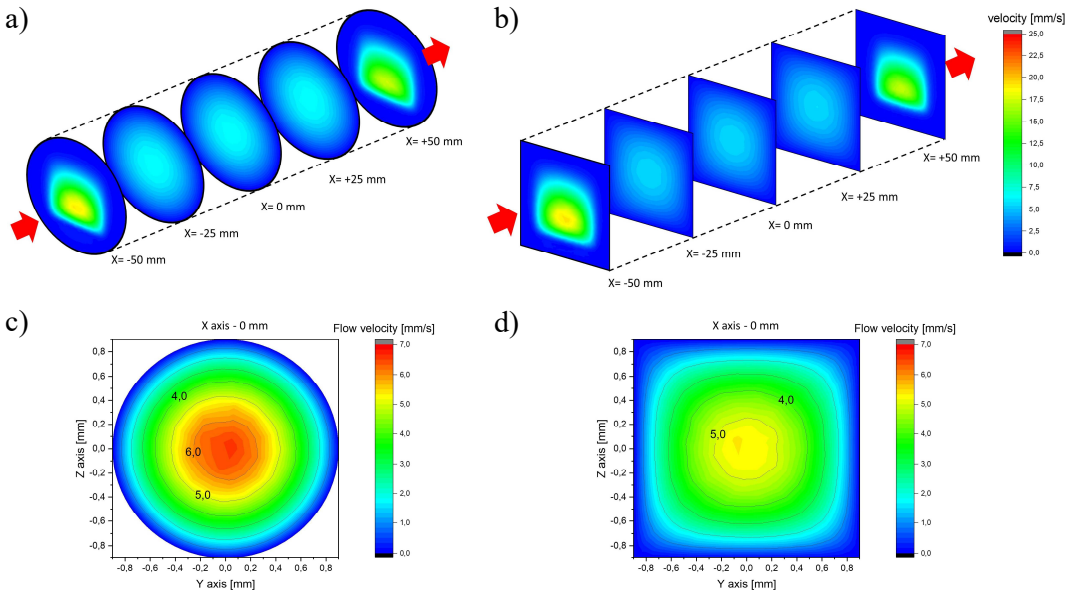

Figure 3.7. *CFD analyses. Flow velocity distributions through the whole channels (a, b) and central y-z vertical cross-sections (c, d) of the microfluidic devices were modeled using COMSOL, with the colors indicating the local velocity rate. Simulations were performed at 0.5 mL/min.*

3.3.3 Characterization of zein-based coated channels

The surface morphologies of the ZR-coated channels are shown in Figure 3.8. During the fabrication steps of the chips, the channels were not polished down to optical quality in order to ensure maximum adhesion of the polymeric material to the fused silica-based substrate. The channels looked evenly covered and devoid of fractures based on SEM observations (Figure 3.8 a, b).

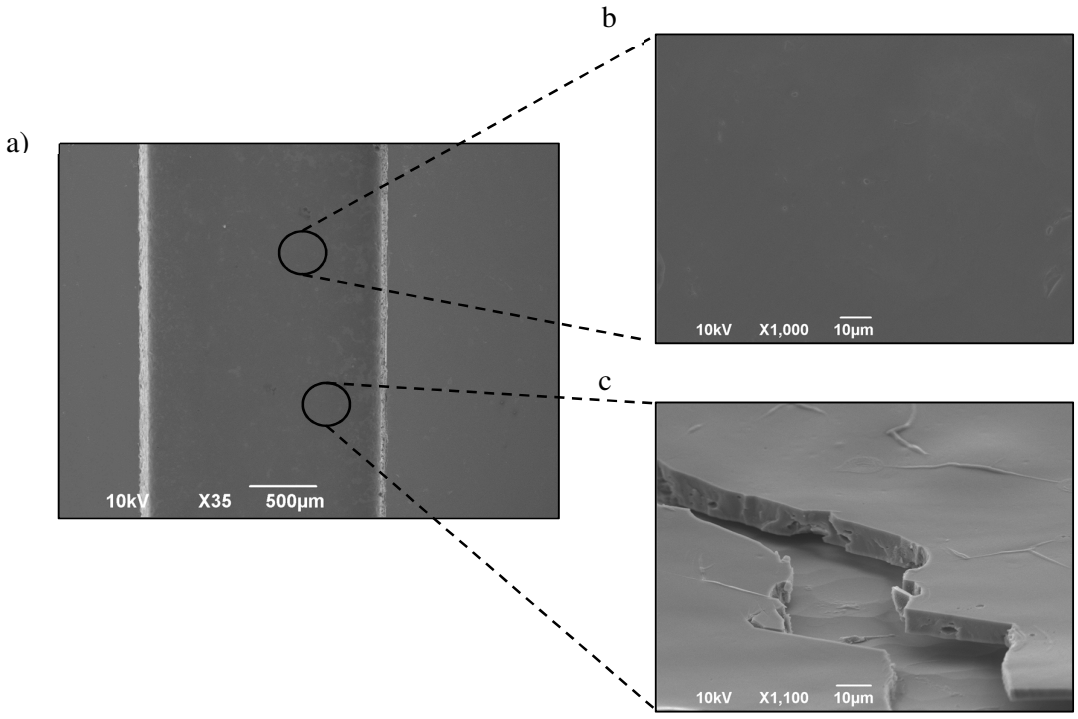

Figure 3.8. *Morphological characterization of a coated channel. SEM images at different magnifications, showing the bottom of a coated channel and the cross-section view of the ZR coating after being intentionally scratched.*

Different magnifications show how the coating is uniformly applied from the bottom to the channel borders (Figure 3.9), accurately simulating a uniformly coated drug-eluting stent that adheres to a vascular wall. This aspect is of critical importance since coating homogeneity is crucial to guarantee a uniform drug delivery to the blood vessel and decrease therapeutic risks [205].

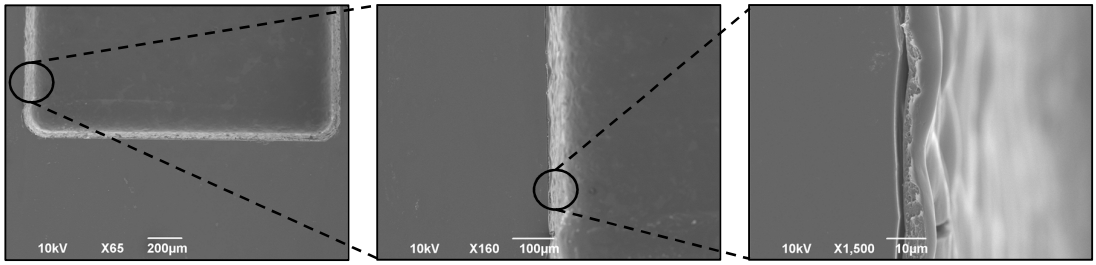

Figure 3.9. *Morphological characterization of the edges of a coated channel.*

A stylus profilometer was used to measure the coating surface roughness, and comparable results were extrapolated for chambers with round and square cross-sections (Table 3.3). The surface roughness, also visible in Figure 3.9, is mainly caused by the spray deposition process involving the adhesion and spreading of impacting spray droplets of the ZR solution.

Table 3.3. *Physico-chemical properties of the rutin-loaded zein coating deposited on the fused silica-based channels.*

Coating Material	**Water contact angle (°)**	**Coating thickness (µm)**	**Arithmetic roughness (nm)**
Rutin-loaded Zein	60.5 ± 2.6	6.6 ± 0.5 (square channel) 7.5 ± 0.2 (round channel)	403.0 ± 74.6 (square channel) 438.5 ± 54.9 (round channel)

After the samples were intentionally scratched using a lancet, the stylus profilometer was used to measure the thickness of the coatings at the bottom of each channel. As stated in Table 3.3, similar values were found on round and square cross-section chambers. Figure 3.10 provides an example of a measurement on a round ZR-coated channel (thickness value = 7.5 µm). These results were comparable to those obtained from SEM cross-section images; in particular, a value of 7.2 µm was calculated using the ImageJ software from Figure 3.8c.

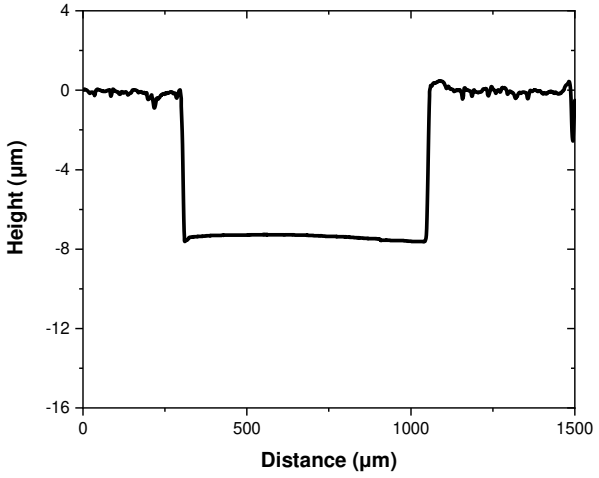

Figure 3.10. *A stylus profilometer scan showing the thickness of the ZR coating on a round microfluidic channel.*

Finally, based on the measurements of the water contact angle, the surface wettability of the coated substrates was obtained, and experimental results showed that the ZR-coated chambers display a mean water contact angle of 60.5° (Table 3.3). The ability of the zein to make the surfaces more hydrophobic was therefore confirmed: in the case of clean stainless steel (Chapter 2 Paragraph 2.3.8), the value changed from 28.9° to 38.7°, and in the case of fused silica increased changes from 52.6° to 60.5° when applying a rutin-loaded zein layer.

3.3.4 Matrix degradation studies

The ZR-coated channels were subjected to two aqueous SBFs at a constant flow rate of 500 µL/min for up to 6 hours in order to examine the kinetics of coating degradation. The polymer release emerged more sharply in the initial step than in the succeeding phases of the experiments. The composition of the working fluids significantly affected the overall polymer degradation: more specifically, a difference in the zein release profiles was observed within the first hour for round cross-section channels (34.5 ± 3.2% with SBF_ws and 23.1 ± 2.5% with SBF_wgu, Figure 3.11a) and the square cross-section channels (38.6 ± 2.9% with SBF_ws and 33.7 ± 4.9% with SBF_wgu, Figure 3.11b).

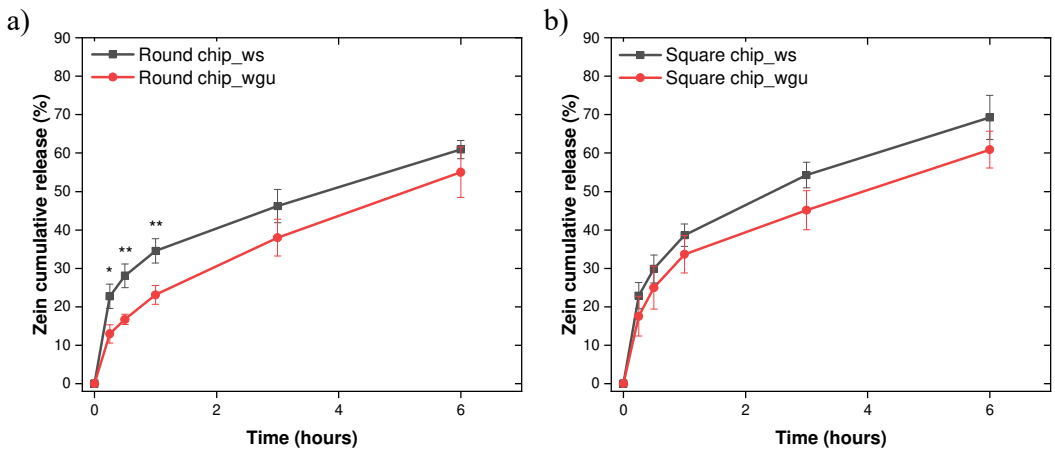

Figure 3.11. *Zein degradation kinetics. Cumulative percentage of zein mass released from round (a) and square (b) ZR-coated channels. Data are presented as mean ± SD (n = 3), which were statistically analyzed using Student's t-test. * p < 0.05, ** p < 0.01.*

Interestingly, the use of SBF_ws resulted in an early formation of more leachable zein fragments, which would speed up the loss of film material. According to previous researches, an increase in the amount of salt ions in the flowing media may stimulate the hydrolysis and be the primary factor causing this rise in fragment release [54, 206]. Furthermore, SBF_wgu not only has a lower salt content but, since it is more viscous than SBF_ws, it has a more streaming resistance, and so it flows slower through the channel. When the flow rate is lowered, so may the degradation rate, resulting in prolonged degradation times for the coated samples [207]. In addition, the inclusion of glycerol in SBF_wgu might explain the reduced zein degradation rates throughout the 6-hour time period (round channel: 55.0 ± 6.6%; square channel: 60.9 ± 4.8%): this plasticizer molecule not only enhances the viscosity of the layer at the fluid-coating interface, but it may also inhibit film swelling. As a result, initial fragment and subsequent zein diffusion across this glycerol-rich aqueous layer become more challenging, and polymer erosion resistance may increase [208].

As shown in Figures 3.11a and 3.11b, the initial "burst effect" release in the delivery kinetics is slightly faster for the square cross-section channel (e.g., after 30 minutes, SBF_ws: 29.8 ± 3.6%, SBF_wgu: 25.0 ± 5.6%) compared to the round cross-section one (SBF_ws: 28.1 ± 3.1%; SBF_wgu: 16.7 ± 1.3%). The square channel shape, which led to a larger exposed area of the polymer matrix to the flow of the release medium, is responsible for this small yet not statistically significant variance. Overall, it can be concluded that the zein coatings were likely degrading as a result of the water molecules of the release media directly penetrating into the films and generating zein amide bond breaks in the swollen areas.

3.3.5 Morphological changes during degradation assays

After performing dynamic experiments at various time periods, changes in the surface morphology of the zein-coated channels were studied under the SEM. The results are displayed in Figures 3.12 and 3.13. At time t = 0, zein coatings displayed a uniformly compact surface, while degradation signs could be seen at all subsequent time points. After the release media flowed, the samples showed a surface that became progressively more porous over time.

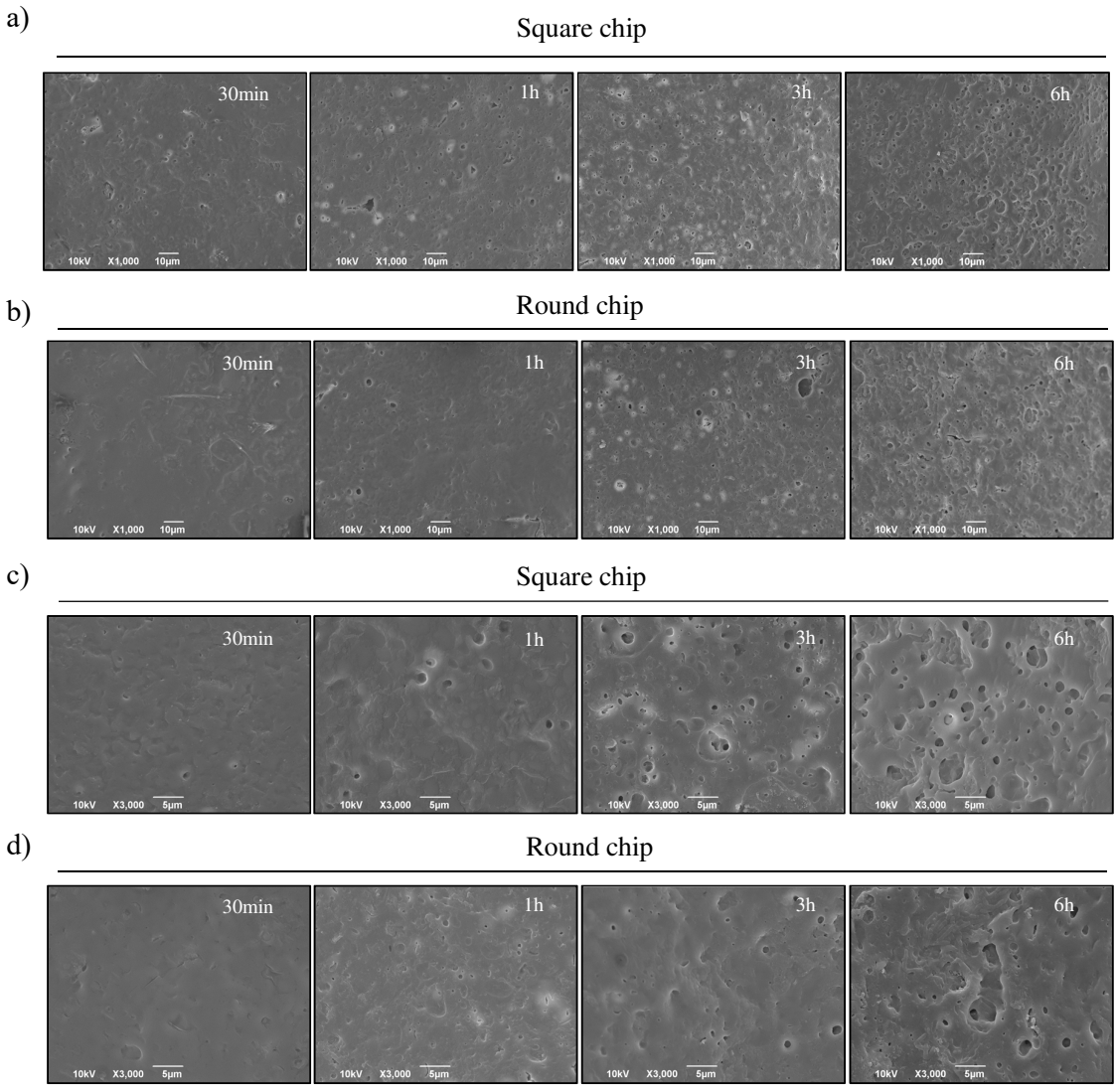

Figure 3.12. *SEM morphologies obtained from the coated channels with SBF_ws as flowing medium. Representative SEM images at different magnifications of the square (a, c) and round (b, d) chip were taken at different time points (from 30 minutes to 6 hours).*

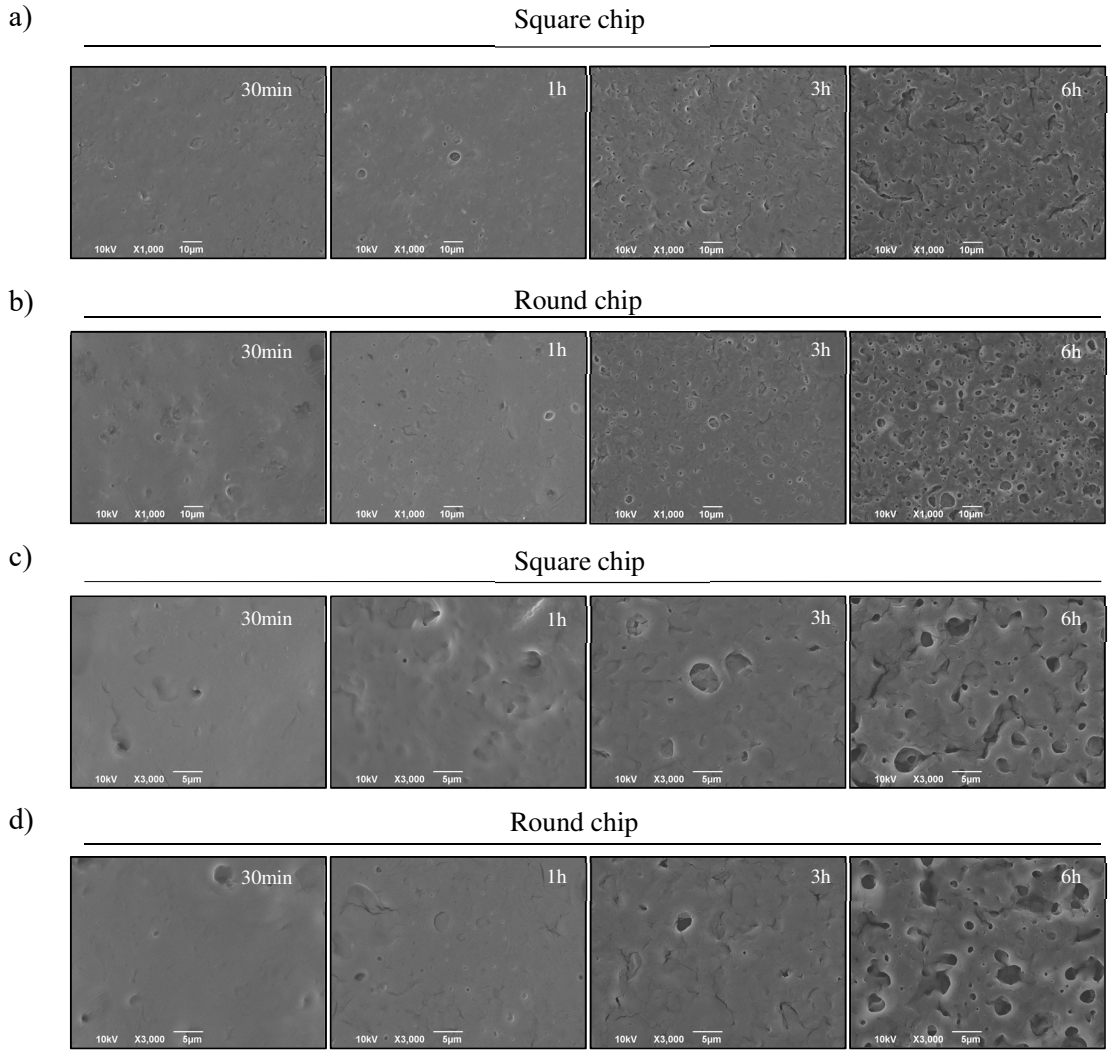

Figure 3.13. *SEM morphologies obtained from the coated channels with SBF_wgu as flowing medium. Representative SEM images at different magnifications of the square (a, c) and round (b, d) chip were taken at different time points (from 30 minutes to 6 hours).*

Since the pore surface areas and diameters are larger in the samples in Figure 3.12, SBF_ws appears to be a more aggressive and erosive fluid than SBF_wgu (Figure 3.13) from a qualitative analysis. These findings are consistent with those shown in Figure 3.11, which shows the concentrations of the zein eluted samples measured using a spectrophotometer. On the other hand, surface topography differences were not observed when distinct channel geometries were examined, confirming the previously reported non-statistically different degradation data in Figure 3.11.

Cross-sections of the degraded coatings were also inspected by SEM, showing the residual coating thickness gradually diminished over time (Figure 3.14); nevertheless, after 6 hours of flow, the zein layer still uniformly covered the underlying substrate.

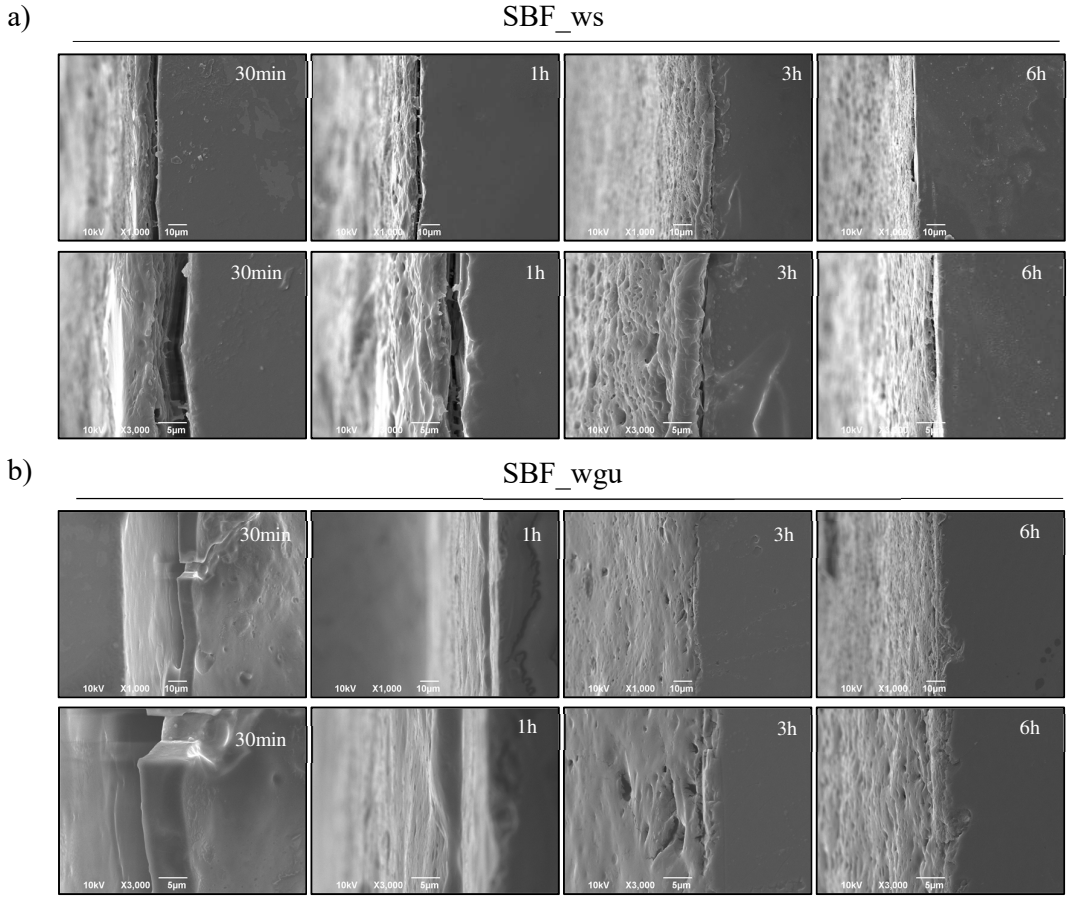

Figure 3.14. *Morphological changes observed on the edge of the channels during the degradation process. Low and high magnification of SEM images of the edges of the coated channels at different time points with SBF_ws (a) and SBF_wgu (b) as flowing media.*

Overall, the degradation products did not peel off as large fragments, indicating an optimal degradation behavior of the zein matrix and good adhesion between the coating and the substrate. These findings demonstrate that the surface roughness of the microfluidic channels formed using the FLICE manufacturing approach contributes to the polymer adhesion strength. As further proof, the zein absorption peaks (270 nm) recorded at the UV spectrophotometer were frequently represented as well-defined curves, and no broad peaks were observed in the spectra area at 320 nm, which is typically associated with large protein aggregation.

3.3.6 Drug release kinetics

Rutin release from ZR-coated channels was investigated in the two microfluidic devices for 6 hours by flowing SBF_ws and SBF_wgu at 37 °C. Figure 3.15 depicts the influence of eluting media composition on the rutin release rate, with the cumulative percentage of drug released displayed as a function of time. After 6 hours, the released quantities of rutin into the SBF_ws fluid within the round and square microfluidic chips were 77.0 ± 6.9% and 80.8 ± 7.2%, respectively. Values of 73.8 ± 4.5% and 78.1 ± 8.5% were obtained for the round and square channels, respectively, when using the SBF_wgu. There were no statistically significant changes in the quantities of drug released when comparing the two fluids or from the channels with different geometry.

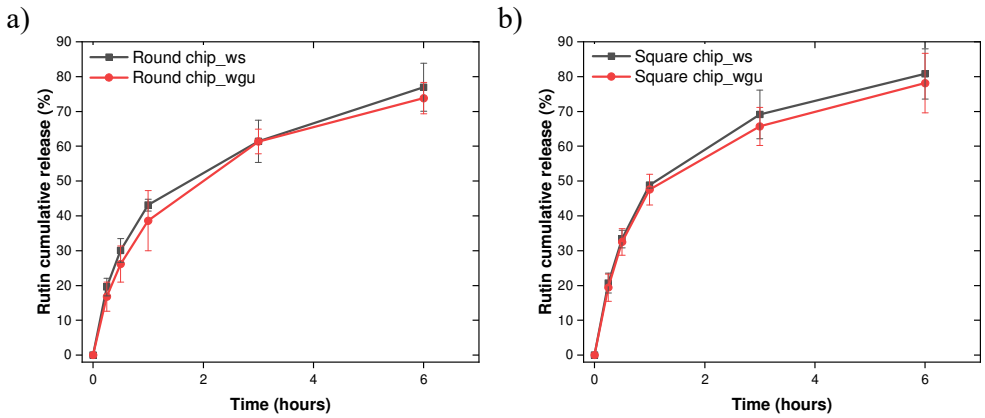

Figure 3.15. *Rutin release kinetics. Cumulative percentage of rutin mass released from round (a) and square (b) ZR-coated channels. Data are presented as mean ± SD (n = 3), which were statistically analyzed using Student's t-test. * $p < 0.05$, ** $p < 0.01$.*

To get a clearer idea of the drug-polymer interaction, a comparison between the release kinetics of zein and rutin from each type of channel with the two different elution media was carried out (Figure 3.16). An initial burst release of both rutin and zein within the first 15 - 30 minutes of the assays was detected in all the conditions. Following that, the drug release appears to be faster than the polymer degradation process, suggesting that diffusion processes primarily drive the rutin release kinetics at this stage.

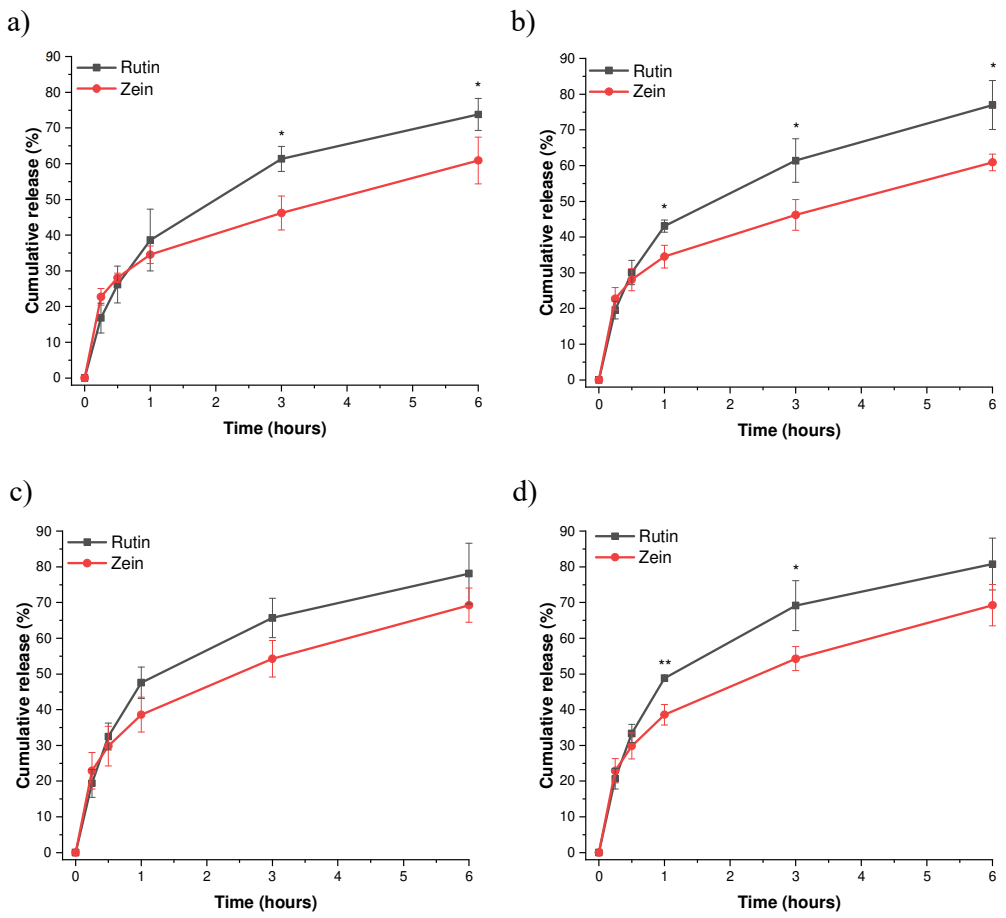

Figure 3.16*. Comparison between drug and polymer release from ZR-coated microfluidic chips. Zein and rutin release from round (a, b) and square (c, d) channels in the presence of continuous SBF_wgu (a, c) and SBF_ws (b, d) flows. Data are presented as mean ± SD (n = 3), which were statistically analyzed using Student's t-test. * p < 0.05, ** p < 0.01.*

3.3.7 Mathematical modeling of drug release

To get further insight into the rutin delivery mechanisms from the degradable zein matrix, mathematical models were used alongside release experimental studies [195]. In particular, the equations described in paragraph 3.2.8 were fitted with the cumulative release data (Figure 3.15). The Korsmeyer-Peppas (Figure 3.17 a, b) and first-order models (Figure 3.17 c, d) were the most accurate for the mathematical description of rutin delivery kinetics. Table 3.4 provides r^2 and K values – the measure of goodness-of-fit and the model constant, respectively – for all samples.

Table 3.4. *Mathematical model fitting values obtained from rutin release kinetics. Bold values indicate the best fits.*

Cross-section	SBF	Zero-order		First-order		Higuchi		Korsmeyer-Peppas		Hixson-Crowell	
		r^2	K	r^2	K	r^2	K	r^2	n	r^2	K
Round	ws	0.8996	0.1525	0.9764	-0.0015	0.9745	3.6812	**0.9774**	0.4198	0.9564	-0.004
Round	wgu	0.8908	0.1558	0.9618	-0.0014	0.9723	3.7758	**0.9805**	0.4653	0.9414	-0.0039
Square	ws	0.8457	0.1576	0.9517	-0.0017	0.9446	3.8637	**0.9565**	0.4193	0.9215	-0.0044
Square	wgu	0.8462	0.1519	**0.9492**	-0.0015	0.9434	3.7206	**0.9489**	0.4226	0.9199	-0.0041

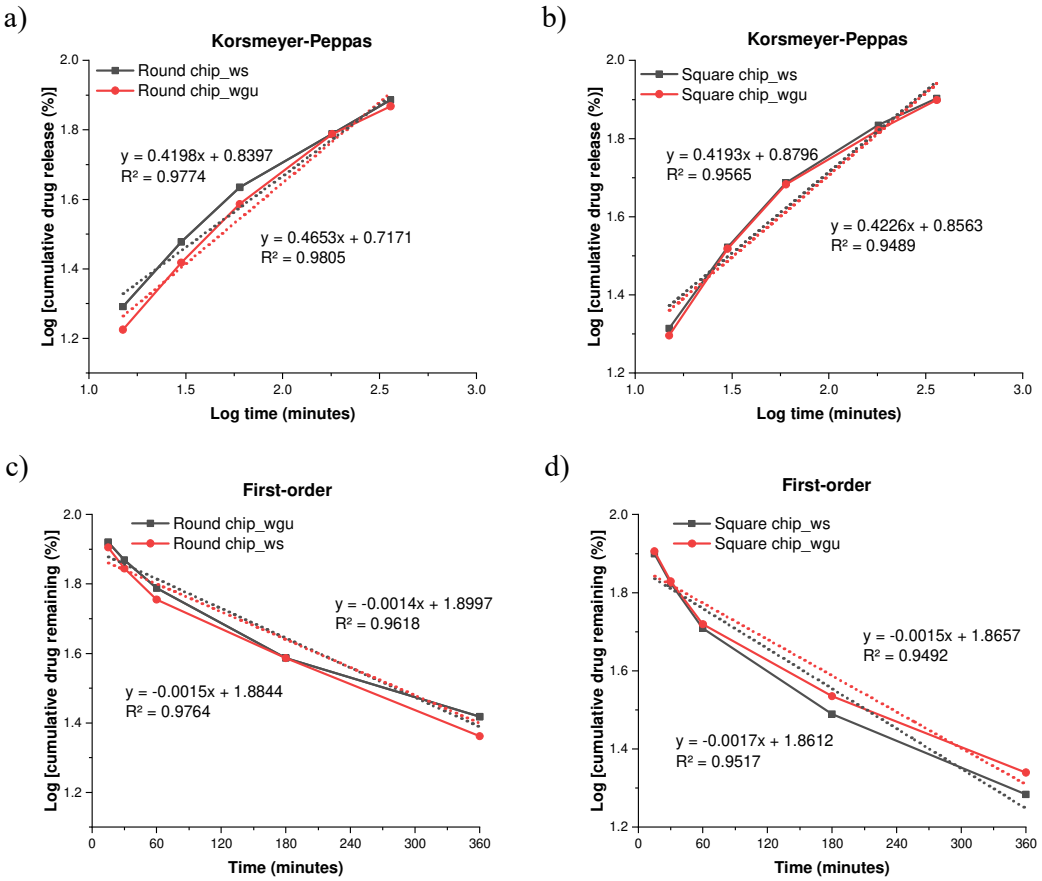

Figure 3.17. *Rutin release fitting profiles. Rutin release profiles were fitted to different mathematical models, among which the Korsmeyer-Peppas (a, b) and first-order (c, d) models resulted to be the most accurate. These models could help understand the mechanism of rutin release from round (a, c) and square (b, d) coated channels with different flow fluids.*

Rutin release from zein matrices is thought to occur through the partially swollen zein layer and to be primarily controlled by a Fickian diffusion (i.e., the diffusion rate of the penetrating solvent is much greater than the relaxation and degradation rate of the polymeric chains), as suggested by the n coefficients of the Korsmeyer- Peppas model, which lay below 0.5 for both configurations and both

fluids [195]. Furthermore, analyzing two sections of the release curves independently provided an additional interpretation of the release process (Table 3.5). The Higuchi model was determined to be the best fit with a greater correlation ($r^2 > 0.99$) during the first time period of up to one hour. When the Korsmeyer-Peppas model was used to fit the same data, the results showed high linearity ($r^2 > 0.99$) with slope values between 0.5 and 1.0, indicating that the release rate was controlled by diffusion, relaxation (swelling), and erosion mechanisms of the zein polymeric coatings, as already suggested by the findings in Figures 3.14 and 3.16 [209]. The Korsmeyer-Peppas and first-order models, the latter referring to a system where the drug release rate is a function of the residual drug concentration, were found to have the greatest r^2 values when the second time period (60 minutes - 6 hours) was examined. The n coefficients from the Korsmeyer-Peppas model were less than 0.5, confirming that the release kinetics were mostly diffusion-controlled throughout the last sessions of the experiments. The kinetics of a hydrophilic drug, such as rutin, from a partly hydrophobic matrix, such as zein, often involve diffusion as well as matrix erosion. Berardi et al. provided a similar explanation for the tramadol release mechanism from zein tablets in phosphate buffer solutions [210].

Table 3.5. *Mathematical model fitting values obtained from rutin release kinetics for different time periods. Bold values indicate the best fits.*

Cross-section	SBF	Analyzed time (min)	Zero-order	First-order	Higuchi	Korsmeyer-Peppas		Hixson-Crowell
			r^2	r^2	r^2	r^2	n	r^2
Round	ws	0 - 60	0.9835	0.9935	**0.9986**	0.9974	0.5696	0.9907
Round	ws	60 - 360	0.974	0.9989	0.9983	**1**	0.3237	0.9942
Round	wgu	0 - 60	0.9881	0.9954	**0.9997**	0.9986	0.6004	0.9934
Round	wgu	60 - 360	0.9222	0.9729	0.974	**0.9871**	0.3672	0.9583
Square	ws	0 - 60	0.9825	0.9948	**0.9983**	0.9958	0.6204	0.9915.
Square	ws	60 - 360	0.9282	0.9819	0.9775	**0.9923**	0.2843	0.9691
Square	wgu	0 - 60	0.9776	0.992	**0.9965**	0.9924	0.6472	0.988
Square	wgu	60 - 360	0.9512	0.9903	0.9897	**0.9982**	0.2785	0.9804

Overall, the mathematical modeling confirmed that the degradation process of zein coatings in aqueous media partially influences the rutin release behavior: (1) the drug initial burst release is caused by the rapid displacement of physically-adsorbed rutin molecules; (2) pores are formed within the amphipathic zein matrix upon water contact; and (3) these pores in the matrix serve as an additional drug transport pathway, allowing the drug to be released faster. Compared to the static studies reported in Chapter 2, Paragraph 2.3.5, zein degradation and rutin release were quicker and more continuous

when experiments were carried out under dynamic settings. The most likely explanation for these results is that the constant liquid flow caused more rapid infiltration of water molecules within the polymer matrix, and the ZR surface experienced a constant removal of the drug/polymer top layer, resulting in the maintenance of a continuous concentration gradient, avoidance of medium saturation, and accelerated polymer degradation.

3.3.8 Static blood cells adhesion assays

Wettability, chemical composition, surface charge, and roughness are all critical characteristics in the hemocompatibility of medical devices and materials, and they have an impact on cell and protein adsorption during the early stages of the material-blood interaction [211]. Using whole blood for *in vitro* assays has the advantage of testing the thrombotic system in its entireness. In this study, several samples were pre-conditioned and incubated in fresh mouse blood for 30 minutes under static conditions at 37 °C. As widely known from the literature, evidence of platelet activation may be inferred from the shape of adherent platelets [187, 189]. The morphology of blood cells on different substrates is presented in Figure 3.18. 316L SS surfaces were also examined for comparative purposes, since, as it is acknowledged in the literature, the trade-off for the mechanical advantage of metals is thrombogenicity [212]. The majority of platelets on steel (Figure 3.18e) exhibited aggregation, significant pseudopodia development, and shape modifications (i.e., spreading), as confirmed by the literature [205]. On the other hand, the partial hydrophobicity of the corn-derived material may account for the limited number of platelets that adhered to the zein-based coatings (Figure 3.18 a, b). According to several authors, surfaces with hydrophilic components of polar functional groups often encourage cell attachment as opposed to surfaces with non-polar hydrophobic components. However, the coagulation system may also be affected by other factors such as the binding and conformation of plasma proteins, surface chemistry, charge, and roughness [188]. Few platelets spread completely onto the rutin-loaded surfaces (Figure 3.18b), where a reduction in platelet activation was observed, and only a few platelets began to adopt a dendritic morphology. On the other hand, many of the adhering platelets to the drug-free zein coating assumed a dendritic shape (Figure 3.18a). This results might be attributed to (1) the electrostatic repulsion between the platelet negative charges and the rutin molecules and (2) the drug natural anti-coagulant capabilities, which have been previously observed to successfully suppress platelet activation and thrombus formation [159, 213].

The same experimental protocol has also been followed for testing other reference materials (PU and PLA), currently under investigation in the literature as potential DES coatings. In particular, severe platelet aggregation was seen on the PU-coated surfaces (Figure 3.18c), indicating poor hemocompatibility of the material, as previously described for other classes of polyurethanes [214]. On the other hand, a high number of erythrocytes was detected on PLA surfaces (Figure 3.18d), likely owing to the shape and specific surface area of this synthetic polymer, which allowed more cells to attach, as previously observed by Ji et al [215]. Moreover, on the PLA surfaces, fibrin gel network was densely present above and around red blood cells, suggesting a preliminary stage of blood clot formation.

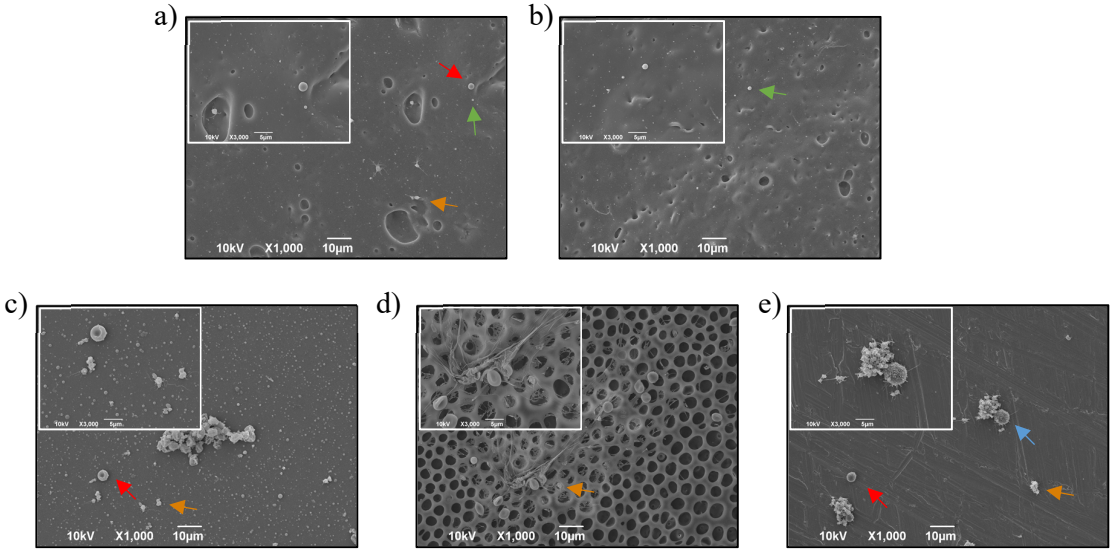

Figure 3.18. *SEM images of adhered platelets. Representative SEM images with magnified insets show the morphology of the platelets adhered on zein (a), rutin-loaded zein (b), polyurethane (c), PLA (d), and stainless steel (e). Arrows indicate red blood cells (red), white blood cells (cyan), resting platelets (green) and activated platelets (orange).*

Figure 3.19 shows platelet adhesion and activation levels on the tested sample surfaces. On the zein-based coatings without and with rutin, the average number of adherent and activated platelets per mm^2 was 617 (333 exhibited activated morphology) and 775 (179 showed activated morphology), respectively. As a comparison with different naturally-derived materials, Kim et al. studied the platelet adhesion phenomena on alginate hydrogel films, with and without $CaCl_2$ crosslinking, which showed a density of 700 platelets/mm^2 and 840 platelets/mm^2, respectively [173]. A comparable number of cells was found onto silk fibroin films, while several authors tested chitosan-coated surfaces and measured more than 3500 adherent platelets per mm^2 [216, 217]. Bare metal samples reported an average numbers of adherent and activated platelets per mm^2 of 2877 and 2489, respectively. The average number of adherent and activated platelets per mm^2 were 2930 and 808 for the PU coating and 790 and 156 for the PLA coating, as shown in Figure 3.19. The latter showed a similar behavior compared to what was

observed by Kim et al. with PLGA-coated substrate (~875 adherent platelets/mm^2) [173]. The amounts of adherent cells on both PU and SS samples were significantly higher than those on PLA and zein-based samples, with a high degree of spreading and aggregation. It has to be noted that it was often not possible to distinguish individual platelets in large clots; here, the average number of adherent and activated platelets on PU and SS surfaces was estimated from areas where the cells were more well-separated.

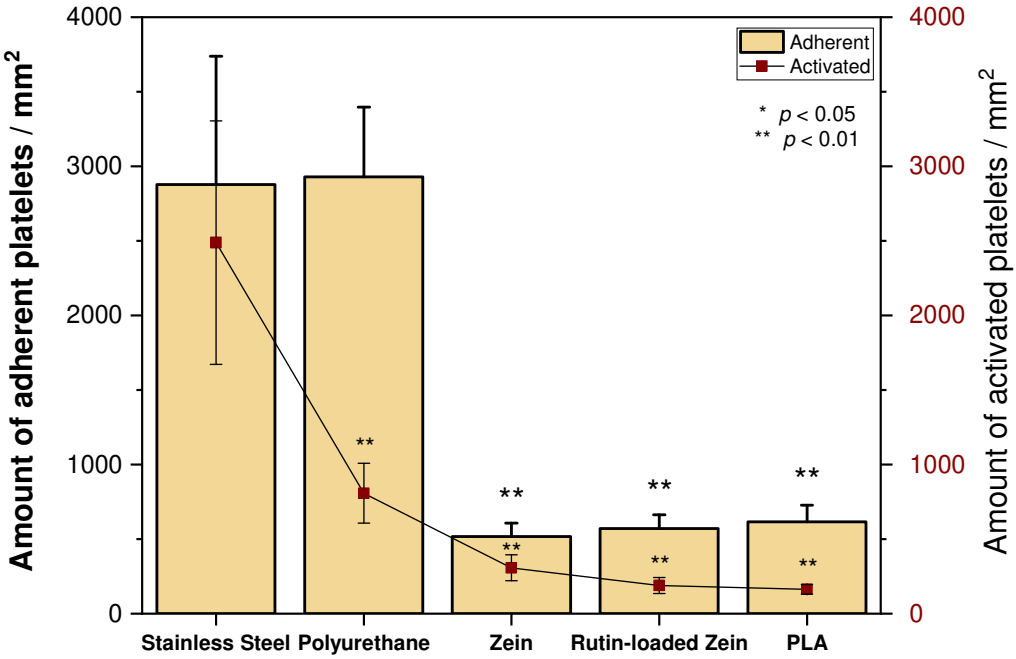

Figure 3.19. *Static blood cells adhesion assays. Data are presented as mean ± SE, which were statistically analyzed using one-way ANOVA followed by post-hoc Tukey's test. * $p < 0.05$, ** $p < 0.01$.*

3.3.9 Hemolysis assays

Erythrocyte-induced hemolysis *in vitro* is considered another reliable and essential parameter in order to evaluate the hemocompatibility of a blood-contacting material. Table 3.6 provides a summary of the hemolysis rates obtained from zein-based films and reference samples following a 30-minutes incubation protocol with whole blood at 37 °C.

Table 3.6. *Hemolysis rate for stainless steel, zein-based coatings, and other reference materials.*

Sample surface	Hemolysis Rate (%)
Normal saline (negative control)	0
Stainless Steel	1.20 ± 0.54
Rutin-loaded zein	2.43 ± 0.63
Poly(lactic acid)	3.00 ± 0.21
Zein	3.66 ± 1.02
Polyurethane	22.08 ± 1.61
Distilled water (positive control)	100

The zein and rutin-loaded zein samples revealed low hemolysis rates of 3.66 ± 1.02% and 2.43 ± 0.63%, respectively, which are lower than the judging criterion (5%) for eligible blood compatibility for any implantable biomedical materials, according to the ISO 10993-4 norm [201]. Other coatings fabricated from different naturally-derived materials showed similar hemolysis rates of less than 5% (i.e., silk fibroin, β-glucan, chitosan, and collagen) [175, 218, 219]. According to the literature, a low percentage of hemolysis was obtained from bare stainless steel (1.20 ± 0.54%) and PLA-coated samples (3.00 ± 0.21%). On the contrary, PU-coated samples showed more than 20% hemolysis rates, resulting in non-hemocompatible coating materials [205, 220].

3.3.10 Polystyrene beads dynamic experiments

Attachment of 5-µm diameter PS particles, using dilute suspensions that resemble the concentration of red blood cells (RBCs) in human blood, might provide an early insight into the coating ability to attract and allow particles or flowing cells to adhere to itself. The zeta potential of 5-µm PS particles dispersed in SBF_wgu was -4.6 ± 0.1 mV and -7.4 ± 1.1 mV in SBF_ws. This difference might be explained by the presence of glycerol molecules on the surface of the particles, which could reduce the zeta potential values due to steric hindrance. PS beads were chosen and employed to replicate RBCs behavior in terms of quantity, size, negative charge, and density. Although such particle model has limits and definitely does not mimic all of the complexity involved in an *in vivo* setting, it can be beneficial in gaining preliminary insights into adhesion events at the zein/liquid interface. In both

SBF_ws and SBF_wgu media, optical microscope pictures at different magnifications revealed well-dispersed PS particles (Figure 3.20).

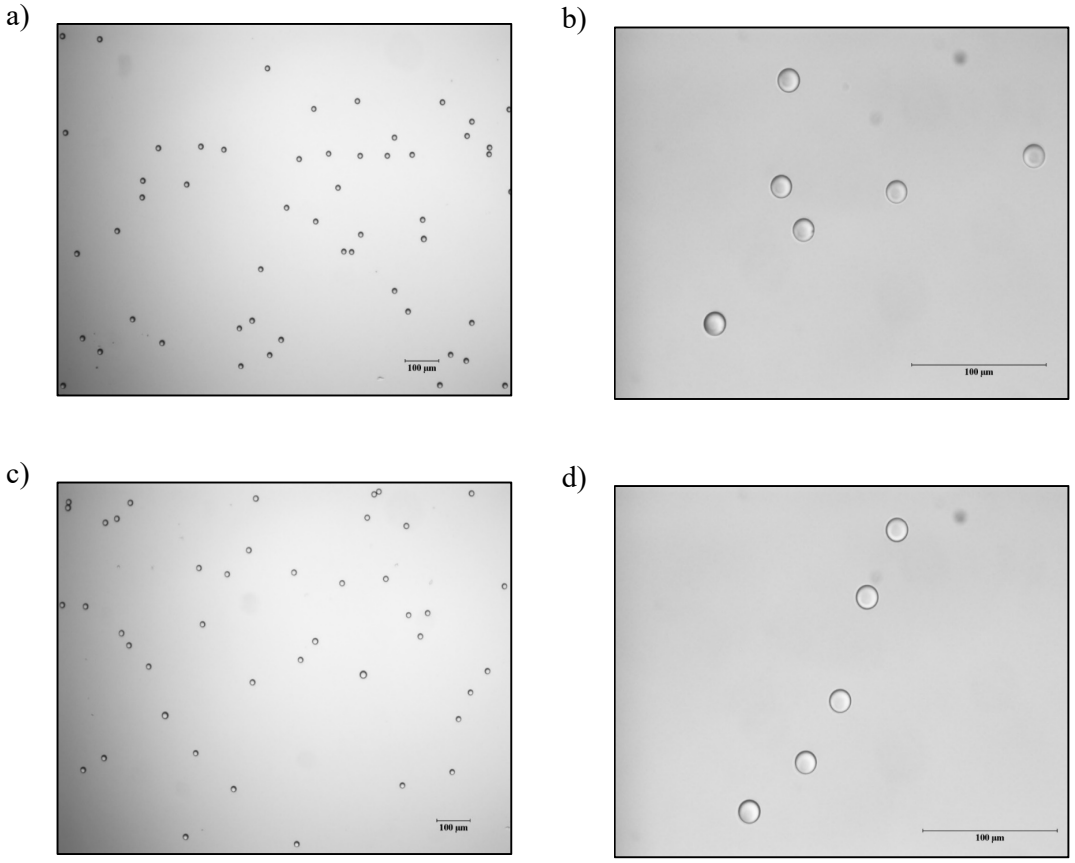

Figure 3.20. *Optical microscopy images of diluted PS beads. The beads were suspended (5 x 10^6 particles/mL) in SBF_ws solution (a, b) and SBF_wgu solution (c, d).*

A preliminary examination was carried out to assess PS beads adherence and the morphology of the ZR-coated channels after 30 minutes of dynamic experiments. The particles shown in Figure 3.21 a-d likely adhered to the ZR coatings due to van der Waals, hydrophobic and electrostatic interactions with the zein matrix. According to the SEM images, their adhesion on the coated surface is very low, although they are abundant in the fluids (5 x 10^6 beads/mL).

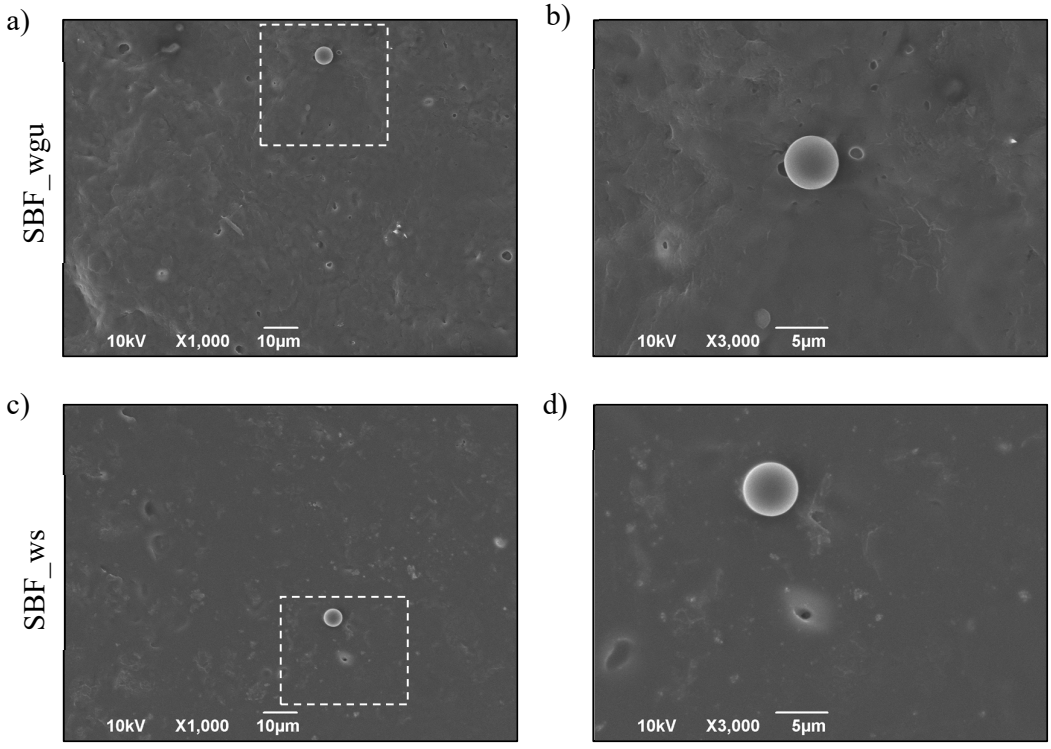

Figure 3.21. *PS beads adhesion on ZR-coated channels. SEM images were acquired after 30 minutes of flow of PS beads dispersed in SBF_wgu (a, b) and SBF_ws (c, d). Images on the right (b, d) are higher magnification of the dashed box area in images (a, c).*

When comparing the pictures acquired with PS beads dispersed in the two SBFs, no considerable change was observed in the number of adhering particles or the coating morphology. When the SEM images in Figures 3.12 and 3.13 were compared in a qualitative analysis, a slightly more degraded matrix area was detected, probably owing to solid particle erosion (Figure 3.21 a-d). This effect can be attributed to the repetitive dynamic impact of fast-moving suspended particles in the fluid onto the surface material [221].

3.3.11 Whole blood dynamic experiments

Dynamic whole blood tests were conducted at a flow rate of 500 µL/min for 10 minutes to study the hemocompatibility of the ZR coating and the feasibility of the microfluidic devices for assessing DES coating thrombogenicity. Despite the fact that various research groups have frequently fixed the flow time at 4-5 minutes employing parallel-flow chambers, thrombus development typically occurs within 5-8 minutes on physiological surfaces [151, 222]. Furthermore, whereas many studies only use platelet-rich plasma (PRP) to test the blood compatibility of selected materials, whole blood flow tests

were used in this project to integrate the cumulative contributions of blood cells, coagulation factors, and hemodynamic forces into the process of thrombus formation on selected materials. After the flowing experiment, the formation of blood clots, platelet adhesion, and their morphologies within the microfluidic channel were examined. Clot formation generally serves as one of the most important *in vitro* indicators for assessing the blood compatibility of a material. Under blood flow, the formation of clots is primarily fueled by the adsorption of plasma proteins followed by the adhesion of blood cells on the implant surface [188]. In addition, the shape and size of platelets can change within a few seconds in response to a triggering stimulus, being the activation level of adherent platelets closely connected with their morphology (i.e., platelets extrude pseudopodia upon activation, assuming a dendritic shape until completely spread) [211]. Even though only a few articles have reported SEM pictures for both platelet adhesion and activation assessment after completing dynamic blood tests, the samples were here investigated using electron microscopy techniques rather than fluorescent methods [223-225]. Nevertheless, being light-transparent, the fused silica-based chips could also be used in combination with brightfield or fluorescence microscopy. Representative SEM images, acquired after the dynamic blood experiments, are depicted in Figure 3.22 (a-c), which shows a small number of adhered platelets, and an even smaller number of activated platelets, onto the ZR coating (~3.2% area coverage with blood cells), and only occasionally visible red blood cells. For comparison, Ollivier et al. reported a value of ~18% from the platelet coverage experiment on bare cobalt-chromium discs within 10 minutes of flow [226]. Under the same conditions, Sarvepalli et al. showed that platelet adhesion on a collagen-coated surface had exceeded 80% of the available surface area in a microfluidic chamber [227].

No presence of fibrin networks containing trapped blood cells, as seen for example in Figure 3.18d on the PLA-coated surfaces, and no sign of platelet aggregation was found on the surface of the zein-based coatings. The observed platelets showed a spherical shape with a rare development of pseudopodia growing from their surface, indicating a non-activated phenotype.

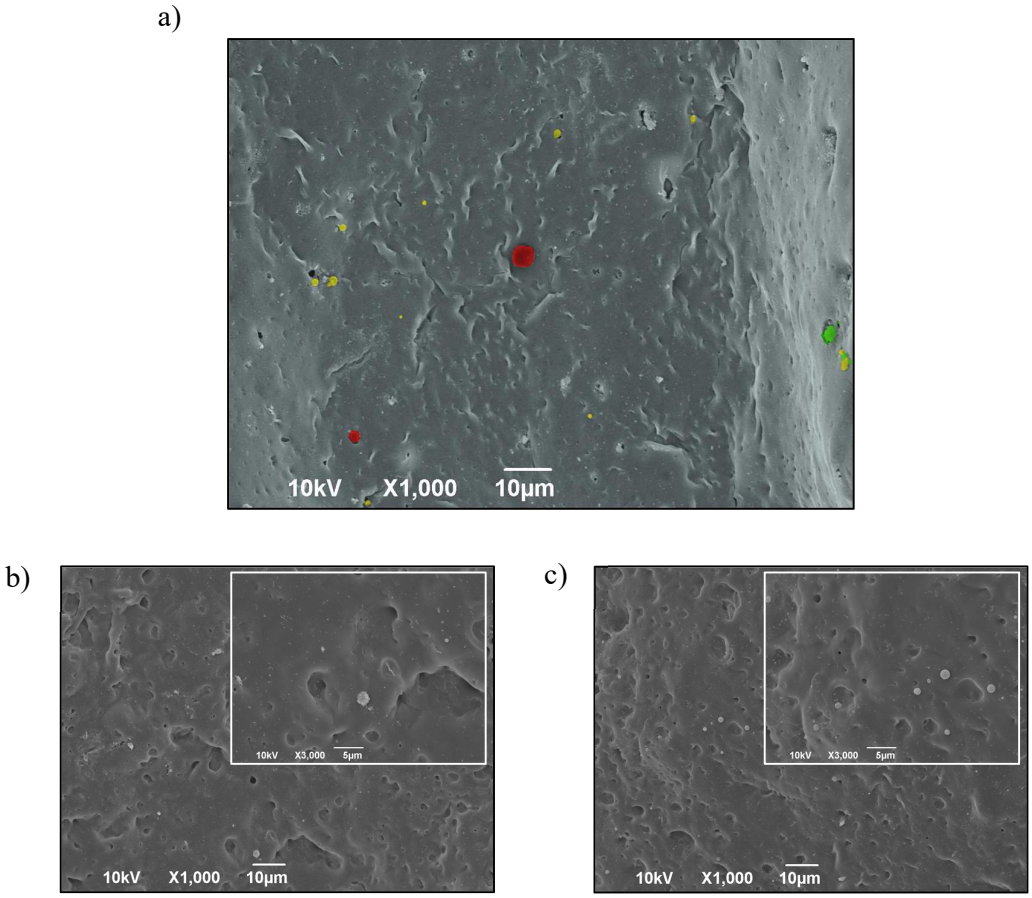

Figure 3.22. *SEM image of adherent blood cells on ZR-coated microfluidic channel acquired after a 10 minutes flow. A red blood cell (red), resting platelets (yellow), and slightly activated platelets with pseudopodia formation (green) are colored in (a) by using Mountains Map software from Digital Surf (Besançon, France).*

SEM images of the zein matrix tested under blood flow revealed more intense degradation than those obtained after the experiments with aqueous SBFs solutions (Figure 3.12 and Figure 3.13). This outcome was most likely caused by the enzymatic action of various proteases exerted on the protein matrix, as expected from the prior results shown by Suarato et al [93]. Data obtained from the static tests are consistent with those from the dynamic whole blood tests and showed how this plant-based, drug-loaded matrix could provide a safe coating material for stent application. These results are particularly relevant to the physiological situation in partially occluded blood vessels, where platelet behavior can have a significant impact on the onset of adverse effects and is of primary interest when developing materials for stent coating.

3.4 Conclusions

This chapter section is partially taken from Lenzuni M. et al., "Dynamic investigation of zein-based degradable and hemocompatible coatings for drug-eluting stents: a microfluidic approach" RSC Lab on a Chip (2023).

In this second PhD project, a simple, reusable, fused silica-based microfluidic platform was designed and validated. The proposed platforms allowed a quantitative analysis of the influence of the flow environment and channel geometry on the degradation and drug release kinetics of DES coatings. The developed microfluidic structure might be used to investigate various working fluids and flow rates, as well as multiple coating types (degradable or non-degradable) that can be deposited using a variety of processes (such as casting and spray methods). The current investigation focused on the effect of different SBFs and geometrical characteristics of the microfluidic channels on the degradation and drug release profiles of naturally-derived zein-based coatings. According to the results, the release media had a more significant impact on the polymer degradation profile than the geometrical form (round vs. square) of the channels. In particular, the zein matrix was degraded faster when a higher concentration of salt ions (simulating the physiological blood plasma milieu) was added to the eluting medium. The drug release mechanism from the zein coatings was subsequently determined by mathematical modeling of the rutin delivery kinetics, which revealed a diffusion-controlled (Fickian) behavior, according to the Korsmeyer-Peppas model. Variations in polymer mass and surface topography of the coatings were also analyzed and compared in order to better understand release behavior and to guide future *in vivo* experiments.

Hemocompatibility constitutes another leading requirement when designing blood-contacting materials for vascular devices. While the dynamics of blood cell activation are frequently overlooked during blood tests, in this work, a whole blood assay was carried out under controlled physiologically flow conditions using the fused silica-based microfluidic approaches to evaluate the antithrombotic properties of the ZR material. The proposed plant-based coating was found to be hemocompatible from the results of the hemolysis assays (< 5%) and the static and dynamic whole blood cell adhesion experiments. Particularly, SEM images analysis revealed that the zein-based coatings significantly reduced platelet adhesion and activation when compared to reference substrates (bare stainless steel or waterborne polyurethane). Detection methods such as contrast-enhanced microscopy could have helped to visualize adhered platelets in real-time, but such a technique is unable to inform on their activation levels and does not provide qualitative information on thrombus composition [150]. Alternative approaches could have detected platelets by labeling them with DiOC6, fluorescein, or fluorescent antibodies [143, 228]. However, fluorescent tags are not only expensive and require intensive sample manipulation, but they may also affect the biological functions and adhesion affinity of the target molecules. Moreover, counting the platelets is not achievable when all platelets are fluorescently labeled

since the close packing makes it impossible to distinguish between individual platelets. In addition to the aging light sources, photo-bleaching, and detector gain manual adjustments, the fluorescence intensity measured in a single focal plane may underestimate the number of aggregating platelets [229].

To conclude, our microfluidic systems, manufactured into non-deformable and completely inert substrates such as fused silica, represent versatile tools for release, degradation, and hemocompatibility studies, mimicking DES design and blood environment. More importantly, our plant-based materials have been demonstrated to be a safe alternative to synthetic polymers as coatings for blood-contacting biomedical devices, such as stents.

Chapter 4 - Conclusions and Future perspectives

4.1 Conclusions

The increasing risk of CHD throughout the globe has been of critical concern and will ultimately lead to a rising share of the population experiencing stent-related pathologies such as restenosis and thrombosis. PCI has evolved from balloon angioplasty through bare metal stents and now to the dominant contemporary platform, the drug-eluting stent. The exploitation of local drug release has certainly reduced the incidence of stent restenosis at the cost of endothelial healing, resulting in heterogeneous and incomplete endothelial reconstitution, a factor strongly associated with stent thrombosis. Since the stents are in contact with the vascular system, the cytocompatibility with vascular cells (e.g., endothelial cells and fibroblasts) and the non-thrombogenicity of their surfaces are essential features. Improving the biocompatibility properties of cardiovascular DES, together with tuning their drug release kinetics, are thought to be the most promising strategies for solving the problem of restenosis and thrombosis, usually associated with disastrous patient outcomes.

Due to their biodegradability, excellent biocompatibility, and chemical tailorability, naturally-derived polymers have been extensively investigated for the development of drug delivery systems. Under this perspective, in the present PhD thesis work, plant-derived coatings for DES were developed to offer new drug release platforms and improve the stent cyto- and hemocompatibility. Static and dynamic analyses were carried out to assess the performances of the proposed materials. The goal was to design a more biocompatible stent coating through natural polymers and drugs, exclusively employing green solvents.

In the first PhD project, single and double-layer coatings were developed and characterized, taking advantage of the innovative use of plant-based, biodegradable polymers, which constitute a promising alternative to permanent synthetic DES coatings. In particular, zein-based coatings have been evaluated for their controlled-release ability because of their slow biodegradability, low cost, biocompatibility, and non-immunogenicity. Rutin, acting as the active compound, was successfully loaded into the zein coatings, and its sustained release and anti-oxidant effects were assessed. Among the studied polymers, cross-linked alginate resulted the best sacrificial covering layer since it showed strong attachment to the protein layer and delayed release kinetics of the underlying drug. The strategy of cross-linking with calcium ions was preferred over the conventional cross-linking with glutaraldehyde, genipin, or metal complexes, given the high toxicity of these chemicals, which would

diverge from our green fabrication standards and might interfere with the final biological application. Lastly, the applicability of single and bilayer coatings to the vascular system was established by positively evaluating the attachment and proliferation of HUVEC and HDFa over the prepared plant-based layers.

On the other hand, there is a time window prior to endothelialization when stents are exposed to the bloodstream. Although the stenting procedure is well established, it is clear from clinical data that there is a large void of comprehension of coatings impact in preventing thrombosis. Moreover, hydrodynamic forces play a crucial role in coating wetting, polymer degradation, mass loss, drug release, and thrombogenicity of the tested materials. The understanding of dynamic interactions between DES coatings and blood flow is still at an early stage. Instruments, such as USP Apparatus 4 (Flow-through Cell) or USP Apparatus 7 (Reciprocating Holder), try to recreate a physiological flow in static sample cells to simulate the human hemodynamic environment. In addition to the high cost of these devices, the flow field inside such large instruments results non-homogenous and causes the drug to be released at different rates from distinctive regions of the samples [185, 190, 230]. Moreover, simulated blood fluids (SBFs) are frequently prepared with Tween 20, Triton-X100, Pluronic, or other surfactants, which could not accurately simulate the blood components. In this scenario, microfluidic chips have been indicated as superior tools to replicate biological processes and provide simple to operate and high-throughput techniques for material screening, unlike *in vivo* experiments, which are often hampered by the complexity of the results, high cost, time consumption, and ethical issues. In the second project of the PhD thesis, *ad hoc* designed microfluidic chips were fabricated on fused-silica substrates via FLICE technique with round and square cross-section areas to mimic key flow dynamic properties of a stented artery. Our microfluidic technology has demonstrated significant potential as a versatile tool for investigating drug-carrying coating behavior, in this case rutin-loaded zein coatings, under the influence of a uniform fluid field. The two main important features were assessed, i.e., drug release and matrix degradation kinetics, which are recognized to be two interconnected phenomena. Based on the assays conducted, the release medium properties (e.g., salt ions concentration) were found to significantly affect the profile of polymer degradation, while rutin delivery kinetics were mathematically modeled and revealed a diffusion-controlled (Fickian) behavior in accordance with the Korsmeyer-Peppas models. Lastly, using the proposed devices, the hemocompatibility properties of the proposed zein-based coatings were assessed with a small blood sample volume and proved to satisfy all the requirements, in particular low platelet adhesion and activation levels compared to reference substrates. The fused silica-based devices were extremely durable and were recycled and reused multiple times, thus allowing us to adopt green work habits during research in laboratories.

Overall, the results obtained in these PhD multi-disciplinary research projects and the knowledge generated on the processing of biocompatible and biodegradable zein-based biomaterials can serve as guidelines for the further employment of plant proteins as green materials replacing animal proteins and synthetic polymers for a wide range of biomedical applications, such as coatings for stents.

4.2 Future Perspectives

The work reported in this PhD thesis has paved the way for a multitude of future research. Based on the drug release studies discussed in Chapter 2 and Chapter 3, further optimization of the coatings might be required to reduce the burst release effect from zein matrices. To this end, one approach could be the covalent bonding and modification of the interaction between drug molecules and the coating materials. Additional layers or drugs can be added to fabricate a multifunctional coating that, at the same time, should result cost-effective, easily applied, non-toxic, and have optimal temporal and continuous dosing. Copolymers and polymer blends could allow for hybrid properties (e.g., combining polymers with slow degradation rate with materials showing optimal cell proliferative capabilities).

Moreover, femtosecond laser-assisted direct manufacturing techniques (e.g., FLICE) demonstrated several advantages in terms of adaptability (such as the freedom to create unique 3D designs) and prototyping speed compared to traditional methods. The ability to mimic the *in vivo* topography of complex biological systems offers several critical advantages, leading to results that can closely resemble *in vivo* observations. Our microfluidic platform demonstrated a solid proof of concept and needs validation by testing other (bio)materials. In particular, the chips are highly versatile and can be adapted to test a range of blood-contacting coatings with different properties (e.g., degradability, tunable thickness) upon exposure to different flow dynamic conditions. This will contribute to identify optimal strategies for the future development of DES.

To better understand how stenting influenced intravascular hemodynamics, the intravascular flow conditions are often predicted by CFD. It would be of value to employ CFD simulations to reproduce human blood as particulate within the proposed fused silica-based microfluidic devices. Our data could serve as input conditions to the CFD models to create models that can predict polymer degradation and/or drug release kinetics after DES implantation. Experimental measurement and computational simulations could complement each other to provide new insights into the properties of novel drug-eluting coatings. This would help to predict the behavior of drug-eluting stent coatings with any design at any condition using computational methods.

For the foreseeable future, metallic alloys will remain the material of choice for coronary stents due to the benefits of radial strength, deformation characteristics, and radio-opacity, as described in Chapter 1. Polymers on stents are usually applied using spray or dip coating technology. An innovative system that could be investigated in order to produce DES coatings is electrospraying. This electrodynamic approach allows the production of micro- or nanoparticles in the ground electrode by spraying a polymer solution in an electric field at high voltage. As the solvent(s) evaporate during the spraying process, droplets of the polymer solution are created. To date, very few studies have been published in the literature on coating biomedical implants with electosprayed particles. Ongoing

experiments focus on producing and characterizing zein-based particles on SS substrates. Since implantation-associated infections are one of the most commonly encountered complications leading to a long healing process and even implant failure, future work will concern the incorporation of antimicrobial agents to prevent the formation and growth of biofilm on DES surface and the development of infectious diseases.

References

1. Amini, M.; Zayeri, F.; Salehi, M., Trend analysis of cardiovascular disease mortality, incidence, and mortality-to-incidence ratio: results from global burden of disease study 2017. *BMC Public Health* **2021,** *21* (1), 401.
2. Ullah, M.; Wahab, A.; Khan, S. U.; Zaman, U.; Rehman, K. u.; Hamayun, S.; Naeem, M.; Ali, H.; Riaz, T.; Saeed, S.; Alsuhaibani, A. M.; Refat, M. S., Stent as a Novel Technology for Coronary Artery Disease and Their Clinical Manifestation. *Current Problems in Cardiology* **2023,** *48* (1), 101415.
3. Libby, P., The molecular mechanisms of the thrombotic complications of atherosclerosis. *Journal of Internal Medicine* **2008,** *263* (5), 517-527.
4. Libby, P., Inflammation in atherosclerosis. *Nature* **2002,** *420* (6917), 868-874.
5. Khan, M. A. B.; Hashim, M. J.; Mustafa, H.; Baniyas, M. Y.; Al Suwaidi, S. K. B. M.; AlKatheeri, R.; Alblooshi, F. M. K.; Almatrooshi, M. E. A. H.; Alzaabi, M. E. H.; Al Darmaki, R. S.; Lootah, S. N. A. H., Global Epidemiology of Ischemic Heart Disease: Results from the Global Burden of Disease Study. *Cureus* **2020,** *12* (7), e9349.
6. Chaabane, C.; Otsuka, F.; Virmani, R.; Bochaton-Piallat, M.-L., Biological responses in stented arteries. *Cardiovascular Research* **2013,** *99* (2), 353-363.
7. Hansson, G. K., Immune mechanisms in atherosclerosis. *Arterioscler Thromb Vasc Biol* **2001,** *21* (12), 1876-90.
8. Feinleib, M., Seven countries: A multivariate analysis of death and coronary heart disease. *Jama* **1981,** *245* (5), 511-512.
9. Zaman, A. G.; Aleem, Q., Pharmacology before, during and after percutaneous coronary intervention. *Heart* **2021,** *107* (7), 585-592.
10. Jennings, S.; Bennett, K.; Shelley, E.; Kearney, P.; Daly, K.; Fennell, W., Trends in percutaneous coronary intervention and angiography in Ireland, 2004-2011: Implications for Ireland and Europe. *Int J Cardiol Heart Vessel* **2014,** *4*, 35-39.
11. Gudiño, E. a.; Oishi, C. M.; Sequeira, A. l., Multiscale Boundary Conditions for Non-Fickian Diffusion Applied to Drug-Eluting Stents. *SIAM Journal on Applied Mathematics* **2017,** *77* (4), 1184-1203.
12. Zhao, Y.; Meng, S.; Liu, T.; Dong, R., Economic Analysis of Surgical and Interventional Treatments for Patients with Complex Coronary Artery Disease: Insights from a One-Year Single-Center Study. *Med Sci Monit* **2020,** *26*, e919374.
13. Sigwart, U.; Puel, J.; Mirkovitch, V.; Joffre, F.; Kappenberger, L., Intravascular stents to prevent occlusion and restenosis after transluminal angioplasty. *N Engl J Med* **1987,** *316* (12), 701-6.
14. Roguin, A., Stent: The Man and Word Behind the Coronary Metal Prosthesis. *Circulation: Cardiovascular Interventions* **2011,** *4* (2), 206-209.
15. Dotter, C. T.; Buschmann, R. W.; McKinney, M. K.; Rösch, J., Transluminal expandable nitinol coil stent grafting: preliminary report. *Radiology* **1983,** *147* (1), 259-260.
16. Serruys, P. W.; Kutryk, M. J. B.; Ong, A. T. L., Coronary-Artery Stents. *New England Journal of Medicine* **2006,** *354* (5), 483-495.
17. Yang, K.; Ren, Y.; Wan, P., High nitrogen nickel-free austenitic stainless steel: A promising coronary stent material. *Science China Technological Sciences* **2012,** *55* (2), 329-340.
18. Buccheri, D.; Piraino, D.; Andolina, G.; Cortese, B., Understanding and managing in-stent restenosis: a review of clinical data, from pathogenesis to treatment. *J Thorac Dis* **2016,** *8* (10), E1150-E1162.
19. Hamid, H.; Coltart, J., 'Miracle stents'--a future without restenosis. *Mcgill J Med* **2007,** *10* (2), 105-11.
20. Inoue, T.; Croce, K.; Morooka, T.; Sakuma, M.; Node, K.; Simon Daniel, I., Vascular Inflammation and Repair. *JACC: Cardiovascular Interventions* **2011,** *4* (10), 1057-1066.
21. Anderson, J. M.; Rodriguez, A.; Chang, D. T., Foreign body reaction to biomaterials. *Semin Immunol* **2008,** *20* (2), 86-100.
22. Tesfamariam, B., Endothelial Repair and Regeneration Following Intimal Injury. *J Cardiovasc Transl Res* **2016,** *9* (2), 91-101.
23. Wang, J.; Jin, X.; Huang, Y.; Ran, X.; Luo, D.; Yang, D.; Jia, D.; Zhang, K.; Tong, J.; Deng, X.; Wang, G., Endovascular stent-induced alterations in host artery mechanical environments and their roles in stent restenosis and late thrombosis. *Regen Biomater* **2018,** *5* (3), 177-187.
24. Deloose, K.; Bosiers, M.; Peeters, P.; Verbist, J.; Maene, L.; Beelen, R.; Keirse, K.; Hendriks, J.; Lauwers, P.; Wauters, J.; Verschueren, M., Combining the Passeo-18 Lux Drug-Coated Balloon and the Pulsar-

18 Bare Metal Stent: 12- and 24-Month Outcomes of the BIOLUX 4EVER Investigator-Initiated Trial. *J Endovasc Ther* **2020,** *27* (6), 936-945.
25. Kipshidze, N.; Dangas, G.; Tsapenko, M.; Moses, J.; Leon, M. B.; Kutryk, M.; Serruys, P., Role of the endothelium in modulating neointimal formation: vasculoprotective approaches to attenuate restenosis after percutaneous coronary interventions. *J Am Coll Cardiol* **2004,** *44* (4), 733-9.
26. Waksman, R., Drug-eluting stents: from bench to bed. *Cardiovasc Radiat Med* **2002,** *3* (3-4), 226-41.
27. Wang, Q.; Fang, G.; Zhao, Y.-H.; Zhou, J., Improvement of Mechanical Performance of Bioresorbable Magnesium Alloy Coronary Artery Stents through Stent Pattern Redesign. *Applied Sciences* **2018,** *8* (12), 2461.
28. Ceresnakova, M.; Dully, M.; Murray, D.; Soulimane, T.; Hudson, S. P., Stent conditioned media for in vitro evaluation of hydrophobic stent coatings. *Toxicology in Vitro* **2021,** *76*, 105212.
29. Deb, P. K.; Kokaz, S. F.; Abed, S. N.; Paradkar, A.; Tekade, R. K., Chapter 6 - Pharmaceutical and Biomedical Applications of Polymers. In *Basic Fundamentals of Drug Delivery*, Tekade, R. K., Ed. Academic Press: 2019; pp 203-267.
30. Dangas, G. D.; Claessen, B. E.; Caixeta, A.; Sanidas, E. A.; Mintz, G. S.; Mehran, R., In-Stent Restenosis in the Drug-Eluting Stent Era. *Journal of the American College of Cardiology* **2010,** *56* (23), 1897-1907.
31. Reejhsinghani, R.; Lotfi, A. S., Prevention of stent thrombosis: challenges and solutions. *Vasc Health Risk Manag* **2015,** *11*, 93-106.
32. Garg, S.; Serruys, P. W., Coronary stents: current status. *J Am Coll Cardiol* **2010,** *56* (10 Suppl), S1-42.
33. Joner, M.; Finn, A. V.; Farb, A.; Mont, E. K.; Kolodgie, F. D.; Ladich, E.; Kutys, R.; Skorija, K.; Gold, H. K.; Virmani, R., Pathology of drug-eluting stents in humans: delayed healing and late thrombotic risk. *J Am Coll Cardiol* **2006,** *48* (1), 193-202.
34. Kerner, A.; Gruberg, L.; Kapeliovich, M.; Grenadier, E., Late stent thrombosis after implantation of a sirolimus-eluting stent. *Catheter Cardiovasc Interv* **2003,** *60* (4), 505-8.
35. Lefèvre, T.; Haude, M.; Neumann, F. J.; Stangl, K.; Skurk, C.; Slagboom, T.; Sabaté, M.; Goicolea, J.; Barragan, P.; Cook, S.; Macia, J. C.; Windecker, S., Comparison of a Novel Biodegradable Polymer Sirolimus-Eluting Stent With a Durable Polymer Everolimus-Eluting Stent: 5-Year Outcomes of the Randomized BIOFLOW-II Trial. *JACC Cardiovasc Interv* **2018,** *11* (10), 995-1002.
36. Rebagay, G.; Bangalore, S., Biodegradable Polymers and Stents: the Next Generation? *Current Cardiovascular Risk Reports* **2019,** *13* (8).
37. Bangalore, S.; Toklu, B.; Amoroso, N.; Fusaro, M.; Kumar, S.; Hannan, E. L.; Faxon, D. P.; Feit, F., Bare metal stents, durable polymer drug eluting stents, and biodegradable polymer drug eluting stents for coronary artery disease: mixed treatment comparison meta-analysis. *Bmj* **2013,** *347*, f6625.
38. Beshchasna, N.; Saqib, M.; Kraskiewicz, H.; Wasyluk, L.; Kuzmin, O.; Duta, O. C.; Ficai, D.; Ghizdavet, Z.; Marin, A.; Ficai, A.; Sun, Z.; Pichugin, V. F.; Opitz, J.; Andronescu, E., Recent Advances in Manufacturing Innovative Stents. *Pharmaceutics* **2020,** *12* (4).
39. van der Giessen, W. J.; Lincoff, A. M.; Schwartz, R. S.; van Beusekom, H. M.; Serruys, P. W.; Holmes, D. R., Jr.; Ellis, S. G.; Topol, E. J., Marked inflammatory sequelae to implantation of biodegradable and nonbiodegradable polymers in porcine coronary arteries. *Circulation* **1996,** *94* (7), 1690-7.
40. Busch, R.; Strohbach, A.; Rethfeldt, S.; Walz, S.; Busch, M.; Petersen, S.; Felix, S.; Sternberg, K., New stent surface materials: the impact of polymer-dependent interactions of human endothelial cells, smooth muscle cells, and platelets. *Acta Biomater* **2014,** *10* (2), 688-700.
41. Moses, J. W.; Leon, M. B.; Popma, J. J.; Fitzgerald, P. J.; Holmes, D. R.; O'Shaughnessy, C.; Caputo, R. P.; Kereiakes, D. J.; Williams, D. O.; Teirstein, P. S.; Jaeger, J. L.; Kuntz, R. E., Sirolimus-eluting stents versus standard stents in patients with stenosis in a native coronary artery. *N Engl J Med* **2003,** *349* (14), 1315-23.
42. Lee, D. H.; de la Torre Hernandez, J. M., The Newest Generation of Drug-eluting Stents and Beyond. *Eur Cardiol* **2018,** *13* (1), 54-59.
43. Nakazawa, G., Stent thrombosis of drug eluting stent: Pathological perspective. *Journal of Cardiology* **2011,** *58* (2), 84-91.
44. O'Brien, B.; Carroll, W., The evolution of cardiovascular stent materials and surfaces in response to clinical drivers: a review. *Acta Biomater* **2009,** *5* (4), 945-58.
45. Lewis, A. L.; Vick, T. A.; Collias, A. C.; Hughes, L. G.; Palmer, R. R.; Leppard, S. W.; Furze, J. D.; Taylor, A. S.; Stratford, P. W., Phosphorylcholine-based polymer coatings for stent drug delivery. *J Mater Sci Mater Med* **2001,** *12* (10-12), 865-70.
46. Nakazawa, G.; Finn, A. V.; John, M. C.; Kolodgie, F. D.; Virmani, R., The significance of preclinical evaluation of sirolimus-, paclitaxel-, and zotarolimus-eluting stents. *Am J Cardiol* **2007,** *100* (8b), 36m-44m.
47. Mehilli, J.; Massberg, S., Revisiting the BIOSCIENCE of drug-eluting stent technology. *Lancet* **2014,** *384* (9960), 2086-8.

48. Lindquist, J.; Schramm, K., Drug-Eluting Balloons and Drug-Eluting Stents in the Treatment of Peripheral Vascular Disease. *Semin Intervent Radiol* **2018,** *35* (5), 443-452.
49. Marlies, M. K.; Paolo, Z.; Rosaly, A. B.; Peter, W. D.; Carl, E. S.; Martijn, S.; Marc, H.; Martin, G. S.; Houwelingen, K. G. v.; Gerard, C. M. L.; Carine, J. M. D.; Clemens von, B., Two-year clinical outcome of all-comers treated with three highly dissimilar contemporary coronary drug-eluting stents in the randomised BIO-RESORT trial. *EuroIntervention* **2018,** *14* (8), 915-923.
50. Costa, R. A.; Abizaid, A.; Mehran, R.; Schofer, J.; Schuler, G. C.; Hauptmann, K. E.; Magalhães, M. A.; Parise, H.; Grube, E., Polymer-Free Biolimus A9-Coated Stents in the Treatment of De Novo Coronary Lesions: 4- and 12-Month Angiographic Follow-Up and Final 5-Year Clinical Outcomes of the Prospective, Multicenter BioFreedom FIM Clinical Trial. *JACC Cardiovasc Interv* **2016,** *9* (1), 51-64.
51. Tada, N.; Virmani, R.; Grant, G.; Bartlett, L.; Black, A.; Clavijo, C.; Christians, U.; Betts, R.; Savage, D.; Su, S. H.; Shulze, J.; Kar, S., Polymer-free biolimus a9-coated stent demonstrates more sustained intimal inhibition, improved healing, and reduced inflammation compared with a polymer-coated sirolimus-eluting cypher stent in a porcine model. *Circulation: Cardiovascular Interventions* **2010,** *3* (2), 174-83.
52. Waksman, R.; Pakala, R.; Baffour, R.; Seabron, R.; Hellinga, D.; Chan, R.; Su, S.-H.; Kolodgie, F.; Virmani, R., In vivo comparison of a polymer-free Biolimus A9-eluting stent with a biodegradable polymer-based Biolimus A9 eluting stent and a bare metal stent in balloon denuded and radiated hypercholesterolemic rabbit iliac arteries. *Catheterization and cardiovascular interventions : official journal of the Society for Cardiac Angiography & Interventions* **2011,** *80* (3), 429-36.
53. Sousa, J. E.; Serruys, P. W.; Costa, M. A., New Frontiers in Cardiology. *Circulation* **2003,** *107* (17), 2274-2279.
54. Visan, A. I.; Popescu-Pelin, G.; Socol, G., Degradation Behavior of Polymers Used as Coating Materials for Drug Delivery-A Basic Review. *Polymers* **2021,** *13* (8), 1272.
55. Langer, R. S.; Peppas, N. A., Present and future applications of biomaterials in controlled drug delivery systems. *Biomaterials* **1981,** *2* (4), 201-14.
56. Rykowska, I.; Nowak, I.; Nowak, R., Drug-Eluting Stents and Balloons-Materials, Structure Designs, and Coating Techniques: A Review. *Molecules* **2020,** *25* (20).
57. Turk, M.; Gupta, V.; Fischell, T. A., Evaluation of balloon withdrawal forces with bare-metal stents, compared with Taxus and Cypher drug-eluting coronary stents: balloon, stent and polymer interactions. *J Invasive Cardiol* **2010,** *22* (3), 113-6.
58. Leon, M. B.; Mauri, L.; Popma, J. J.; Cutlip, D. E.; Nikolsky, E.; O'Shaughnessy, C.; Overlie, P. A.; McLaurin, B. T.; Solomon, S. L.; Douglas, J. S., Jr.; Ball, M. W.; Caputo, R. P.; Jain, A.; Tolleson, T. R.; Reen, B. M., 3rd; Kirtane, A. J.; Fitzgerald, P. J.; Thompson, K.; Kandzari, D. E., A randomized comparison of the Endeavor zotarolimus-eluting stent versus the TAXUS paclitaxel-eluting stent in de novo native coronary lesions 12-month outcomes from the ENDEAVOR IV trial. *J Am Coll Cardiol* **2010,** *55* (6), 543-54.
59. Ding, N.; Pacetti, S. D.; Tang, F.-w.; Gada, M.; Roorda, W., XIENCE V™ Stent Design and Rationale. *Journal of Interventional Cardiology* **2009,** *22* (s1), S18-S27.
60. Akinapelli, A.; Chen, J. P.; Roy, K.; Donnelly, J.; Dawkins, K.; Huibregtse, B.; Hou, D., Current State of Bioabsorbable Polymer-Coated Drug-Eluting Stents. *Curr Cardiol Rev* **2017,** *13* (2), 139-154.
61. Borhani, S.; Hassanajili, S.; Ahmadi Tafti, S. H.; Rabbani, S., Cardiovascular stents: overview, evolution, and next generation. *Prog Biomater* **2018,** *7* (3), 175-205.
62. Maurus, P. B.; Kaeding, C. C., Bioabsorbable implant material review. *Operative Techniques in Sports Medicine* **2004,** *12* (3), 158-160.
63. Dake, M. D.; Van Alstine, W. G.; Zhou, Q.; Ragheb, A. O., Polymer-free paclitaxel-coated Zilver PTX Stents--evaluation of pharmacokinetics and comparative safety in porcine arteries. *J Vasc Interv Radiol* **2011,** *22* (5), 603-10.
64. Rhodin, J. A. G., Architecture of the Vessel Wall. *Comprehensive Physiology* **1980**, 1-31.
65. Rogers, C.; Karnovsky, M. J.; Edelman, E. R., Inhibition of experimental neointimal hyperplasia and thrombosis depends on the type of vascular injury and the site of drug administration. *Circulation* **1993,** *88* (3), 1215-21.
66. Jiménez-Valero, S.; Moreno, R.; Sánchez-Recalde, A., Very late drug-eluting stent thrombosis related to incomplete stent endothelialization: in-vivo demonstration by optical coherence tomography. *J Invasive Cardiol* **2009,** *21* (9), 488-90.
67. Kotani, J.; Awata, M.; Nanto, S.; Uematsu, M.; Oshima, F.; Minamiguchi, H.; Mintz, G. S.; Nagata, S., Incomplete neointimal coverage of sirolimus-eluting stents: angioscopic findings. *J Am Coll Cardiol* **2006,** *47* (10), 2108-11.
68. Lange, R. A.; Hillis, L. D., Second-generation drug-eluting coronary stents. *The New England journal of medicine* **2010,** *362* (18), 1728-1730.
69. Suzuki, T.; Kopia, G.; Hayashi, S.-i.; Bailey, L. R.; Llanos, G.; Wilensky, R.; Klugherz, B. D.; Papandreou, G.; Narayan, P.; Leon, M. B.; Yeung, A. C.; Tio, F.; Tsao, P. S.; Falotico, R.; Carter, A. J., Stent-

Based Delivery of Sirolimus Reduces Neointimal Formation in a Porcine Coronary Model. *Circulation* **2001,** *104* (10), 1188-1193.
70. van Buuren, F.; Dahm, J. B.; Horskotte, D., Stent restenosis and thrombosis: etiology, treatment, and outcomes. *Minerva Med* **2012,** *103* (6), 503-11.
71. Curfman, G. D.; Morrissey, S.; Jarcho, J. A.; Drazen, J. M., Drug-eluting coronary stents--promise and uncertainty. *N Engl J Med* **2007,** *356* (10), 1059-60.
72. Stassen, J. M.; Arnout, J.; Deckmyn, H., The hemostatic system. *Curr Med Chem* **2004,** *11* (17), 2245-60.
73. Wahlgren, M.; Arnebrant, T., Protein adsorption to solid surfaces. *Trends Biotechnol* **1991,** *9* (6), 201-8.
74. Félétou, M., Integrated Systems Physiology: from Molecule to Function to Disease. In *The Endothelium: Part 1: Multiple Functions of the Endothelial Cells—Focus on Endothelium-Derived Vasoactive Mediators*, Morgan & Claypool Life Sciences
Copyright © 2011 by Morgan & Claypool Life Sciences Publishers.: San Rafael (CA), 2011.
75. Holmes, D. R., Jr.; Kereiakes, D. J.; Garg, S.; Serruys, P. W.; Dehmer, G. J.; Ellis, S. G.; Williams, D. O.; Kimura, T.; Moliterno, D. J., Stent thrombosis. *J Am Coll Cardiol* **2010,** *56* (17), 1357-65.
76. Lemesle, G.; Delhaye, C.; Bonello, L.; de Labriolle, A.; Waksman, R.; Pichard, A., Stent thrombosis in 2008: Definition, predictors, prognosis and treatment. *Archives of Cardiovascular Diseases* **2008,** *101* (11), 769-777.
77. Martina, M.; Hutmacher, D. W., Biodegradable polymers applied in tissue engineering research: a review. *Polymer International* **2007,** *56* (2), 145-157.
78. Pillai, O.; Panchagnula, R., Polymers in drug delivery. *Curr Opin Chem Biol* **2001,** *5* (4), 447-51.
79. Ong, C. S.; Zhou, X.; Huang, C.-y.; Fukunishi, T.; Zhang, H.; Hibino, N., Tissue engineered vascular grafts: current state of the field. *Expert Review of Medical Devices* **2017,** *14*, 1-10.
80. Jian, W.; Hui, D.; Lau, D., Nanoengineering in biomedicine: Current development and future perspectives. *Nanotechnology Reviews* **2020,** *9* (1), 700-715.
81. DeStefano, V.; Khan, S.; Tabada, A., Applications of PLA in modern medicine. *Engineered Regeneration* **2020,** *1*, 76-87.
82. Ostuni, E.; Chapman, R. G.; Holmlin, R. E.; Takayama, S.; Whitesides, G. M., A Survey of Structure−Property Relationships of Surfaces that Resist the Adsorption of Protein. *Langmuir* **2001,** *17* (18), 5605-5620.
83. Mano, J. F.; Silva, G. A.; Azevedo, H. S.; Malafaya, P. B.; Sousa, R. A.; Silva, S. S.; Boesel, L. F.; Oliveira, J. M.; Santos, T. C.; Marques, A. P.; Neves, N. M.; Reis, R. L., Natural origin biodegradable systems in tissue engineering and regenerative medicine: present status and some moving trends. *Journal of The Royal Society Interface* **2007,** *4* (17), 999-1030.
84. Reddy, M. S. B.; Ponnamma, D.; Choudhary, R.; Sadasivuni, K. K., A Comparative Review of Natural and Synthetic Biopolymer Composite Scaffolds. *Polymers* **2021,** *13* (7), 1105.
85. Suarato, G.; Bertorelli, R.; Athanassiou, A., Borrowing From Nature: Biopolymers and Biocomposites as Smart Wound Care Materials. *Frontiers in Bioengineering and Biotechnology* **2018,** *6*.
86. Chen, G. Q., A microbial polyhydroxyalkanoates (PHA) based bio- and materials industry. *Chem Soc Rev* **2009,** *38* (8), 2434-46.
87. Tchobanian, A.; Van Oosterwyck, H.; Fardim, P., Polysaccharides for tissue engineering: Current landscape and future prospects. *Carbohydr Polym* **2019,** *205*, 601-625.
88. Suh, J. K.; Matthew, H. W., Application of chitosan-based polysaccharide biomaterials in cartilage tissue engineering: a review. *Biomaterials* **2000,** *21* (24), 2589-98.
89. Reddy, N.; Yang, Y., Potential of plant proteins for medical applications. *Trends Biotechnol* **2011,** *29* (10), 490-8.
90. Zhang, Y.; Sun, T.; Jiang, C., Biomacromolecules as carriers in drug delivery and tissue engineering. *Acta Pharmaceutica Sinica B* **2018,** *8* (1), 34-50.
91. Gomes, A.; Sobral, P., Plant Protein-Based Delivery Systems: An Emerging Approach for Increasing the Efficacy of Lipophilic Bioactive Compounds. *Molecules* **2021,** *27* (1).
92. Wang, Y.; Kim, U.-J.; Blasioli, D. J.; Kim, H.-J.; Kaplan, D. L., In vitro cartilage tissue engineering with 3D porous aqueous-derived silk scaffolds and mesenchymal stem cells. *Biomaterials* **2005,** *26* (34), 7082-7094.
93. Suarato, G.; Contardi, M.; Perotto, G.; Heredia-Guerrero, J. A.; Fiorentini, F.; Ceseracciu, L.; Pignatelli, C.; Debellis, D.; Bertorelli, R.; Athanassiou, A., From fabric to tissue: Recovered wool keratin/polyvinylpyrrolidone biocomposite fibers as artificial scaffold platform. *Materials Science and Engineering: C* **2020,** *116*, 111151.
94. Kossyvaki, D.; Suarato, G.; Summa, M.; Gennari, A.; Francini, N.; Gounaki, I.; Venieri, D.; Tirelli, N.; Bertorelli, R.; Athanassiou, A.; Papadopoulou, E. L., Keratin–cinnamon essential oil biocomposite fibrous patches for skin burn care. *Materials Advances* **2020,** *1* (6), 1805-1816.

95. Yang, X.; Zhang, H.; Yuan, X.; Cui, S., Wool keratin: a novel building block for layer-by-layer self-assembly. *J Colloid Interface Sci* **2009,** *336* (2), 756-60.
96. Trojanowska, D. J.; Suarato, G.; Braccia, C.; Armirotti, A.; Fiorentini, F.; Athanassiou, A.; Perotto, G., Wool Keratin Nanoparticle-Based Micropatterns for Cellular Guidance Applications. *ACS Applied Nano Materials* **2022,** *5* (10), 15272-15287.
97. Hurtado-López, P.; Murdan, S., An investigation into the adjuvanticity and immunogenicity of zein microspheres being researched as drug and vaccine carriers. *Journal of Pharmacy and Pharmacology* **2010,** *58* (6), 769-774.
98. Reddy, N.; Yang, Y., Novel protein fibers from wheat gluten. *Biomacromolecules* **2007,** *8* (2), 638-43.
99. Dong, J.; Sun, Q.; Wang, J. Y., Basic study of corn protein, zein, as a biomaterial in tissue engineering, surface morphology and biocompatibility. *Biomaterials* **2004,** *25* (19), 4691-7.
100. Liu, X.; Sun, Q.; Wang, H.; Zhang, L.; Wang, J. Y., Microspheres of corn protein, zein, for an ivermectin drug delivery system. *Biomaterials* **2005,** *26* (1), 109-15.
101. Duclairoir, C.; Orecchioni, A. M.; Depraetere, P.; Osterstock, F.; Nakache, E., Evaluation of gliadins nanoparticles as drug delivery systems: a study of three different drugs. *Int J Pharm* **2003,** *253* (1-2), 133-44.
102. Fiorentini, F.; Suarato, G.; Grisoli, P.; Zych, A.; Bertorelli, R.; Athanassiou, A., Plant-based biocomposite films as potential antibacterial patches for skin wound healing. *European Polymer Journal* **2021,** *150*, 110414.
103. Silva, R.; Bulut, B.; Roether, J. A.; Kaschta, J.; Schubert, D. W.; Boccaccini, A. R., Sonochemical processing and characterization of composite materials based on soy protein and alginate containing micron-sized bioactive glass particles. *Journal of Molecular Structure* **2014,** *1073*, 87-96.
104. Paliwal, R.; Palakurthi, S., Zein in controlled drug delivery and tissue engineering. *J Control Release* **2014,** *189*, 108-22.
105. Argos, P.; Pedersen, K.; Marks, M. D.; Larkins, B. A., A structural model for maize zein proteins. *Journal of Biological Chemistry* **1982,** *257* (17), 9984-9990.
106. Tortorella, S.; Maturi, M.; Vetri Buratti, V.; Vozzolo, G.; Locatelli, E.; Sambri, L.; Comes Franchini, M., Zein as a versatile biopolymer: different shapes for different biomedical applications. *RSC Adv* **2021,** *11* (62), 39004-39026.
107. Dong, F.; Dong, X.; Zhou, L.; Xiao, H.; Ho, P. Y.; Wong, M. S.; Wang, Y., Doxorubicin-loaded biodegradable self-assembly zein nanoparticle and its anti-cancer effect: Preparation, in vitro evaluation, and cellular uptake. *Colloids Surf B Biointerfaces* **2016,** *140*, 324-331.
108. Barbosa, J.; Conway, B.; Merchant, H., Going Natural: Using polymers from nature for gastroresistant applications. *British Journal of Pharmacy* **2017,** *2*.
109. Iravani, S.; Varma, R. S., Plants and plant-based polymers as scaffolds for tissue engineering. *Green Chemistry* **2019,** *21* (18), 4839-4867.
110. Gong, S.; Wang, H.; Sun, Q.; Xue, S.-T.; Wang, J.-Y., Mechanical properties and in vitro biocompatibility of porous zein scaffolds. *Biomaterials* **2006,** *27* (20), 3793-3799.
111. Wang, H. J.; Gong, S. J.; Lin, Z. X.; Fu, J. X.; Xue, S. T.; Huang, J. C.; Wang, J. Y., In vivo biocompatibility and mechanical properties of porous zein scaffolds. *Biomaterials* **2007,** *28* (27), 3952-64.
112. Lai, H.-M.; Padua, G. W., Properties and Microstructure of Plasticized Zein Films. *Cereal Chemistry* **1997,** *74* (6), 771-775.
113. Shukla, R.; Cheryan, M., Zein: the industrial protein from corn. *Industrial Crops and Products* **2001,** *13* (3), 171-192.
114. Zhang, Y.; Cui, L.; Che, X.; Zhang, H.; Shi, N.; Li, C.; Chen, Y.; Kong, W., Zein-based films and their usage for controlled delivery: Origin, classes and current landscape. *J Control Release* **2015,** *206*, 206-19.
115. Liu, L.; Fishman, M. L.; Hicks, K. B.; Kende, M.; Ruthel, G., Pectin/zein beads for potential colon-specific drug delivery: synthesis and in vitro evaluation. *Drug Deliv* **2006,** *13* (6), 417-23.
116. Ur Rehman, M. A., Zein/Bioactive Glass Coatings with Controlled Degradation of Magnesium under Physiological Conditions: Designed for Orthopedic Implants. *Prosthesis* **2020,** *2* (3), 211-224.
117. Ahmed, Y.; Ur Rehman, M. A., Improvement in the surface properties of stainless steel via zein/hydroxyapatite composite coatings for biomedical applications. *Surfaces and Interfaces* **2020,** *20*, 100589.
118. Ariyoshi, Y., Angiotensin-converting enzyme inhibitors derived from food proteins. *Trends in Food Science & Technology* **1993,** *4* (5), 139-144.
119. Liang, Q.; Chalamaiah, M.; Liao, W.; Ren, X.; Ma, H.; Wu, J., Zein hydrolysate and its peptides exert anti-inflammatory activity on endothelial cells by preventing TNF-α-induced NF-κB activation. *Journal of Functional Foods* **2020,** *64*, 103598.
120. Shen, N.; Zhang, Y.; Wang, J., Parallel Plate Flow Chamber Device for Evaluation of Cell Retention of Electrospun Zein Fiber Film Under Steady Shear. *Journal of Shanghai Jiaotong University (Science)* **2021,** *26* (1), 69-75.

121. Xue, Y.-Q.; Zhang, Y.-C.; Zhang, Y.-B.; Wang, J.-Y., Zein-based 3D tubular constructs with tunable porosity for 3D cell culture and drug delivery. *Biomedical Engineering Advances* **2023,** *5*, 100059.
122. Whitesides, G. M., The origins and the future of microfluidics. *Nature* **2006,** *442* (7101), 368-373.
123. Tian, W.-C.; Finehout, E., *Microfluidics for Biological Applications*. 2008.
124. Cui, J.; Björnmalm, M.; Liang, K.; Xu, C.; Best, J. P.; Zhang, X.; Caruso, F., Super-Soft Hydrogel Particles with Tunable Elasticity in a Microfluidic Blood Capillary Model. *Advanced Materials* **2014,** *26* (43), 7295-7299.
125. Mei, X.; Middleton, K.; Shim, D.; Wan, Q.; Xu, L.; Ma, Y. V.; Devadas, D.; Walji, N.; Wang, L.; Young, E. W. K.; You, L., Microfluidic platform for studying osteocyte mechanoregulation of breast cancer bone metastasis. *Integr Biol (Camb)* **2019,** *11* (4), 119-129.
126. Park, J. Y.; Yoo, S. J.; Hwang, C. M.; Lee, S.-H., Simultaneous generation of chemical concentration and mechanical shear stress gradients using microfluidic osmotic flow comparable to interstitial flow. *Lab on a Chip* **2009,** *9* (15), 2194-2202.
127. Sakolish, Courtney M.; Mahler, G. J., A novel microfluidic device to model the human proximal tubule and glomerulus. *RSC Advances* **2017,** *7* (8), 4216-4225.
128. Simitian, G.; Virumbrales-Muñoz, M.; Sánchez-de-Diego, C.; Beebe, D. J.; Kosoff, D., Microfluidics in vascular biology research: a critical review for engineers, biologists, and clinicians. *Lab on a Chip* **2022,** *22* (19), 3618-3636.
129. Burke, K. S.; Parul, D.; Reddish, M. J.; Dyer, R. B., A simple three-dimensional-focusing, continuous-flow mixer for the study of fast protein dynamics. *Lab on a Chip* **2013,** *13* (15), 2912-2921.
130. Sun, H.; Olsen, T.; Zhu, J.; Tao, J.; Ponnaiya, B.; Amundson, S. A.; Brenner, D. J.; Lin, Q., A bead-based microfluidic approach to integrated single-cell gene expression analysis by quantitative RT-PCR. *RSC Advances* **2015,** *5* (7), 4886-4893.
131. Kai, J.; Puntambekar, A.; Santiago, N.; Lee, S. H.; Sehy, D. W.; Moore, V.; Han, J.; Ahn, C. H., A novel microfluidic microplate as the next generation assay platform for enzyme linked immunoassays (ELISA). *Lab on a Chip* **2012,** *12* (21), 4257-4262.
132. Picollet-D'hahan, N.; Dolega, M. E.; Liguori, L.; Marquette, C.; Le Gac, S.; Gidrol, X.; Martin, D. K., A 3D Toolbox to Enhance Physiological Relevance of Human Tissue Models. *Trends Biotechnol* **2016,** *34* (9), 757-769.
133. Berlanda, S. F.; Breitfeld, M.; Dietsche, C. L.; Dittrich, P. S., Recent Advances in Microfluidic Technology for Bioanalysis and Diagnostics. *Analytical Chemistry* **2021,** *93* (1), 311-331.
134. Chaitanya Vishnubhatla, K.; Clark, J.; Lanzani, G.; Ramponi, R.; Osellame, R.; Virgili, T., Femtosecond laser fabrication of microfluidic channels for organic photonic devices. *Appl. Opt.* **2009,** *48* (31), G114-G118.
135. Bonfadini, S.; Ciciulla, F.; Criante, L.; Zaltron, A.; Simoni, F.; Reshetnyak, V.; Lucchetti, L., Optofluidic platform using liquid crystals in lithium niobate microchannel. *Scientific Reports* **2019,** *9* (1), 1062.
136. Storti, F.; Bonfadini, S.; Criante, L., Battery-free fully integrated microfluidic light source for portable lab-on-a-chip applications. *Scientific Reports* **2020,** *10* (1), 12910.
137. Wu, J.; Zheng, G.; Lee, L. M., Optical imaging techniques in microfluidics and their applications. *Lab on a Chip* **2012,** *12* (19), 3566-3575.
138. Huh, D.; Hamilton, G. A.; Ingber, D. E., From 3D cell culture to organs-on-chips. *Trends Cell Biol* **2011,** *21* (12), 745-54.
139. Chin, V. I.; Taupin, P.; Sanga, S.; Scheel, J.; Gage, F. H.; Bhatia, S. N., Microfabricated platform for studying stem cell fates. *Biotechnology and Bioengineering* **2004,** *88* (3), 399-415.
140. Fenton, O. S.; Olafson, K. N.; Pillai, P. S.; Mitchell, M. J.; Langer, R., Advances in Biomaterials for Drug Delivery. *Advanced Materials* **2018,** *30* (29), 1705328.
141. Kent, N. J.; Basabe-Desmonts, L.; Meade, G.; MacCraith, B. D.; Corcoran, B. G.; Kenny, D.; Ricco, A. J., Microfluidic device to study arterial shear-mediated platelet-surface interactions in whole blood: reduced sample volumes and well-characterised protein surfaces. *Biomedical Microdevices* **2010,** *12* (6), 987-1000.
142. Usami, S.; Chen, H. H.; Zhao, Y.; Chien, S.; Skalak, R., Design and construction of a linear shear stress flow chamber. *Ann Biomed Eng* **1993,** *21* (1), 77-83.
143. Li, Z.; Seker, E., Configurable microfluidic platform for investigating therapeutic delivery from biomedical device coatings. *Lab on a Chip* **2017,** *17* (19), 3331-3337.
144. Jia, Z.; Ma, C.; Zhang, H., PLGA Coatings and PLGA Drug-Loading Coatings for Cardiac Stent Samples: Degradation Characteristics and Blood Compatibility. *Coatings* **2021,** *11* (11), 1427.
145. Zheng, Q.; Chu, Z.; Li, X.; Kang, H.; Yang, X.; Fan, Y., The Effect of Fluid Shear Stress on the In Vitro Release Kinetics of Sirolimus from PLGA Films. *Polymers* **2017,** *9* (11), 618-630.
146. Wang, J.; Liu, L.; Wu, Y.; Maitz, M. F.; Wang, Z.; Koo, Y.; Zhao, A.; Sankar, J.; Kong, D.; Huang, N.; Yun, Y., Ex vivo blood vessel bioreactor for analysis of the biodegradation of magnesium stent models with and without vessel wall integration. *Acta Biomater* **2017,** *50*, 546-555.

147. Scarcello, E.; Lison, D., Are Fe-Based Stenting Materials Biocompatible? A Critical Review of In Vitro and In Vivo Studies. *J Funct Biomater* **2019,** *11* (1).
148. Ye, C.; Wang, J.; Zhao, A.; He, D.; Maitz, M. F.; Zhou, N.; Huang, N., Atorvastatin Eluting Coating for Magnesium-Based Stents: Control of Degradation and Endothelialization in a Microfluidic Assay and In Vivo. *Advanced Materials Technologies* **2020,** *5* (4), 1900947.
149. Cheng, Y.; Zhang, X.; Liu, R.; Li, Y.; Zeng, J.; Zhou, M.; Zhao, Y., Bioinspired Vascular Stents with Microfluidic Electrospun Multilayer Coatings for Preventing In-Stent Restenosis. *Advanced Healthcare Materials* **2022,** *11* (17), 2200965.
150. Westein, E.; de Witt, S.; Lamers, M.; Cosemans, J. M.; Heemskerk, J. W., Monitoring in vitro thrombus formation with novel microfluidic devices. *Platelets* **2012,** *23* (7), 501-509.
151. Provenzale, I.; Brouns, S. L. N.; van der Meijden, P. E. J.; Swieringa, F.; Heemskerk, J. W. M., Whole Blood Based Multiparameter Assessment of Thrombus Formation in Standard Microfluidic Devices to Proxy In Vivo Haemostasis and Thrombosis. *Micromachines (Basel)* **2019,** *10* (11), 787.
152. Roopmani, P.; Sethuraman, S.; Satheesh, S.; Maheswari Krishnan, U., The metamorphosis of vascular stents: passive structures to smart devices. *RSC Advances* **2016,** *6* (4), 2835-2853.
153. Palmerini, T.; Biondi-Zoccai, G.; Della Riva, D.; Mariani, A.; Genereux, P.; Branzi, A.; Stone, G. W., Stent thrombosis with drug-eluting stents: is the paradigm shifting? *Journal of the American College of Cardiology* **2013,** *62* (21), 1915-1921.
154. Strohbach, A.; Busch, R., Polymers for Cardiovascular Stent Coatings. *International Journal of Polymer Science* **2015,** *2015*, 1-11.
155. Balaji, A.; Jaganathan, S. K.; Vellayappan, M. V.; John, A. A.; Subramanian, A. P.; SelvaKumar, M.; Mohandas, H.; M, S. R.; Supriyanto, E., Prospects of common biomolecules as coating substances for polymeric biomaterials. *RSC Advances* **2015,** *5* (85), 69660-69679.
156. Corradini, E.; Curti, P. S.; Meniqueti, A. B.; Martins, A. F.; Rubira, A. F.; Muniz, E. C., Recent advances in food-packing, pharmaceutical and biomedical applications of zein and zein-based materials. *Int J Mol Sci* **2014,** *15* (12), 22438-70.
157. Ciumărnean, L.; Milaciu, M. V.; Runcan, O.; Vesa Ș, C.; Răchișan, A. L.; Negrean, V.; Perné, M. G.; Donca, V. I.; Alexescu, T. G.; Para, I.; Dogaru, G., The Effects of Flavonoids in Cardiovascular Diseases. *Molecules* **2020,** *25* (18).
158. Diwan, V.; Brown, L.; Gobe, G. C., The flavonoid rutin improves kidney and heart structure and function in an adenine-induced rat model of chronic kidney disease. *Journal of Functional Foods* **2017,** *33*, 85-93.
159. Lescano, C. H.; Freitas de Lima, F.; Cardoso, C. A. L.; Vieira, S. C. H.; Mónica, F. Z.; Pires de Oliveira, I., Rutin present in Alibertia edulis extract acts on human platelet aggregation through inhibition of cyclooxygenase/thromboxane. *Food & Function* **2021,** *12* (2), 802-814.
160. Siti, H. N.; Jalil, J.; Asmadi, A. Y.; Kamisah, Y., Parkia speciosa Hassk. Empty Pod Extract Alleviates Angiotensin II-Induced Cardiomyocyte Hypertrophy in H9c2 Cells by Modulating the Ang II/ROS/NO Axis and MAPK Pathway. *Front Pharmacol* **2021,** *12*, 741623.
161. Ugusman, A.; Zakaria, Z.; Chua, K. H.; Megat Mohd Nordin, N. A.; Abdullah Mahdy, Z., Role of Rutin on Nitric Oxide Synthesis in Human Umbilical Vein Endothelial Cells. *The Scientific World Journal* **2014,** *2014*, 169370.
162. Puskas, J. E.; Muñoz-Robledo, L. G.; Hoerr, R. A.; Foley, J.; Schmidt, S. P.; Evancho-Chapman, M.; Dong, J.; Frethem, C.; Haugstad, G., Drug-eluting stent coatings. *WIREs Nanomedicine and Nanobiotechnology* **2009,** *1* (4), 451-462.
163. Yoshioka, T.; Tsuru, K.; Hayakawa, S.; Osaka, A., Preparation of alginic acid layers on stainless-steel substrates for biomedical applications. *Biomaterials* **2003,** *24* (17), 2889-2894.
164. Lewis, F.; Maheux-Lacroix, B.; Turgeon, S.; Mantovani, D., Evaluation of the Adhesion of Ultra-Thin Teflon-Like Films Deposited by Plasma on 316L Stainless Steel for Long-Term Stable Drug-Eluting Stents. *Advanced Materials Research* **2007,** *15-17*, 119-124.
165. Brahatheeswaran, D.; Mathew, A.; Aswathy, R. G.; Nagaoka, Y.; Venugopal, K.; Yoshida, Y.; Maekawa, T.; Sakthikumar, D., Hybrid fluorescent curcumin loaded zein electrospun nanofibrous scaffold for biomedical applications. *Biomed Mater* **2012,** *7* (4), 045001.
166. Bedair, T. M.; Cho, Y.; Kim, T. J.; Kim, Y. D.; Park, B. J.; Joung, Y. K.; Han, D. K., Reinforcement of Interfacial Adhesion of a Coated Polymer Layer on a Cobalt–Chromium Surface for Drug-Eluting Stents. *Langmuir* **2014,** *30* (27), 8020-8028.
167. Jang, T. S.; Cheon, K. H.; Ahn, J. H.; Song, E. H.; Kim, H. E.; Jung, H. D., In-vitro blood and vascular compatibility of sirolimus-eluting organic/inorganic hybrid stent coatings. *Colloids Surf B Biointerfaces* **2019,** *179*, 405-413.
168. Thawien, W., Protein-Based Edible Films: Characteristics and Improvement of Properties. In *Structure and Function of Food Engineering*, Ayman Amer, E., Ed. IntechOpen: Rijeka, 2012; p Ch. 3.

169. Bidyarani, N.; Kumar, U., Synthesis of rotenone loaded zein nano-formulation for plant protection against pathogenic microbes. *RSC Advances* **2019,** *9* (70), 40819-40826.
170. Alcântara, A. C. S.; Aranda, P.; Darder, M.; Ruiz-Hitzky, E., Bionanocomposites based on alginate–zein/layered double hydroxide materials as drug delivery systems. *Journal of Materials Chemistry* **2010,** *20* (42), 9495-9504.
171. Jem, K. J.; Tan, B., The development and challenges of poly (lactic acid) and poly (glycolic acid). *Advanced Industrial and Engineering Polymer Research* **2020,** *3* (2), 60-70.
172. Pan Ch, J.; Tang, J. J.; Weng, Y. J.; Wang, J.; Huang, N., Preparation, characterization and anticoagulation of curcumin-eluting controlled biodegradable coating stents. *J Control Release* **2006,** *116* (1), 42-9.
173. Kim, J. H.; Ko, N. R.; Jung, B.-Y.; Kwon, I. K., Development of a novel dual PLGA and alginate coated drug-eluting stent for enhanced blood compatibility. *Macromolecular Research* **2016,** *24* (10), 931-939.
174. Basnett, P.; Ching, K. Y.; Stolz, M.; Knowles, J. C.; Boccaccini, A. R.; Smith, C.; Locke, I. C.; Roy, I., Aspirin-loaded P(3HO)/P(3HB) blend films: potential materials for biodegradable drug-eluting stents. *Bioinspired, Biomimetic and Nanobiomaterials* **2013,** *2* (3), 141-153.
175. Xu, W.; Yagoshi, K.; Asakura, T.; Sasaki, M.; Niidome, T., Silk Fibroin as a Coating Polymer for Sirolimus-Eluting Magnesium Alloy Stents. *ACS Applied Bio Materials* **2019,** *3* (1), 531-538.
176. Li, J.; He, J.; Huang, Y.; Li, D.; Chen, X., Improving surface and mechanical properties of alginate films by using ethanol as a co-solvent during external gelation. *Carbohydr Polym* **2015,** *123*, 208-16.
177. Costa, M. J.; Marques, A. M.; Pastrana, L. M.; Teixeira, J. A.; Sillankorva, S. M.; Cerqueira, M. A., Physicochemical properties of alginate-based films: Effect of ionic crosslinking and mannuronic and guluronic acid ratio. *Food Hydrocolloids* **2018,** *81*, 442-448.
178. Morales-Gonzalez, M.; Arévalo-Alquichire, S.; Diaz, L. E.; Sans, J. Á.; Vilariño-Feltrer, G.; Gómez-Tejedor, J. A.; Valero, M. F., Hydrolytic stability and biocompatibility on smooth muscle cells of polyethylene glycol–polycaprolactone-based polyurethanes. *Journal of Materials Research* **2020,** *35* (23), 3276-3285.
179. Huang, Y.; Venkatraman, S. S.; Boey, F. Y.; Lahti, E. M.; Umashankar, P. R.; Mohanty, M.; Arumugam, S.; Khanolkar, L.; Vaishnav, S., In vitro and in vivo performance of a dual drug-eluting stent (DDES). *Biomaterials* **2010,** *31* (15), 4382-91.
180. Thakkar, A.; Raval, A.; Mandal, R.; Parmar, S.; Jariwala, A.; Tailor, J.; Mehta, A., Development and Evaluation of Drug Eluting Stent Having Biphasic Release From a Single Layer of Biodegradable Polymer. *Journal of Medical Devices* **2013,** *7* (1).
181. Chen, M. C.; Liang, H. F.; Chiu, Y. L.; Chang, Y.; Wei, H. J.; Sung, H. W., A novel drug-eluting stent spray-coated with multi-layers of collagen and sirolimus. *J Control Release* **2005,** *108* (1), 178-89.
182. Okoh, S. O.; Asekun, O. T.; Familoni, O. B.; Afolayan, A. J., Antioxidant and Free Radical Scavenging Capacity of Seed and Shell Essential Oils Extracted from Abrus precatorius (L). *Antioxidants (Basel)* **2014,** *3* (2), 278-87.
183. Gbureck, U.; Vorndran, E.; Barralet, J. E., Modeling vancomycin release kinetics from microporous calcium phosphate ceramics comparing static and dynamic immersion conditions. *Acta Biomaterialia* **2008,** *4* (5), 1480-1486.
184. McKittrick, C. M.; Kennedy, S.; Oldroyd, K. G.; McGinty, S.; McCormick, C., Modelling the Impact of Atherosclerosis on Drug Release and Distribution from Coronary Stents. *Annals of biomedical engineering* **2016,** *44* (2), 477-487.
185. Kamberi, M.; Nayak, S.; Myo-Min, K.; Carter, T. P.; Hancock, L.; Feder, D., A novel accelerated in vitro release method for biodegradable coating of drug eluting stents: Insight to the drug release mechanisms. *European Journal of Pharmaceutical Sciences* **2009,** *37* (3-4), 217-222.
186. Yusuf, S.; Zhao, F.; Mehta, S. R.; Chrolavicius, S.; Tognoni, G.; Fox, K. K., Effects of clopidogrel in addition to aspirin in patients with acute coronary syndromes without ST-segment elevation. *N Engl J Med* **2001,** *345* (7), 494-502.
187. Hietala, E.-M.; Maasilta, P.; Juuti, H.; Nuutinen, J.-P.; Harjula, A. L. J.; Salminen, U.-S.; Lassila, R., Platelet deposition on stainless steel, spiral, and braided polylactide stents. *Thromb Haemost* **2004,** *92* (12), 1394-1401.
188. Kenry; Loh, K. P.; Lim, C. T., Molecular Hemocompatibility of Graphene Oxide and Its Implication for Antithrombotic Applications. *Small* **2015,** *11* (38), 5105-5117.
189. Groth, T.; Podias, A.; Missirlis, Y., Platelet adhesion and activation under static and flow conditions. *Colloids and Surfaces B: Biointerfaces* **1994,** *3* (4), 241-249.
190. Amoyav, B.; Goldstein, Y.; Steinberg, E.; Benny, O., 3D Printed Microfluidic Devices for Drug Release Assays. *Pharmaceutics* **2020,** *13* (1), 13.
191. Unal, G.; Bucher, S.; Carlier, S.; Slabaugh, G.; Fang, T.; Tanaka, K., Shape-Driven Segmentation of the Arterial Wall in Intravascular Ultrasound Images. *IEEE Transactions on Information Technology in Biomedicine* **2008,** *12* (3), 335-347.

192. Bentzon, J. F.; Otsuka, F.; Virmani, R.; Falk, E., Mechanisms of plaque formation and rupture. *Circ Res* **2014,** *114* (12), 1852-66.
193. Brindise, M. C.; Busse, M. M.; Vlachos, P. P., Density and Viscosity Matched Newtonian and non-Newtonian Blood-Analog Solutions with PDMS Refractive Index. *Exp Fluids* **2018,** *59* (11), 173.
194. Tas, A. C., The use of physiological solutions or media in calcium phosphate synthesis and processing. *Acta Biomaterialia* **2014,** *10* (5), 1771-92.
195. Bruschi, M. L., Mathematical models of drug release. In *Strategies to Modify the Drug Release from Pharmaceutical Systems*, Woodhead Publishing: 2015; pp 63-86.
196. Calzavara, D.; Ferraro, D.; Litti, L.; Cappozzo, G.; Mistura, G.; Meneghetti, M.; Pierno, M., Single File Flow of Biomimetic Beads for Continuous SERS Recording in a Microfluidic Device. *Advances in Condensed Matter Physics* **2018,** *2018*, 2849175.
197. Reimers, R.; Sutera, S.; Joist, J., Potentiation by red blood cells of shear-induced platelet aggregation: relative importance of chemical and physical mechanisms. *Blood* **1984,** *64* (6), 1200-1206.
198. Zhang, Z.; Borenstein, J.; Guiney, L.; Miller, R.; Sukavaneshvar, S.; Loose, C., Polybetaine modification of PDMS microfluidic devices to resist thrombus formation in whole blood. *Lab on a Chip* **2013,** *13* (10), 1963-1968.
199. Tomohiko, Y.; Kanji, T.; Satoshi, H.; Akiyoshi, O., Preparation of alginic acid layers on stainless-steel substrates for biomedical applications. *Biomaterials* **2003,** *24* (17), 2889-2894.
200. Wang, X.; Shi, N.; Chen, Y.; Li, C.; Du, X.; Jin, W.; Chen, Y.; Chang, P. R., Improvement in hemocompatibility of chitosan/soy protein composite membranes by heparinization. *BioMedical Materials and Engineering* **2012,** *22* (1-3), 143-50.
201. 10993-4 . Biological evaluation of medical devices -Part 4: Selection of tests for interactions with blood. 2022.
202. Wei, Z.; Tian, P.; Liu, X.; Zhou, B., In vitro degradation, hemolysis, and cytocompatibility of PEO/PLLA composite coating on biodegradable AZ31 alloy. *J Biomed Mater Res B Appl Biomater* **2015,** *103* (2), 342-54.
203. Li, H.; Peng, F.; Wang, D.; Qiao, Y.; Xu, D.; Liu, X., Layered double hydroxide/poly-dopamine composite coating with surface heparinization on Mg alloys: improved anticorrosion, endothelialization and hemocompatibility. *Biomaterials Science* **2018,** *6* (7), 1846-1858.
204. Tamura, T., Blood Flow Measurement. In *Comprehensive Biomedical Physics*, Brahme, A., Ed. Elsevier: Oxford, 2014; pp 91-105.
205. Fu, J.; Su, Y.; Qin, Y.-X.; Zheng, Y.; Wang, Y.; Zhu, D., Evolution of metallic cardiovascular stent materials: A comparative study among stainless steel, magnesium and zinc. *Biomaterials* **2020,** *230*, 119641.
206. Swaine, T.; Tang, Y.; Garcia, P.; John, J.; Waters, L. J.; Lewis, A. L., Evaluation of ion exchange processes in drug-eluting embolization beads by use of an improved flow-through elution method. *European Journal of Pharmaceutical Sciences* **2016,** *93*, 351-359.
207. Nødland, O.; Lohne, A.; Stavland, A.; Hiorth, A., An Investigation of Polymer Mechanical Degradation in Radial Well Geometry. *Transport in Porous Media* **2019,** *128* (1), 1-27.
208. Hermans, K.; Van den Plas, D.; Kerimova, S.; Carleer, R.; Adriaensens, P.; Weyenberg, W.; Ludwig, A., Development and characterization of mucoadhesive chitosan films for ophthalmic delivery of cyclosporine A. *International Journal of Pharmaceutics* **2014,** *472* (1-2), 10-9.
209. Cooperman, L.; Michaeli, D., The immunogenicity of injectable collagen. I. A 1-year prospective study. *J Am Acad Dermatol* **1984,** *10* (4), 638-46.
210. Berardi, A.; Bisharat, L.; Bonacucina, G.; Casettari, L.; Logrippo, S.; Cespi, M.; AlKhatib, H. S.; Palmieri, G. F., Formulation, swelling and dissolution kinetics study of zein based matrix tablets. *Powder Technology* **2017,** *310*, 241-249.
211. Goodman, S. L.; Grasel, T. G.; Cooper, S. L.; Albrecht, R. M., Platelet shape change and cytoskeletal reorganization on polyurethaneureas. *Journal of biomedical materials research* **1989,** *23* (1), 105-23.
212. Palmaz, J. C.; Bailey, S.; Marton, D.; Sprague, E., Influence of stent design and material composition on procedure outcome. *J Vasc Surg* **2002,** *36* (5), 1031-9.
213. Choi, S.-S.; Park, H.-R.; Lee, K.-A., A Comparative Study of Rutin and Rutin Glycoside: Antioxidant Activity, Anti-Inflammatory Effect, Effect on Platelet Aggregation and Blood Coagulation. *Antioxidants* **2021,** *10* (11), 1696.
214. Butruk-Raszeja, B.; Trzaskowski, M.; Ciach, T., Cell membrane-mimicking coating for blood-contacting polyurethanes. *J Biomater Appl* **2015,** *29* (6), 801-12.
215. Ji, X.; Yang, W.; Wang, T.; Mao, C.; Guo, L.; Xiao, J.; He, N., Coaxially Electrospun Core/Shell Structured Poly(L-Lactide) Acid/Chitosan Nanofibers for Potential Drug Carrier in Tissue Engineering. *Journal of Biomedical Nanotechnology* **2013,** *9* (10), 1672-1678.
216. Chou, T. C.; Fu, E.; Wu, C. J.; Yeh, J. H., Chitosan enhances platelet adhesion and aggregation. *Biochemical and Biophysical Research Communications* **2003,** *302* (3), 480-3.

217. Lovett, M.; Eng, G.; Kluge, J. A.; Cannizzaro, C.; Vunjak-Novakovic, G.; Kaplan, D. L., Tubular silk scaffolds for small diameter vascular grafts. *Organogenesis* **2010,** *6* (4), 217-24.
218. Michalska-Sionkowska, M.; Warżyńska, O.; Kaczmarek-Szczepańska, B.; Łukowicz, K.; Osyczka, A. M.; Walczak, M., Preparation and Characterization of Fish Skin Collagen Material Modified with β-Glucan as Potential Wound Dressing. *Materials* **2021,** *14* (6), 1322.
219. Wu, Z.; Zhou, W.; Deng, W.; Xu, C.; Cai, Y.; Wang, X., Antibacterial and Hemostatic Thiol-Modified Chitosan-Immobilized AgNPs Composite Sponges. *ACS Applied Materials & Interfaces* **2020,** *12* (18), 20307-20320.
220. Li, J.; Chen, Q.; Zhang, Q.; Fan, T.; Gong, L.; Ye, W.; Fan, Z.; Cao, L., Improving Mechanical Properties and Biocompatibilities by Highly Oriented Long Chain Branching Poly(lactic acid) with Bionic Surface Structures. *ACS Applied Materials & Interfaces* **2020,** *12* (12), 14365-14375.
221. Friedrich, K., Chapter 1 - Routes for achieving multifunctionality in reinforced polymers and composite structures. In *Multifunctionality of Polymer Composites*, Friedrich, K.; Breuer, U., Eds. William Andrew Publishing: Oxford, 2015; pp 3-41.
222. Van Kruchten, R.; Cosemans, J. M.; Heemskerk, J. W., Measurement of whole blood thrombus formation using parallel-plate flow chambers - a practical guide. *Platelets* **2012,** *23* (3), 229-42.
223. Jain, A.; Graveline, A.; Waterhouse, A.; Vernet, A.; Flaumenhaft, R.; Ingber, D. E., A shear gradient-activated microfluidic device for automated monitoring of whole blood haemostasis and platelet function. *Nature Communications* **2016,** *7* (1), 10176.
224. Ting, L. H.; Feghhi, S.; Taparia, N.; Smith, A. O.; Karchin, A.; Lim, E.; John, A. S.; Wang, X.; Rue, T.; White, N. J.; Sniadecki, N. J., Contractile forces in platelet aggregates under microfluidic shear gradients reflect platelet inhibition and bleeding risk. *Nature communications* **2019,** *10* (1), 1204-1204.
225. Minelli, C.; Kikuta, A.; Tsud, N.; Ball, M. D.; Yamamoto, A., A micro-fluidic study of whole blood behaviour on PMMA topographical nanostructures. *Journal of Nanobiotechnology* **2008,** *6* (1), 3.
226. Ollivier, V.; Roques, C.; Receveur, N.; Gratz, M.; Feldman, L.; Letourneur, D.; Gachet, C.; Mangin, P. H.; Jandrot-Perrus, M., Bioreactivity of stent material: Activation of platelets, coagulation, leukocytes and endothelial cell dysfunction in vitro. *Platelets* **2017,** *28* (6), 529-539.
227. Sarvepalli, D. P.; Schmidtke, D. W.; Nollert, M. U., Design considerations for a microfluidic device to quantify the platelet adhesion to collagen at physiological shear rates. *Annals of Biomedical Engineering* **2009,** *37* (7), 1331-41.
228. de Witt, S. M.; Swieringa, F.; Cavill, R.; Lamers, M. M. E.; van Kruchten, R.; Mastenbroek, T.; Baaten, C.; Coort, S.; Pugh, N.; Schulz, A.; Scharrer, I.; Jurk, K.; Zieger, B.; Clemetson, K. J.; Farndale, R. W.; Heemskerk, J. W. M.; Cosemans, J. M. E. M., Identification of platelet function defects by multi-parameter assessment of thrombus formation. *Nature Communications* **2014,** *5* (1), 4257.
229. Claesson, K.; Lindahl, T. L.; Faxälv, L., Counting the platelets: a robust and sensitive quantification method for thrombus formation. *Thrombosis and Haemostasis* **2016,** *115* (6), 1178-1190.
230. Merciadez, M.; Alquier, L.; Mehta, R.; Patel, A.; Wang, A., A novel method for the elution of sirolimus (rapamycin) in drug-eluting stents. *Dissolution Technologies* **2011,** *18* (4), 37-42.